

DEVICE PHYSICS AND MATERIAL SCIENCE OF ORGANIC ELECTROCHEMICAL
TRANSISTORS

by

JACOB T. FRIEDLEIN

B.A., Washington University in St. Louis, 2012

A thesis submitted to the

Faculty of the Graduate School of the

University of Colorado in partial fulfillment

of the requirement for the degree of

Doctor of Philosophy

Department of Electrical, Computer, and Energy Engineering

2017

This thesis entitled:
Device physics and material science of organic electrochemical transistors
written by Jacob T. Friedlein
has been approved for the Department of Electrical, Computer, and Energy Engineering

Professor George G. Malliaras

Professor Robert R. McLeod

Date_____

The final copy of this thesis has been examined by the signatories, and we find that both the content and the form meet acceptable presentation standards of scholarly work in the above mentioned discipline.

Abstract

Friedlein, Jacob T. (Ph.D., Electrical, Computer, and Energy Engineering)

Device physics and material science of organic electrochemical transistors

Thesis directed by Professor Robert R. McLeod

Organic electrochemical transistors (OECTs) are hybrid ionic/electronic devices capable of high-gain signal amplification and have shown exceptional performance in numerous applications such as logic circuits, neuromorphic elements, and biosensing platforms. The work in this thesis improves understanding of OECT behavior and demonstrates how to improve OECT performance in several applications. Prior to our work, researchers understood OECTs in terms of standard models for metal-oxide-semiconductor field-effect transistors (MOSFETs). While these models yielded insight about OECT behavior, they fell short of providing accurate quantitative predictions for two reasons. First, organic semiconductors in OECTs are disordered materials and conduct electricity in fundamentally different ways than crystalline semiconductors in MOSFETs. Secondly, ionic charge storage in OECTs endows them with channel capacitances several orders of magnitude greater than that of typical MOSFETs.

We address these differences between OECTs and MOSFETs, and we derive predictive models for OECT behavior. First, we report combined optical and electrical measurements of OECTs, yielding evidence that, unlike the conductivity of crystalline semiconductors, the conductivity of polymer semiconductors in OECTs has a non-linear dependence on charge carrier concentration. We derive a model that explains this behavior and enables up to 125% improvement of signal amplification with OECTs. Next, we address a ubiquitous, yet unexplained characteristic of OECTs – the non-monotonic relationship between signal amplification and applied voltage. We show this is due to material disorder in OECTs, and we explain this behavior with a model that fits experimental data for two different types of OECTs. Finally, we provide a model for the transient response of OECTs. Our model predicts that

although OECTs are typically slow because of large channel capacitances, they can respond much faster than the RC time constant. We demonstrate that at a particular voltage, OECTs respond >30 times faster than the RC time constant, reaching steady state in $< 20 \mu\text{s}$.

Altogether, our work enables OECTs to operate at higher speeds and with higher gains, and it allows more accurate interpretation of OECT-based sensor measurements.

Dedication

To Addison, Aidan, and Boaz. *Cherchez les montagnes.*

Acknowledgments

I owe gratitude to many people who have guided and helped me in various ways during my PhD. First, I must thank my advisor, Professor Robert McLeod for teaching me something about charisma and enthusiasm and helping me improve my technical communication skills. Additionally, Professor McLeod always provided me with the resources I needed to perform my research. The resources he provided me were myriad and included writing letters of recommendation for fellowships, grant money for the test equipment I used for the data reported in this thesis, introductions to collaborators, encouragement and funding to attend the highest-quality conferences – where I became immersed in my field, and of course, his ceaseless availability to discuss the millions of little problems and breakthroughs that occurred in my research over the past five years.

The next person I'd like to thank is Professor Sean Shaheen who has been helping me as a collaborator since the first days of my thesis. The first way he helped me was to introduce me to his former student Robert Nawrocki who patiently taught me the basics of working with organic electronics. Over the past five years, I've enjoyed working with Professor Shaheen and his students Daniel Weingarten, Josh Brown, Alex Dixon, Sean Dunfield, and others, who generously shared their lab space, equipment, and expertise with me.

I must also extend an enthusiastic thank you to Professors George Malliaras and Róisín Owens who hosted me for a total of twelve months over the course of three years in their lab in the Centre Microelectronique de Provence (CMP). I was warmly welcomed by Professor Malliaras, Professor Owens, and their students, and I felt truly at home in the beautiful city of Gardanne, France. Furthermore, Professor Malliaras greatly helped me with my PhD research. He shared his laboratory, equipment, and resources with me. He provided project ideas for my

thesis and gave me critical advice and guidance with my work. It is no coincidence that each of my first author papers were accepted at the end of a visit to his lab.

Many of Professor Malliaras's students deserve a special thanks as well. Although I can't possibly mention everyone from CMP who encouraged and taught me during my PhD, I will mention three individuals from CMP who gave me the most technical assistance. These people are Professor Jonathan Rivnay, Dr. Mary Donahue, and Dr. Marcel Brändlein. I hope you all understand how much you've helped me with my PhD. While most of what these three contributed to my work is intangible, I can at least acknowledge that they fabricated the majority of the transistors that I tested and published during my thesis.

Other people who helped me during my PhD career include the technicians in the fabrication labs I worked in at the University of Colorado and CMP. Many thanks to Gaëlle Rondeau, Thierry Camillioni, Adel Hama, Dr. Zefram Marks, Dr. Tzu-Min Ou, Ryan Brow, Alex Denton, Andrea Randolph, Jan Van Zeghbroeck, Professor Van Zeghbroeck, and Dr. David Alchenberger.

I'd also like to thank the students of Iain McCullough's lab, chiefly Alexander Giovannitti and Dan-Tiberiu Sbircea, who provided the semiconductor p(g2T-TT) that I used in some of my work.

Next, I should mention funding agencies who made my work possible. My graduate research stipend was provided by the Department of Education Graduate Assistantships in Areas of National Need Award No. P200A120063 and the NSF GRFP Award No. DGE 1144083. The research material and equipment that I used was mostly provided by National Science Foundation Grant No. DMR-1006930 (awarded to Professor Shaheen), National Science Foundation Grant CAREER (No. ECCS 0847390 – awarded to Professor McLeod), and National

Science Foundation Grant No. ECCS 1509909 (awarded jointly to Professor McLeod and Shaheen).

Finally I want to thank the students in Professor McLeod's lab for their technical help and friendship over the past five years. Thanks to Marvin Alim, Dr. Martha Bodine, Katrina Bossenbroek, Dr. Callie Fiedler, Dr. Darren Forman, David Glugla, Johnny Hergert, Dr. Ben Kowalski, Dr. Zefram Marks, David Miller, Archish Muralidharan, Josh Noble, Charlie Rackson, Megan Renny, Amy Resman, Dr. Amy Sullivan, Camilla Uzcategui.

Table of Contents

Chapter I Introduction.....	1
A. Background.....	1
B. OECT operating principles	2
C. Models for OECT behavior.....	6
D. Applications for OECTs	10
E. Summary	15
Chapter II Simultaneous optical and electrical measurements revealing non-uniform hole mobility in OECTs	18
A. Background.....	18
1. Electrochromism in semiconducting polymers.....	18
2. Applications for electrochromism.....	20
B. Moving front experiments for estimating ionic mobility	24
C. Optical measurements revealing non-uniform hole mobility in OECTs.....	30
D. Development of a non-uniform mobility model	30
1. Optical evidence for non-uniform hole mobility	34
2. Geometrical scaling of transistor parameters.....	39
3. Transconductance optimization	43
E. Conclusion.....	45
Chapter III Influence of disorder on transfer characteristics of organic electrochemical transistors.....	47
A. Introduction.....	47
B. Effect of contact resistance on transfer curves.....	50
C. The disorder model	53
1. Model description and data fitting	53
2. Discussion of fit parameters.....	54
3. Comparison with non-uniform mobility model	55
4. Discussion.....	58
D. Conclusion	59
Chapter IV Time domain modeling of OECT behavior.....	60
A. Introduction.....	60
B. Faster than ionic response	61
1. Background.....	61
2. 20 μ s step response	62

C. Discrete circuit model for OEET transient response.....	65
D. Discrete model results.....	68
1. Predicting OEET output.....	68
2. Extracting material and device parameters	71
3. Limitations of the discrete model.....	72
4. Extending the discrete model – non-monotonic transconductance.....	73
5. Extracting the input signal	77
E. Conclusion.....	79
Chapter V Future Work	81
A. Sub-threshold voltage swing.....	81
B. OEET-based neuromorphic devices.....	83
C. OEET stability	91
Bibliography	95
Appendix I: Supporting material for chapter II	112
A. Chapter II experimental details.....	112
1. Fresnel lens	112
2. Ion transport measurements	114
3. Simultaneous electrical and optical measurements of OEETs.....	116
B. Supplementary details about chapter II.....	118
1. Optical measurements.....	118
2. Modifications to the Bernards-Malliaras model	122
3. Transient electrical response.....	129
4. Calculation of expected transconductance.....	132
Appendix II: Supporting material for chapter III.....	134
A. Derivation of the disorder model	134
B. Contact resistance measurements.....	139
C. Experimental details:.....	142
1. Fabrication	142
2. Characterization	143
3. Data fitting	145
Appendix III: Supporting material for chapter IV	146
A. Discrete Model Derivations	146
1. Step response	148
2. Frequency domain response.....	148
B. Experimental non-idealities:	151

1. Long-term current drift	151
2. Error between predicted and measured current at $t = 0$	151
3. Device stability	155
C. Experimental details.....	155
1. OECT fabrication.....	155
2. Characterization	156
3. Estimation of parameter uncertainty	156

Tables

Table III-A. Fit parameters for the disorder model.....	55
---	----

Figures

Figure I-1. Comparison of an OECT with an OFET.	2
Figure I-2. OECT operation and molecular structure of PEDOT:PSS	5
Figure I-3. Output and transfer curves for a typical OECT.	6
Figure I-4. Device structure and transfer curves for Pickup et al.'s "triode-type" device. ¹⁵ Panel (b) is reprinted with permission from <i>J. Electrochem. Soc.</i> , 131, 833-839 (2003). Copyright 1984, The Electrochemical Society	7
Figure I-5. Screen-printed OECT logic circuits. Image adapted from <i>IEEE Trans. Electron Devices</i> 62, 4231-4236 (2015) and reprinted with permission. Copyright © 2015, IEEE.....	11
Figure I-6. OECT array used for in vivo electrocorticographic measurements of epilepsy in a rat brain. Reprinted with permission from <i>Chem. Mater.</i> 26, 679-685 (2014). Copyright 2014 American Chemical Society	13
Figure I-7. Design and output of OECT-based neuromorphic elements. Panels (a) and (b) are reprinted with permission from <i>Adv. Mater.</i> 27, 7176–7180 (2015). Copyright 2015 WILEY-VCH Verlag GmbH & Co. KGaA, Weinheim. Panel (c) is reprinted with permission from <i>Nat. Mater.</i> 16, 414-418 (2017). Copyright 2017 Nature Publishing Group.....	15
Figure II-1. PEDOT:PSS electrochromism.....	20
Figure II-2. Typical structure of a polymer electrochromic device.	21
Figure II-3. Device structure and operation of an electrochromic Fresnel lens.....	24
Figure II-4. PEDOT:PSS absorption spectra as a function of voltage	25
Figure II-5. Device structure and optical measurements of the Stavrinidou de-doping front experiment. Data in (b) come from E. Stavrinidou et al. ⁹⁹	26
Figure II-6. Device structure and results of de-doping front measurement.	29
Figure II-7. OECT geometry and experimental setup for simultaneous optical/electrical measurements.....	35
Figure II-8. Output curves and hole concentration for a lateral OECT and best fit to Bernards model and nonuniform mobility model.	37
Figure II-9. The measured optical absorption increase plotted as a function of the predicted hole concentration.....	38
Figure II-10. Experimental fit of nonuniform mobility model to data from OECTs with liquid electrolyte.....	41

Figure II-11. Geometry scaling of fit parameters according to the nonuniform mobility model.	43
Figure II-12. Optimization of transconductance at saturation drain voltage	45
Figure III-1. OEECT geometry, polymer structures, and steady-state characteristics.....	49
Figure III-2. Gated four point probe measurements of OEECT transconductance.....	52
Figure III-3. Transmission line method measurements for contact resistance in OEECTs	53
Figure III-4. Disorder model fit to OEECT transconductance	54
Figure III-5. Comparison of disorder model (chapter III) with the non-uniform mobility model (chapter II) and the VM model. ¹¹⁹	57
Figure IV-1. Structure and operation of a typical OEECT with a PEDOT:PSS channel	62
Figure IV-2. Step response of an OEECT demonstrating faster than ionic response	64
Figure IV-3. Frequency domain and time domain responses for a PEDOT:PSS-based OEECT ...	69
Figure IV-4. Frequency domain and time domain responses for an OEECT made with the undoped polythiophene, p(g2T-TT).	71
Figure IV-5. Extending the discrete model by incorporating the disorder model.	75
Figure IV-6. Measured current response and extracted voltage input for an OEECT	78
Figure IV-7. Block diagram describing the method for using the discrete model to extract an unknown voltage signal from a measured current response.	79
Figure V-1. Conductivity, transconductance, and voltage swing predicted by the disorder model introduced in chapter III.	83
Figure V-2. ENODE layout and typical pre-synaptic and post-synaptic time series. Data in (b) are from Van de Burgt et al. ⁸¹	84
Figure V-3. Presynaptic voltage and postsynaptic current for a PEDOT:PSS-based ENODE	85
Figure V-4. Circuit diagrams and input-output characteristics of SPICE models for ENODEs. .	87
Figure V-5. Physical layout and SPICE circuit representing the ENODE with multiple gate inputs.	90
Figure V-6. Time-domain response of an ENODE to one, two, and three connected gates	91
Figure V-7. Gate current and drain current responses to a gate voltage step	93
Figure V-8. Cyclic voltammograms of the gate circuit in an OEECT at different temperatures....	95

Figure VII-1. Experimental setup for measuring the Fresnel zone plate lenses.	114
Figure VII-2. Description of spatial averaging for absorption measurements.....	119
Figure VII-3. (a) OECT channel with the perimeters of the cropped regions shown in red. (b) Absorption profile for the uncropped image with $V_G = 400$ mV and $V_D = -50$ mV	120
Figure VII-4 Measured absorption increase vs. predicted hole concentration	121
Figure VII-5. Raw images of the OECT channel during the floating electrode state and the low conductivity state.	122
Figure VII-6 Measured absorption increase versus the hole concentration predicted by the CLM model with different values of the CLM parameter	123
Figure VII-7. Range of predicted hole ratio values at a given absorption increase as a function of the CLM parameter	124
Figure VII-8. Range of predicted hole ratio values at a given absorption increase as a function of the contact resistance.	126
Figure VII-9. Range of predicted hole ratio values at a given absorption increase as a function of the ratio of the voltage dependent capacitance coefficient to the constant capacitance coefficient	127
Figure VII-10. Range of predicted hole ratio values at a given absorption increase as a function of disorder parameter	128
Figure VII-11. Range of predicted hole ratio values at a given absorption increase as a function of the unitless parameter appearing in the exponential dependence of mobility on hole concentration.....	129
Figure VII-12. Typical transient electrical response of an OECT after the application of a positive gate voltage	130
Figure VII-13. Typical transient electrical response of a gel-electrolyte OECT after the application of a positive gate voltage.	131
Figure VII-14. Typical transient electrical response of a liquid-electrolyte OECT after the application of a positive gate voltage.....	132
Figure VII-15. Linear fit to the absorption vs. hole concentration	133
Figure VIII-1. Disorder model predictions for OECTs.	138
Figure VIII-2. Measured voltage in the channel of a PEDOT:PSS-based OECT.	140
Figure VIII-3. Measured voltage near the source of a PEDOT:PSS-based OECT.	141

Figure VIII-4. Normalized contact resistance at the drain electrode.	142
Figure IX-1. Circuit diagram for the Discrete Model description of an OECT (see chapter IV).	146
Figure IX-2. Ratio of gate to drain current as a function of the input frequency.	150
Figure IX-3. Long-term current drift in an OECT	151
Figure IX-4. The raw data and model fits for the results shown in Figure IV-3a and Figure IV-3b.	153
Figure IX-5. The raw data and model fits for the results shown in Figure IV-2a-c in chapter IV.	154
Figure IX-6. Response of a PEDOT:PSS-based OECT to a square pulse train at the gate electrode.	155

CHAPTER I INTRODUCTION

A. Background

Organic electrochemical transistors (OECTs) are thin-film transistors with an organic semiconductor channel between source and drain electrodes. OECTs are structured much like organic field-effect transistors (OFETs) with the distinction that OECTs have an electrolyte layer between the channel and the gate electrode instead of a standard dielectric, as shown in Figure I-1. In 1984, H. S. White et al. reported the first OECTs, demonstrating that the conductivity of a polypyrrole channel could be reversibly modulated by changing its redox state with a gate electrode in an electrolyte.¹ Since that time, researchers have fabricated OECTs with many different materials and geometries and have demonstrated the usefulness of OECTs in a variety of applications. However, several gaps remain in the understanding of OECT behavior. Existing models have been useful for the design of OECT sensors and circuits, but they fail to properly incorporate polymer physics. This has prevented these models from predicting several widely-observed characteristics of OECTs. In particular, prior to the work in this thesis, no models quantitatively described spatially-resolved optical absorption measurements in OECT channels (chapter II), non-monotonic transconductance* as a function of gate voltage (chapter III), and OECT output currents that respond more than 30 times faster than the gating current (chapter IV). This thesis addresses all of these gaps in the understanding of OECT behavior. It highlights the influence that material properties have on the device physics of OECTs, and it describes three original models for predicting the steady-state and transient response of OECTs. These models provide quantitative explanations for the previously unexplained characteristics described above,

* Transconductance, g_m , is defined as the derivative of the transistor's output current with respect to the gate voltage. $g_m \equiv \left[\frac{\partial I_D}{\partial V_G} \right]_{V_D}$, where I_D is the drain current, V_G is the gate voltage, and V_D is the drain voltage.

and, although each model describes a different regime of OECT behavior, they are all consistent with each other. Ultimately, these models inform the design of OECT sensors and circuits, and they provide a way to measure the material properties of the polymer semiconductors used in OECTs, thus aiding the development of new polymers for performance optimization in different applications.

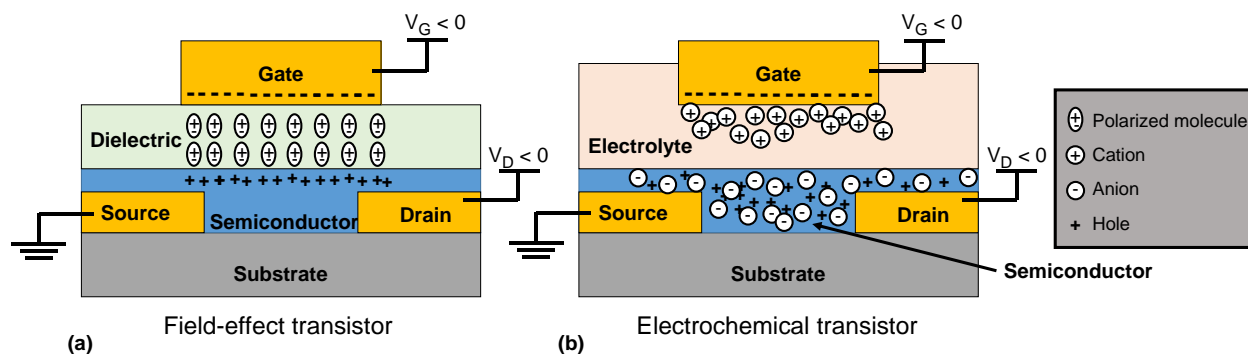


Figure I-1. Typical structure for an OFET (a) and an OECT (b). In the OFET, immobile molecules in the dielectric are polarized by a gate voltage. Charge transport in the semiconductor occurs at the interface of the semiconductor and dielectric. In the OECT, mobile ions are pushed from the electrolyte into the semiconductor by a gate voltage. These ions dope (or de-dope) the semiconductor. Charge transport occurs throughout the volume of the OECT.

This chapter will provide background information about OECT behavior and the use of OECTs in various applications. This background motivates the models discussed in later chapters and explains the fundamental physics that underlie the details of those models. In the following sections, we will first explain the principles of OECT operation. Then we will consider several existing models for OECT behavior. Finally, we will discuss applications for OECTs.

B. OECT operating principles

As mentioned in section A, OECTs have a structure similar to that of OFETs, and they operate according to similar principles. When a voltage, V_D , is applied between the source and drain electrodes, a current flows through the semiconductor channel and is collected at the drain. This current is the output current of the OECT and is called the drain current, I_D . At low drain voltages, the channel conductivity is independent of drain voltage, so the drain current is directly

proportional to the drain voltage according to Ohm's law. The gate electrode, though not directly connected to the channel, can also modulate the drain current. When a voltage is applied at the gate electrode, it creates an electric field that pushes ions from the electrolyte into the semiconductor channel. The effect of these ions on channel conductivity depends on the properties of the semiconductor in the channel. In p-type semiconductors, positive gate voltages decrease channel conductivity, and negative gate voltages increase channel conductivity. Conversely, positive gate voltages increase channel conductivity in n-type semiconductors while negative gate voltages decrease channel conductivity. OEETs can also be classified as "depletion-mode" or "accumulation-mode" transistors. Depletion-mode transistors are highly conductive at $V_G = 0$ V and become less conductive when a gate voltage is applied. Accumulation-mode transistors behave in the opposite way. They are non-conductive at $V_G = 0$ V and become more conductive in response to a non-zero gate voltage.

For concreteness, consider an OEET with the p-type semiconductor poly(3,4-ethylenedioxythiophene):poly(styrenesulfonate), or PEDOT:PSS. PEDOT is a conjugated polymer with semiconducting properties and a stable oxidized form,^{2,3} and PSS allows the PEDOT to be dispersed in water.⁴ In addition to solubilizing PEDOT, the PSS also acts as an acceptor ion, forming an ionic bond with the PEDOT and withdrawing electronic charge density, as shown in Figure I-2b.⁵ This gives the PEDOT positively charged electronic carriers, making it a p-type semiconductor and endowing it with conductivity greater than 800 S/cm in its oxidized form.^{6,7} Because the PEDOT:PSS is naturally in a conductive state, OEETs using PEDOT:PSS are classified as p-type, depletion-mode transistors. When a positive voltage is applied at the gate electrode, it creates a field that pushes cations from the electrolyte into the semiconductor channel, as shown in Figure I-2a. These cations form ionic bonds with the PSS,

displacing it from the PEDOT. Without the ionically-bound PSS dopants, holes are no longer coulombically stable on the PEDOT backbone, so the PEDOT⁺ is reduced from its conductive state to its insulating neutral state, PEDOT⁰. This de-doping (reduction) process is described in equation (I.1) and is reversible; when the gate voltage, V_G , returns to 0 V, the cations diffuse back out of the channel, and the PSS forms new ionic bonds with the PEDOT, oxidizing it to its conductive state, PEDOT⁺.



The left-hand side of equation (I.1) represents the situation when $V_G = 0$ V. In this case cations, M^+ , are in the electrolyte, PEDOT forms an ionic bond with PSS, and holes are on the PEDOT chain. The right-hand side of equation (I.1) represents the situation when $V_G > 0$. In this case, the PEDOT chain is neutral, cations form ionic bonds with the PSS, and holes, h^+ , are removed from the channel. Although, OECTs can use materials other than PEDOT:PSS,⁸⁻¹² the basic principles delineated above still describe device behavior as long as appropriate adjustments are made when considering n-type or accumulation-mode OECTs.

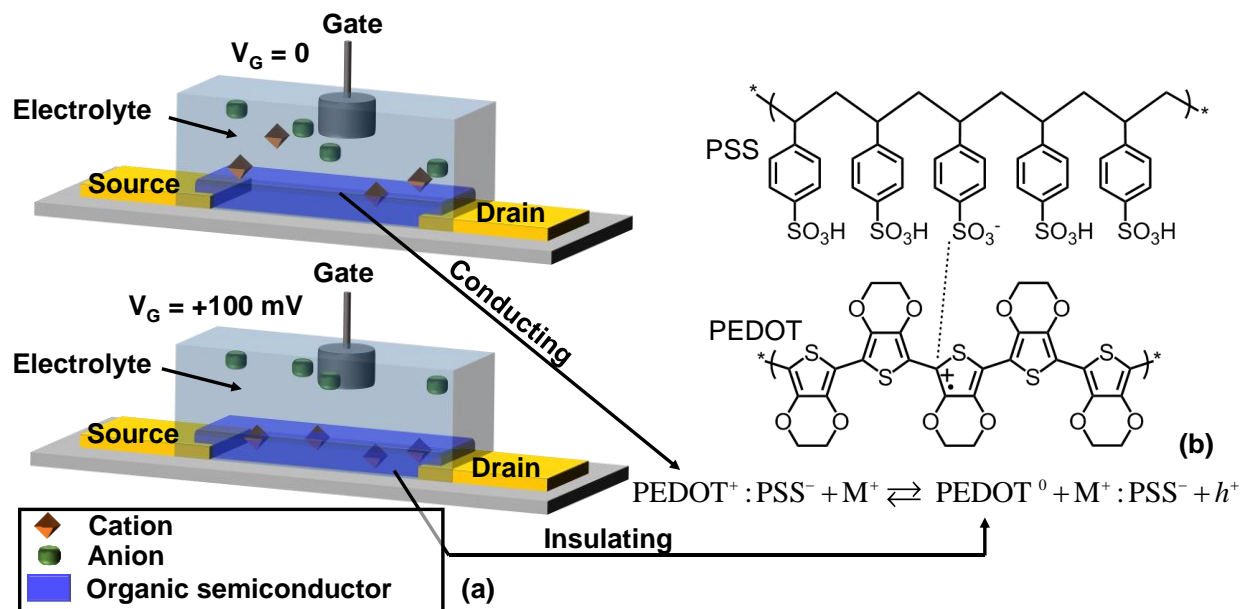


Figure I-2. OECT operation in depletion mode (a) and molecular structure of PEDOT:PSS (b). The dashed line between the PEDOT and PSS represents an ionic bond that leaves a radical cation on the PEDOT chain. In panel (a), the top image represents the OECT in its ON state at $V_G = 0 \text{ V}$. The bottom image represents the OECT in its OFF state at $V_G = 100 \text{ mV}$.

To characterize OECT performance, researchers usually present output and transfer curves, which show the dependence of drain current on V_D and V_G , respectively. An example of typical output and transfer curves is shown in Figure I-3. These plots are similar to the expected output and transfer curves for long-channel, depletion-mode, p-type MOSFETs:¹³ The channel current has a linear dependence on V_D at low voltages, but saturates for higher values of V_D . Also, for a fixed V_D , the magnitude of the drain current decreases as V_G becomes more positive. Because of these qualitative similarities between OECT and MOSFET behavior, researchers have used MOSFET models to describe OECT behavior, as discussed in the next section.

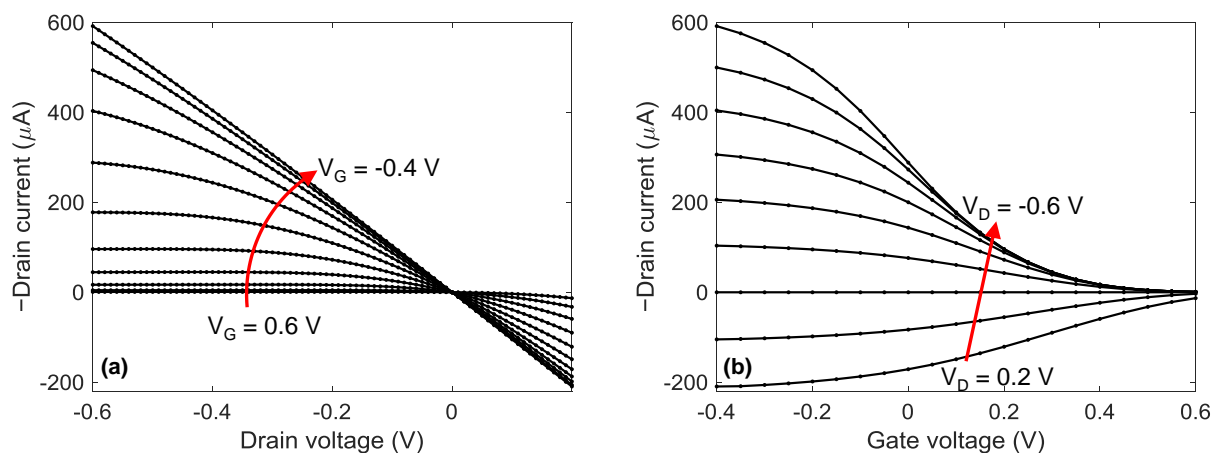


Figure I-3. Output (a) and transfer (b) curves for a typical OEET. Each curve in (a) is for a single gate voltage between 0.6 V and -0.4 V in 0.1 V steps, as indicated in the figure. Each curve in (b) is for a single drain voltage between 0.2 V and -0.6 V in 0.1 V steps, as indicated in the figure.

C. Models for OEET behavior

As stated in the introduction, most researchers regard the device reported by White, et al. as the first OEET.¹ However, before this work, other researchers had developed three-electrode organic electrochemical devices with current-voltage relationships similar to that of White's transistor. In particular, P. G. Pickup, et al. developed a "triode-type device" consisting of a polymer film sandwiched between two metal electrodes, as shown in Figure I-4.^{14,15} The current through the polymer was controlled with a third electrode to adjust the redox state of the polymer. Pickup et al., published the transfer curves of their devices and presented a simple analytical expression describing how the current through the polymer depended on the applied voltages. This expression was based on the Nernst equation and assumed diffusion-based current only, neglecting the contribution of electronic drift current. While this equation was useful for interpreting the results of their experiments, Pickup et al. did not attempt to use it for quantitative fits to their data.

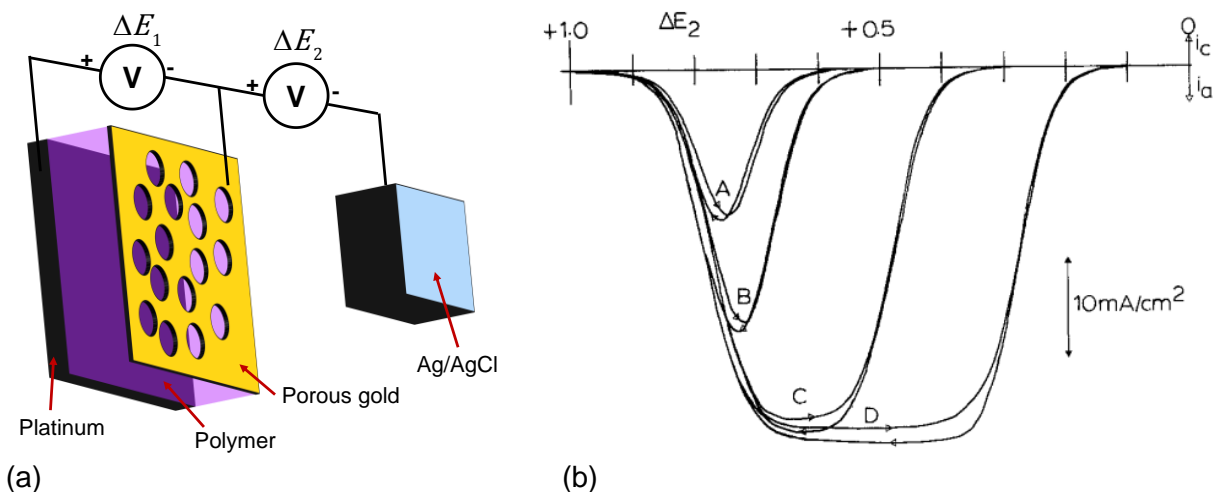


Figure I-4. Device structure (a) and transfer curves (b) for Pickup et al.'s "triode-type" device.¹⁵ Panel (a) shows the device structure and electrical connections. Also, although not shown here, the entire device is immersed in an electrolyte. Panel (b) shows the output current as a function of ΔE_2 (in V) at fixed values for ΔE_1 of 50 mV (A), 100 mV (B), 300 mV (C), and 500 mV (D). Panel (b) is reprinted with permission from *J. Electrochem. Soc.*, 131, 833-839 (2003). Copyright 1984, The Electrochemical Society.

After the work of Pickup et al., many reports of OEETs and OEET-like devices appeared in the literature,¹⁶⁻²³ but no authors focused on providing quantitative models for OEET behavior until N. D. Robinson et al. in 2006.²⁴ These researchers developed a quantitative model for OEETs. They used the Nernst equation to determine the concentration of oxidized PEDOT as a function of voltage, and they used the Poisson equation and Ohm's law to calculate the current as a function of voltage and PEDOT⁺ concentration. Robinson et al. did not provide an analytical expression for the drain current as a function of gate and drain voltage. Instead, they described a numerical simulation to calculate drain current, and they made qualitative comparisons between the predictions of their model and their experimental data. One of the most important findings from this work is that the conductivity of PEDOT:PSS in an OEET channel is not directly proportional to the carrier concentration, motivating the research presented in chapters II and III of this thesis.

In contrast to Pickup et al. and Robinson et al.'s electrochemistry-based development of OECT models, later researchers approached the problem from a solid-state device perspective. For instance, in 2006, shortly after Robinson et al.'s model was published, Y.-J. Lin et al. used an adaptation of the standard model for long-channel p-type MOSFETs to extract hole mobility from OECT measurements.²⁵ In 2007, D. A. Bernards and G. G. Malliaras formalized this approach and published a detailed model for OECT behavior, again based on the standard model for long-channel p-type MOSFETs.²⁶ Bernards and Malliaras explained OECT behavior as an electronic circuit branch in the channel coupled to an ionic branch between the gate and channel. They modeled the channel exactly like a p-type MOSFET, and they modeled the ionic circuit as an ionic resistor in series with a capacitor. The capacitor represents the ionic capacitance of the OECT channel and determines the amount of electronic charge induced in the channel via electrochemical doping. Unlike previous models, the Bernards model provided an analytical expression and quantitatively fit experimental data, providing a way to extract hole mobility and ionic capacitance from transistor measurements. Despite the simplicity and utility of this model, it describes the OECT channel exactly like a crystalline semiconductor. Therefore, it assumes that hole mobility is independent of applied voltage. Because of this assumption, the Bernards model fails to explain spatially-resolved optical measurements of OECTs and fails to predict a non-monotonic transconductance-voltage relationship – two issues that later chapters of this thesis will address.

Subsequent work from the Malliaras research group built on the Bernards model, providing additional insight about OECT optimization and behavior. For example, D. A. Bernards, et al. showed that enzymatic reactions in an OECT electrolyte cause charge transfer at the gate electrode and effectively shift its voltage. Adding this voltage shift to the MOSFET-

based model provides a quantitative framework for measuring metabolite concentrations with OECTs.²⁷ Later, J. Rivnay et al. advanced the understanding of OECT behavior by showing that the ionic capacitance of an OECT channel is directly proportional to the channel volume. This finding proved that OECTs undergo electrochemical doping throughout the bulk of the channel. Because OFET channels only experience conductivity modulation at the semiconductor/dielectric interface, Rivnay's finding highlighted an important distinction between OFETs and OECTs, and it explained why OECTs, unlike FETs, exhibit a channel conductance and transconductance that are directly proportional to film thickness.²⁸ Rivnay pointed out that this information provides a design tool for OECT optimization. Researchers who desire OECTs with high-sensitivity to small changes in gate voltage should fabricate devices with thick semiconducting channels. However, because channel capacitance also increases with channel thickness, researchers who want OECTs with fast responses should use thin channels. Rivnay also points out that the volumetric capacitance of OECT channels endows them with a capacitance per unit volume more than two orders of magnitude greater than that in conventional FETs – and even compared to FETs with high-k dielectrics.²⁹ While Rivnay et al.'s work allows order of magnitude predictions about how this capacitance affects device response speed, it does not describe how the interplay between the charging current and channel current affect the shape of the OECT output current. Chapter IV of this thesis addresses this issue and provides a model that shows how the unprecedented capacitance in OECTs allows the speed of the output current to exceed the speed of the charging current by a factor of 30 in certain situations. Finally, in addition to providing a better understanding of OECT behavior, Rivnay et al.'s work also provides clear motivation for the use of OECTs instead of OFETs. Because OECTs rely on volume doping while OFETs rely on interfacial doping, OECT channels can have much higher

conductance and transconductance than OFET channels. Therefore, OECTs are a leading technology for applications that require high transconductance, as we will discuss in the next section.³⁰

D. Applications for OECTs

Since their discovery in the early 1980s, OECTs have been used in myriad different applications. In this section, we discuss OECTs in integrated circuits, biosensors, and neuromorphic systems.

Less than ten years after the first reported OECT, C. H. McCoy and M. S. Wrighton demonstrated the first OECT-based integrated circuit.³¹ They fabricated a push-pull amplifier consisting of a polyaniline OECT integrated with a polythiophene OECT. McCoy and Wrighton's push-pull amplifier worked like inorganic push-pull amplifiers consisting of bipolar junction transistors. However, unlike inorganic push-pull amplifiers, McCoy and Wrighton's device did not suffer from crossover distortion³² because the complementary OECTs turned on at the same V_G polarity despite having opposite I_D vs. V_G slopes at the turn-on voltage.

Later development of OECT-based integrated circuits focused on logic elements. For example, in 2005 D. Nilsson et al. made OECT-based inverters, NAND gates, and NOR gates.³³ Additionally, they showed that the inverters were uniform enough to be used in 5-stage ring oscillators. Several years later, R. Mannerbro, et al. reported similar results with inkjet-printed OECTs and interconnects.³⁴ Also focusing on printed electronics, engineers at Joanneum Research reported what is, as of 2017, the highest degree of integration for OECT-based logic circuits. They fabricated all-screen-printed logic gates and demonstrated a remarkable level of device reproducibility. Because of the scalable fabrication method and the device uniformity, P. Hütter et al. were able to create functioning flip-flops and 2-bit shift registers that required the integration of 36 OECTs.³⁵ The design and output of these flip-flops is shown in Figure I-5.

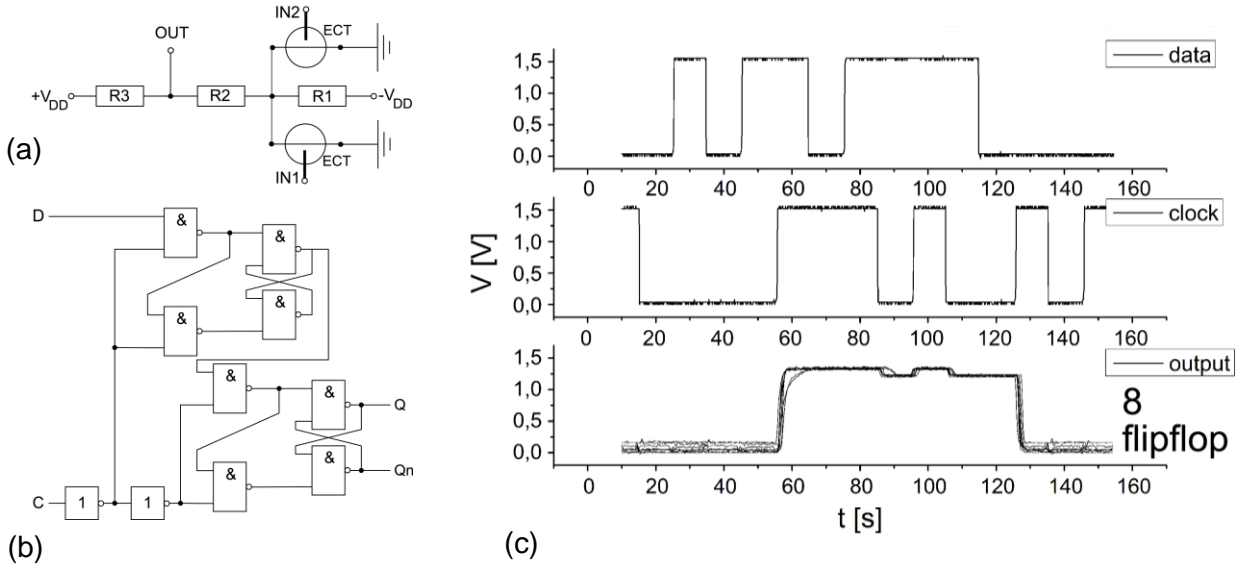


Figure I-5. Screen-printed OECT logic circuits. Panel (a) shows the circuit diagram for a NAND gate where ECT is the label for an OECT, and R1, R2, R3 represent printed resistors. Panel (b) shows the circuit diagram for a flip-flop using 8 NAND gates and 2 inverters. Panel (c) shows the input and output of 8 different printed flip-flops.³⁵ Figures are adapted from IEEE Trans. Electron Devices 62, 4231-4236 (2015) and reprinted with permission. Copyright © 2015, IEEE.

Despite these examples of successful OECT-based integrated circuits, researchers must consider whether this is a feasible application area for OECTs. One reason OECTs might not be useful in integrated circuits is their relatively low operating frequencies. For instance, the fastest reported OECTs operate between 10 kHz and 50 kHz,^{28,36,37} which is about three orders of magnitude slower than the fastest OFETs.³⁸ Moreover, even the performance of off-the-shelf inorganic transistors exceeds the speed of state-of-the-art OFETs by about three orders of magnitude.³⁹ Therefore, if high-speed operation is desired, as in most integrated circuits, using OECTs is a poor choice. Notwithstanding the low speed of OECTs, a common claim in the literature is that OECTs can find a niche in integrated circuits when physical flexibility is a key requirement. Unfortunately, this claim also rings hollow because engineers have made flexible, high-performance inorganic transistors, with GHz operating frequencies.^{40,41} Another challenge for using OECTs in integrated circuits is the tendency for device parameters to drift as a result of bias stress or environmental factors, as noted by researchers who propose using OECTs in hybrid

organic-inorganic circuits.⁴² These scientists suggest using hybrid circuits with fast, stable inorganic chips for data processing and with OECTs for biosensing, a role they are particularly well-suited for, as discussed below.

OECTs possess several characteristics that make them successful biosensors. For instance, PEDOT:PSS is biocompatible⁴³⁻⁴⁷ and ~ 2-3 orders of magnitude softer than silicon.⁴⁸ This means that compared to silicon, PEDOT:PSS can more easily conform to 3D biological systems⁴⁹ and has a lower impact on cell and tissue samples.⁵⁰ Additionally, OECTs are designed to operate in electrolytes, so cell culture media does not necessarily harm OECT performance. Another advantage of OECT-based biosensors is that PEDOT:PSS and other organic semiconductors, unlike inorganic semiconductors, possess both electronic and ionic conductivity. This ionic conductivity greatly reduces the impedance of PEDOT:PSS to ion-based cellular signaling, thus permitting the detection of low-level signals.^{51,52} Finally, as mentioned earlier, OECTs have high transconductance compared to other transistor technologies because of volumetric charge storage and conduction.^{28,30} This high transconductance allows OECTs to make high-fidelity recordings of sub mV biological signals.

The properties mentioned above allow researchers to use OECTs for a wide range of applications.^{51,53} For example, OECT-based enzymatic sensors can measure the concentration of glucose,^{20,23,27,54-56} lactate,^{57,58} penicillin,⁵⁹ acetylcholine,⁶⁰ ethanol,⁶¹ and dopamine.⁶² OECTs can also measure epithelial cell integrity⁶³⁻⁶⁵ and detect complementary DNA strands down to pM concentrations.⁶⁶ Not only can OECTs detect biologically-relevant chemical species, but they can also directly sense the electrical activity of electrogenic cells. For instance, researchers have demonstrated that OECTs can record electrocardiographic waveforms,⁶⁷ measure single-

cell cardiac action potentials,⁶⁸ and make in vivo measurements of epileptic activity (see Figure I-6).⁶⁹

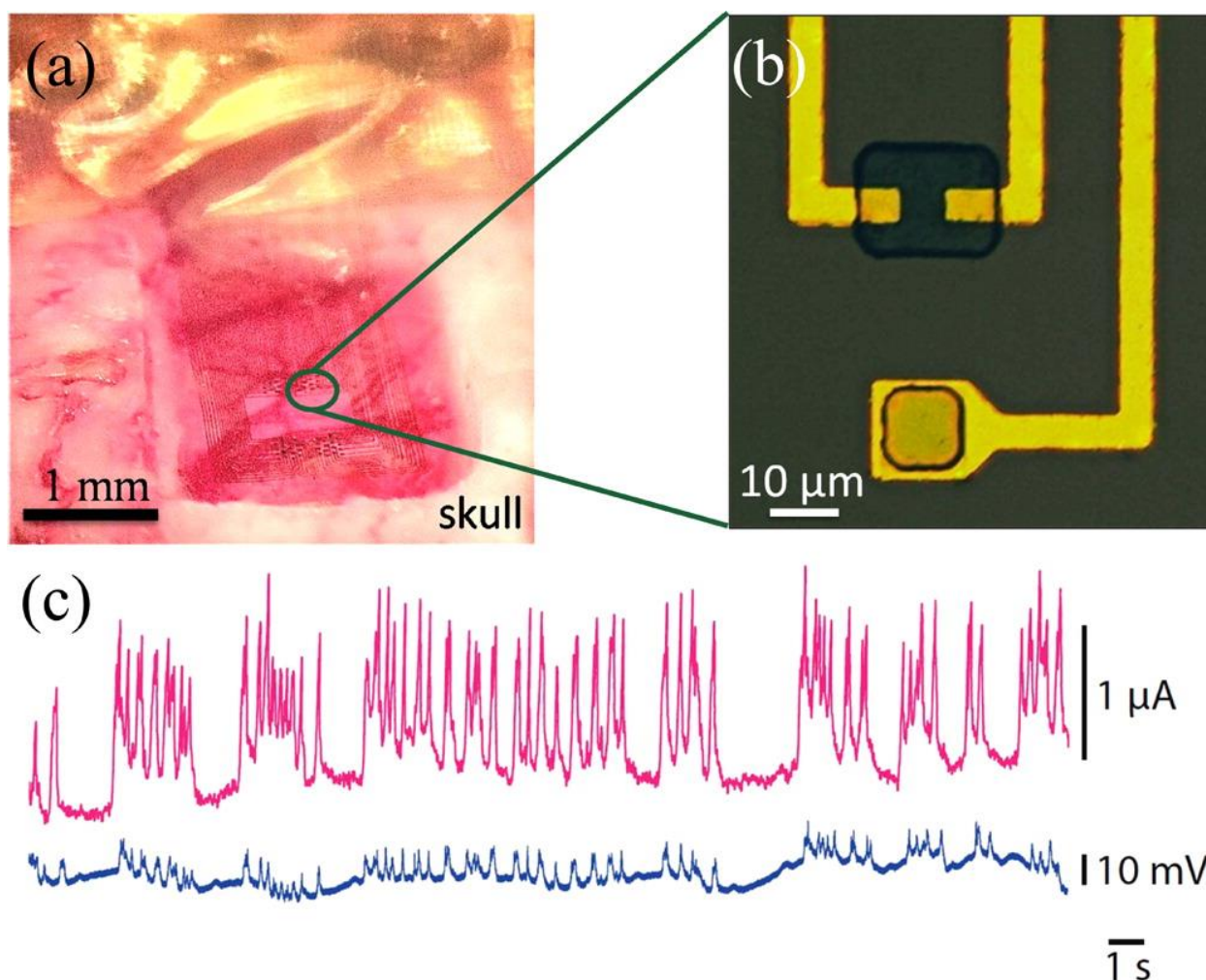


Figure I-6. OECT array used for in vivo electrocorticographic measurements of epilepsy in a rat brain. (a) Image showing the full array of OECTs on the surface of the skull. (b) Magnified view of a single OECT in the array. (c) OECT recording of neural activity (upper trace, pink) compared with a recording from a passive electrode (lower trace, blue).⁷⁰ Reprinted with permission from Chem. Mater. 26, 679-685 (2014). Copyright 2014 American Chemical Society

Neuromorphic engineering is another application for OECTs, and compared to integrated circuits and biosensing, it is a much more recent area for OECT applications. This field can generally be defined as studying “artificial neural systems whose architecture and design principles are based on those of biological nervous systems.”^{71,72} The motivation for developing such systems comes from the observation that biological systems are more efficient than

conventional computers at solving problems involving ill-conditioned input and relative, rather than absolute, computation.⁷² In particular, compared to computers, biological nervous systems are more defect-tolerant, require less physical volume, and require much, much less power to solve certain problems. For example, Watson, the computer that beat Ken Jennings in jeopardy, required a physical volume equivalent to that of approximately 10 household refrigerators and consumed 80 kW of power; whereas, the human brain consumes only about 20 W.⁷³

OECT-based neuromorphic systems have been demonstrated to mimic several behaviors of biological neurons. For example, as described in Figure I-7, many devices have shown spike-timing-dependent plasticity (STDP), in which the response to an input pulse depends not only on the amplitude and width of the pulse, but also on the history of previous pulses that had been applied.⁷⁴⁻⁷⁹ Another neuron-like behavior that OECTs can exhibit is memory, as reported by B. Winther-Jensen et al. These authors developed a PEDOT-based material that experiences a conformational change during reduction and oxidation.⁸⁰ This conformational change introduces a stable hysteresis in the polymer's conductivity as a function of applied voltage. P. Gkoupidenis et al. used this hysteresis as a memory function in OECTs made from this polymer and were able to demonstrate short-term to long-term memory transitions in their devices.⁷⁴ Another OECT-based device capable of storing memory states is the Electrochemical Neuromorphic Organic Device reported by Y. van de Burgt et al. in 2017.⁸¹ This device possesses hundreds of distinct memory states, and can store a single state for days at a time while consuming only pJ of energy per switching event. Finally, in addition to STDP and memory, OECTs have also demonstrated global connectivity⁸² similar to mechanisms of biological homeostatic plasticity which prevent neural circuits from becoming hyper- or hypo-active.⁸³

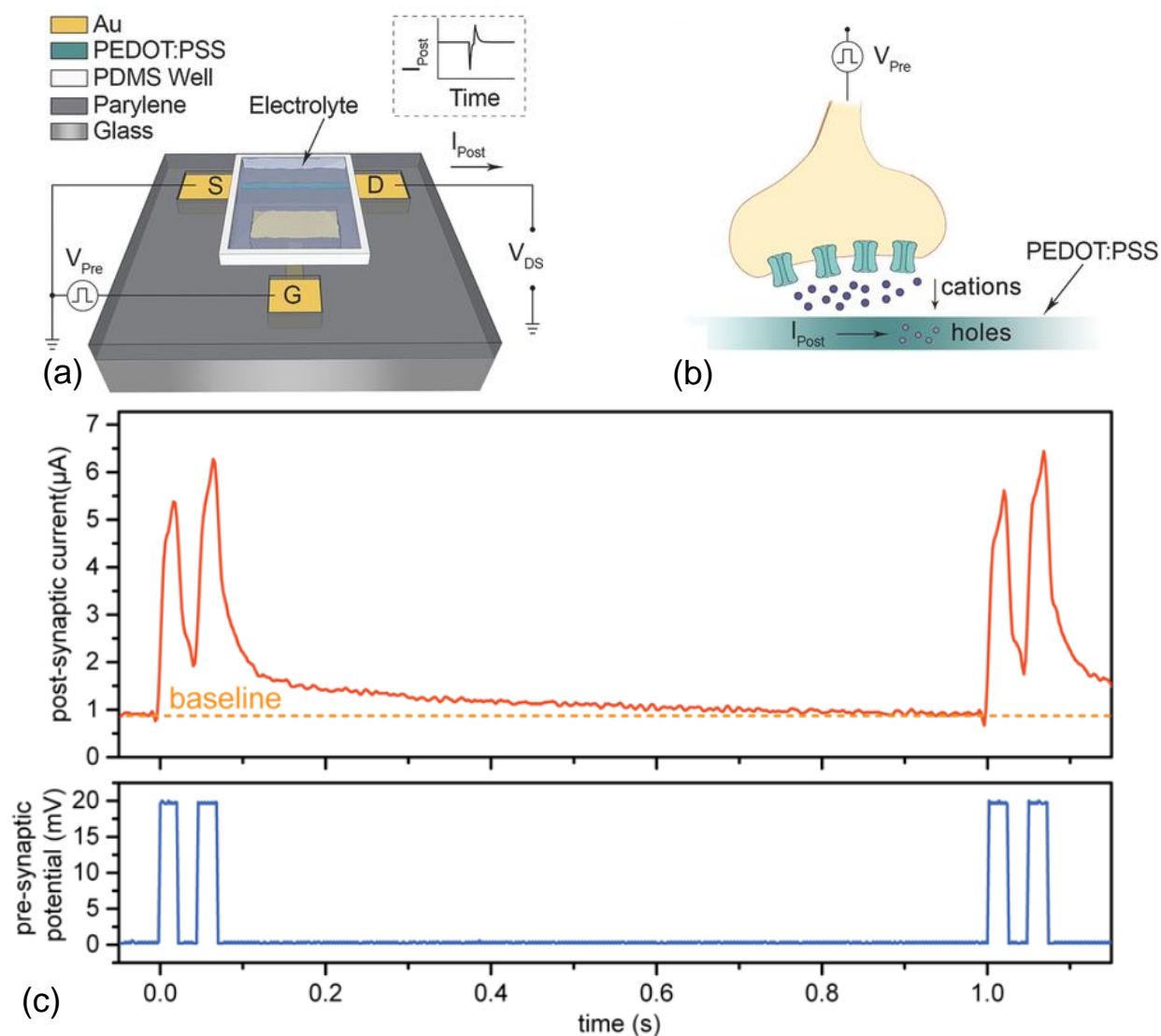


Figure I-7. Design and output of OECT-based neuromorphic elements. Panel (a) shows the design of an OECT-based artificial synapse and indicates the standard interpretation of presynaptic voltage at the gate electrode and post-synaptic current through the channel.⁷⁵ Panel (b) represents the analogy between an OECT and a biological synapse.⁷⁵ Panel (c) shows an example of STDP in an OECT. In this device, presynaptic spikes are excitatory, the post-synaptic current response is amplified when a presynaptic spike closely follows an earlier spike.⁸¹ Panels (a) and (b) are reprinted with permission from *Adv. Mater.* 27, 7176–7180 (2015). Copyright 2015 WILEY-VCH Verlag GmbH & Co. KGaA, Weinheim. Panel (c) is reprinted with permission from *Nat. Mater.* 16, 414–418 (2017). Copyright 2017 Nature Publishing Group.

E. Summary

OECTs are thin-film transistors with coupled ionic and electronic conductivity.

Researchers have developed predictive models for OECT behavior using electrochemistry and

solid-state device physics. These models, as well as novel materials and fabrication technology, have made OECTs useful in a wide range of applications including integrated circuits, biosensing, and neuromorphic systems. However, prior to the work presented in this thesis, most of the understanding of OECT behavior was built on imperfect analogies between OECTs and FETs with crystalline semiconductors. This prevented researchers from understanding several ubiquitous and important OECT characteristics. For example, the high transconductance of OECTs was well-known by researchers who used it for biosensing experiments. However, researchers also realized that OECTs had non-monotonic transconductance as a function of gate voltage.⁸⁴ This complicated use of OECTs as sensors, but it was not explained by existing models. In this thesis, we provide a quantitative explanation of this behavior by appealing to the physics of charge hopping in disordered semiconductors, and we describe how the resulting model can be used for material optimization. We also explore several other previously unexplained OECT characteristics.

Overall, this thesis advances the understanding of OECTs beyond analogies with FETs and shows how the material properties of polymer semiconductors affect the device physics of OECTs. In the following chapters of this thesis, we provide models that explain these effects and show how our models inform optimization of OECT design and material development. In chapter II, we first report combined optical and electrical characterization of OECTs, and we show that these measurements provide evidence that the simple MOSFET model for OECTs is inaccurate. Next, in chapter III we build on this finding and present a model for OECT behavior based on percolation transport in disordered materials, and we demonstrate that this model explains the non-monotonic transconductance in OECTs. Then, in chapter IV we describe a simple model for the time-domain behavior of OECTs and report OECTs with microsecond turn-

on transients that are more than 30 times faster than expected. Finally, in chapter V, we discuss some of the remaining gaps in the understanding of OECTs and consider opportunities for future research.

CHAPTER II

SIMULTANEOUS OPTICAL AND ELECTRICAL MEASUREMENTS REVEALING NON-UNIFORM HOLE MOBILITY IN OECTS

The optical properties of organic semiconductors have been thoroughly studied for the development of organic solar cells, light emitting devices, adaptive optics, and for basic material science. In this chapter, we discuss how optical measurements augment electrical characterization to improve understanding of OECTs. In particular, we use absorption measurements to provide evidence that the hole mobility in PEDOT:PSS is not constant but depends on the hole concentration. Additionally, we develop an analytical model for OECTs that explains this dependence of hole mobility on hole concentration. This model improves on existing models which describe OECTs in much the same way as FETs, and it allows researchers to more accurately estimate device and material parameters. This improved accuracy informs the optimization of OECT operation and can lead to 120% improvement in transconductance.

A. Background

1. Electrochromism in semiconducting polymers

Because polymer semiconductors have weak intermolecular bonds and low dielectric constants, their electronic and geometric properties are strongly coupled, and charged species experience significant coulombic interactions with each other. These characteristics endow organic semiconductors with unique electro-optic properties that are not observed in inorganic semiconductors. In this chapter, we will focus on one of these properties – electrochromism, or electrically-controlled changes in optical absorption. In particular, we will consider electrochromism in PEDOT:PSS even though many other organic semiconductors also possess this property.^{10,85–87}

Electrochromism in PEDOT:PSS is a result of the structural distortion that occurs on a PEDOT chain when it is oxidized. This structural distortion alters the energetic landscape of the

polymer and creates electronic states in the middle of the gap between the highest occupied molecular orbital (HOMO) band and the lowest unoccupied molecular orbital (LUMO) band, as depicted in the energy diagrams shown in the insets of Figure II-1a,b.⁸⁸ The creation of these mid-gap states allows lower energy optical transitions, creating a new absorption peak at longer wavelengths while decreasing the absorption due to HOMO-LUMO transitions.⁸⁹ These spectral changes cause PEDOT to change colors when it is oxidized; neutral PEDOT has an absorption peak near 600 nm, so it appears blue, but oxidized PEDOT has an absorption peak in the infrared (IR), so it appears transparent, as shown in Figure II-1.

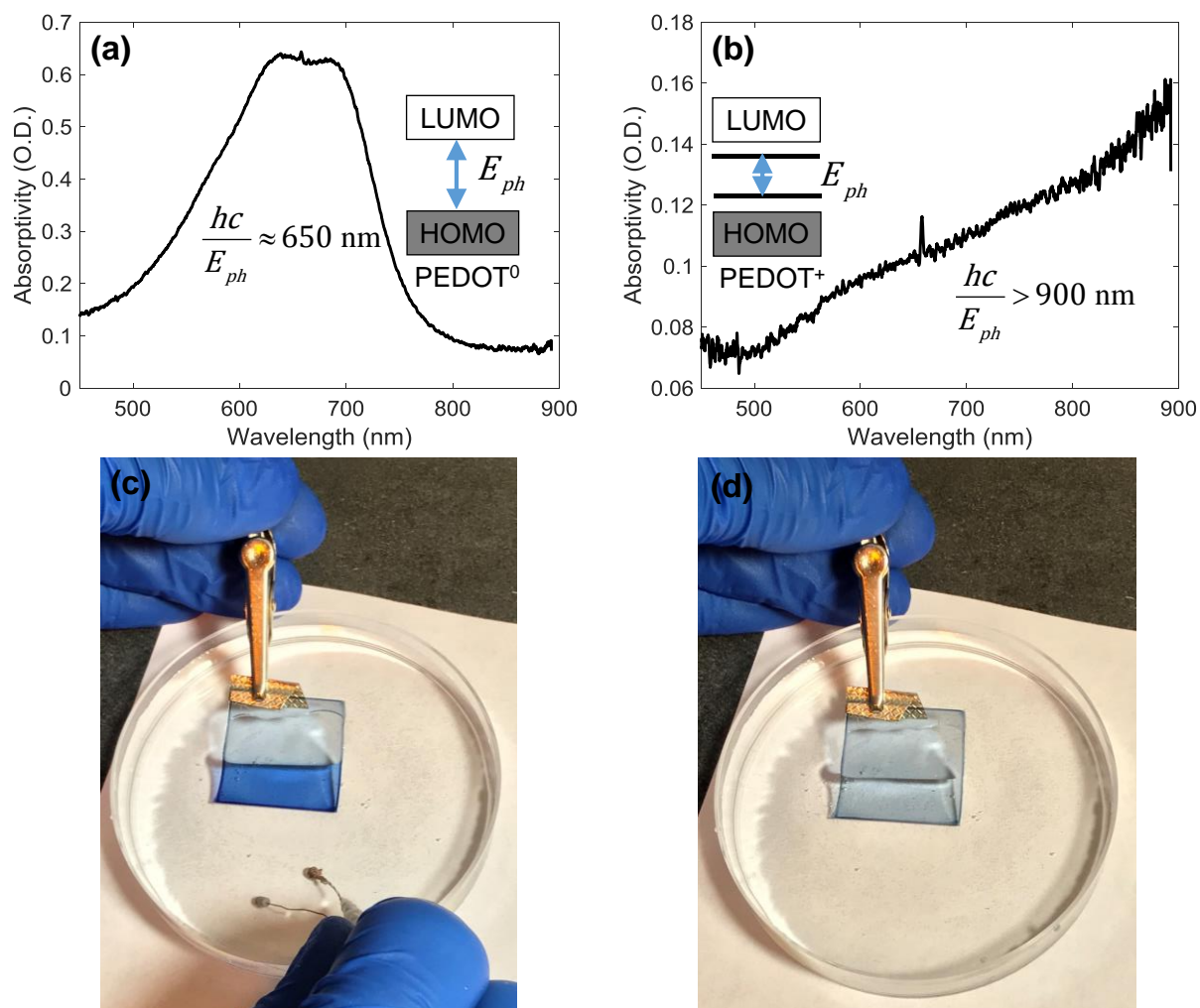


Figure II-1. PEDOT:PSS electrochromism. Panels (a) and (b) show the absorption spectra of reduced PEDOT:PSS (a) and oxidized PEDOT:PSS (b). The insets in (a) and (b) show the respective band diagrams. Panels (c) and (d) show photographs of reduced (c) and oxidized (d) PEDOT:PSS.

2. Applications for electrochromism

Engineers use this electrically-induced color change in a variety of applications such as electrochromic displays and electrically tunable lenses. A typical structure for electrochromic devices includes a transparent conducting oxide (TCO), an electroactive PEDOT:PSS layer, an electrolyte on top of the PEDOT:PSS, and a counter electrode in the electrolyte, as described in Figure II-2. These devices operate according to principles similar to those introduced in chapter I for OECTs. Applying a positive voltage at the counter electrode reduces the PEDOT to its

neutral state, making it a blue color; and applying a negative voltage oxidizes the PEDOT, making it transparent.

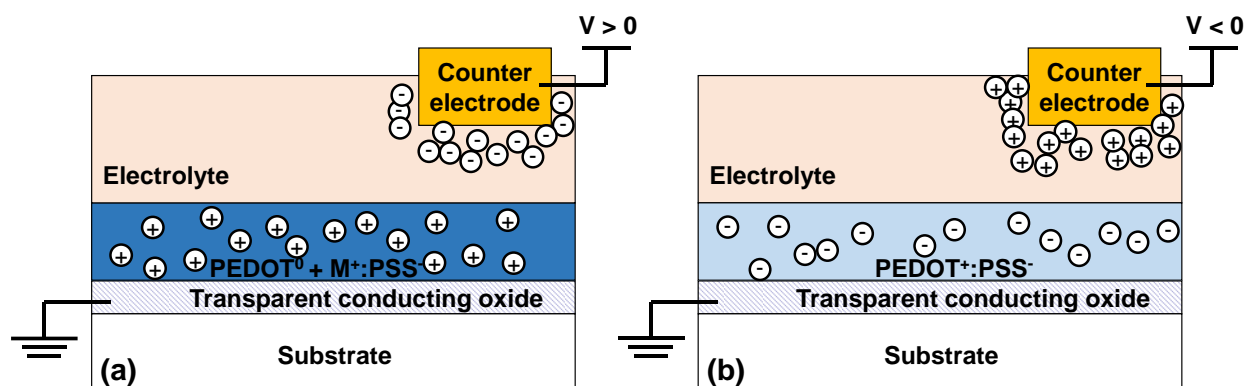


Figure II-2. Typical structure of a polymer electrochromic device. Panel (a) shows the device with reduced PEDOT, which strongly absorbs visible light in the red part of the spectrum. In panel (b), the PEDOT is oxidized and transparent at visible wavelengths.

Applications for PEDOT:PSS-based electrochromic devices were demonstrated as early as 2002 when P. Andersson, et al. fabricated a 4×10 array of individually addressable electrochromic pixels by integrating electrochromic devices with OECTs.⁹⁰ Other engineers used similar techniques and materials to make switchable diffractive optical devices.^{86,91–93} For example, S. Admassie and O. Inganäs patterned PEDOT:PSS films into grating structures with stripes of PEDOT:PSS on indium tin oxide (ITO).⁹³ In these structures, at 0 V applied between the film and the counter electrode, the PEDOT:PSS is $\sim 85\%$ transparent and contrasts only weakly with the ITO. However, when a positive voltage is applied, the PEDOT:PSS darkens, and the lines contrast more strongly with the ITO, forming an absorptive diffraction grating. The increased optical contrast causes the intensity of diffracted light to double compared to its intensity when 0 V is applied. In our lab, we extended this work and made an absorptive Fresnel lens with a variable focal length.⁹⁴ We patterned concentric circles of PEDOT:PSS using electrochemical overoxidation,⁹⁵ as shown in Figure II-3. When the PEDOT is oxidized, the entire lens is transparent and focuses at infinity, but when the PEDOT is reduced, there is a

pattern of absorbing concentric circles that diffract the incident light and focus it at a distance of 33 cm. At an applied voltage of +1 V, approximately 0.5% of the incident light is diffracted to the focus at 33 cm. Although 0.5% is a low diffraction efficiency, the intensity at the focus for +1 V applied is 8 times the intensity at the focus for -1 V, as shown in Figure II-3.

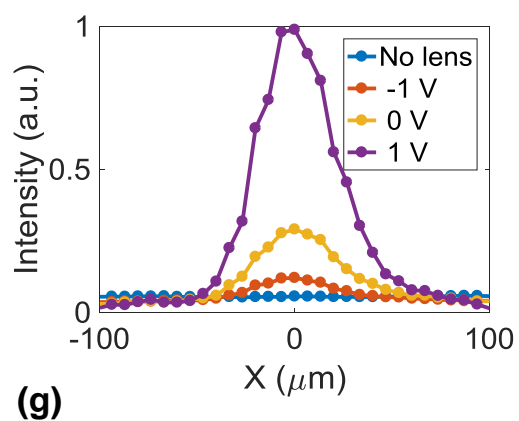
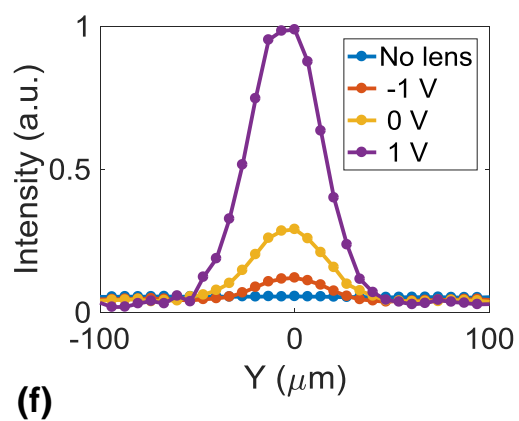
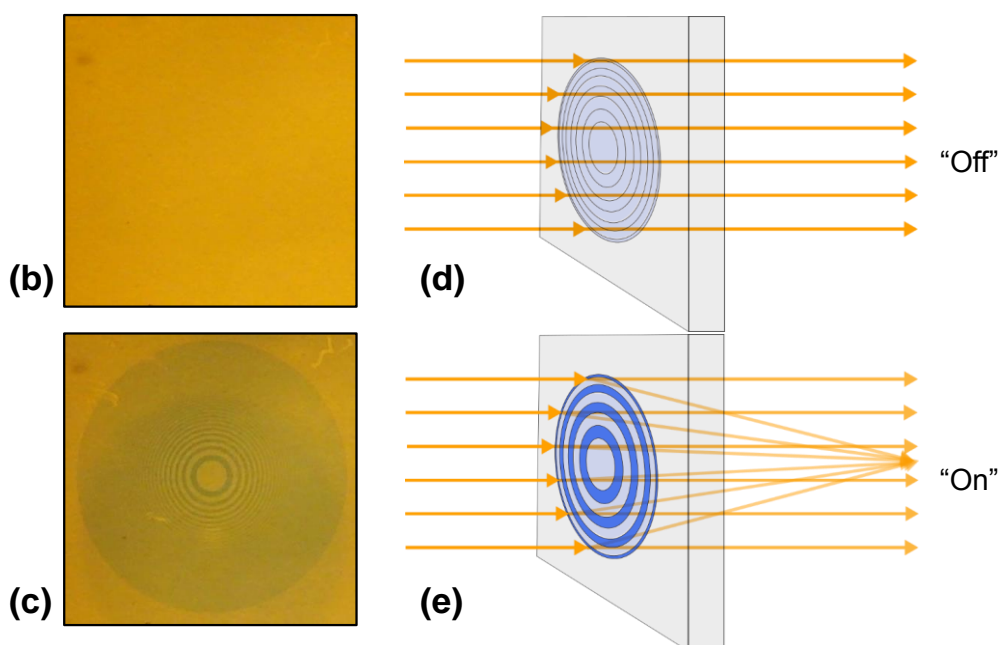
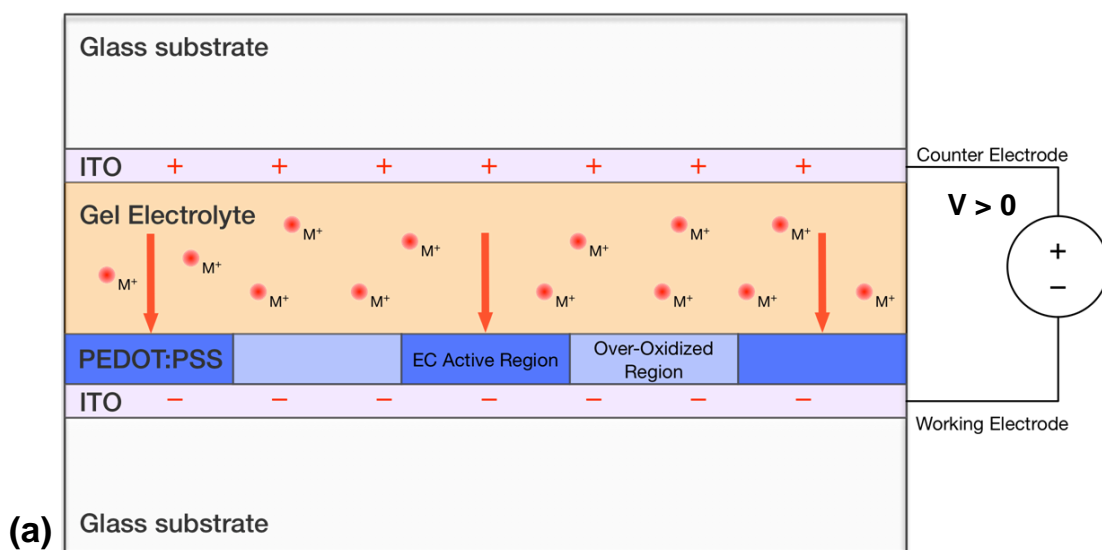


Figure II-3. Device structure and operation of an electrochromic Fresnel lens. Panel (a) shows a cross-section of the device structure. Panels (b) and (c) show photographs of the Fresnel lens when it is off (b) and on (c), demonstrating the change in PEDOT:PSS absorption. Panels (d) and (e) describe the path of light rays passing through the lens in the off (d) and on (e) states. Panels (f) and (g) show the cross-sectional intensity profiles of the focal spot of the lens.

B. Moving front experiments for estimating ionic mobility

While the examples above show that electrochromism in PEDOT:PSS can be directly useful in applications such as displays and electrically switchable lenses, electrochromism can also be used for more basic research purposes, such as inferring the concentration of charge carriers in PEDOT:PSS. Figure II-4 shows that the absorption spectra vary continuously as a function of the voltage on the counter electrode. This continuous variation occurs because not all of the PEDOT is oxidized at the same voltage; therefore, the prominence of the absorption peak near 600 nm represents the ratio of neutral to oxidized PEDOT molecules. As the counter electrode is made more positive, more PEDOT molecules are reduced to the neutral form, so more HOMO-LUMO absorption occurs, and the height of the absorption peak near 600 nm increases. Because neutral PEDOT molecules have no charge carriers and oxidized PEDOT molecules have holes (see chapter I), strong absorption near 600 nm indicates a low concentration of holes in the PEDOT and consequently, a low conductivity.

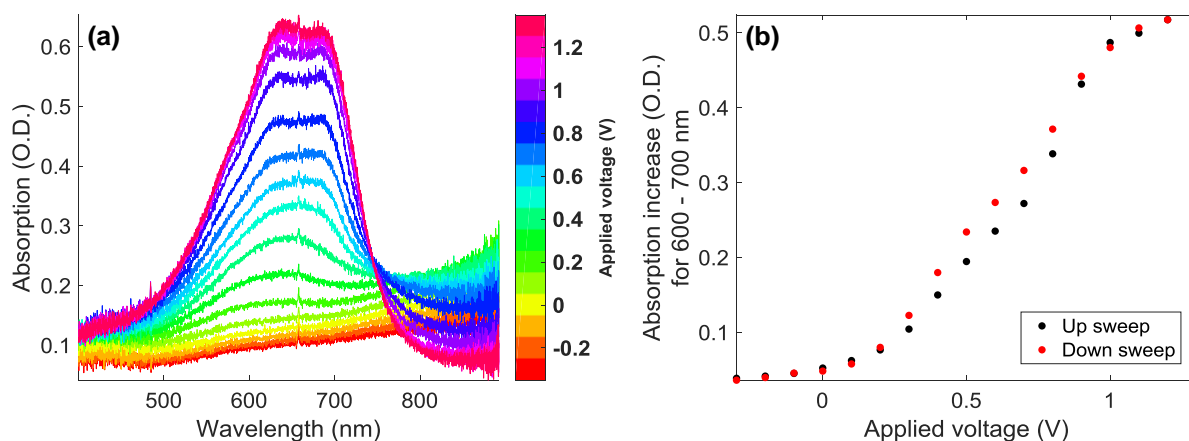


Figure II-4. PEDOT:PSS absorption spectra as a function of voltage applied at the counter electrode. Panel (b) shows the change in optical density as a function of the voltage applied at the counter electrode for wavelengths corresponding to HOMO-LUMO absorption.

Several authors have used this inverse relationship between visible absorption and carrier density to infer the rate of ion transport as the ions dope (or de-dope) films of various organic semiconductors.⁹⁶⁻⁹⁹ For instance, E. Stavriniidou, et al. designed an experiment with 1-dimensional ion transport through a PEDOT:PSS film, as shown in Figure II-5.⁹⁹ The PEDOT:PSS started in its conductive state with 0 V applied at the counter electrode. When a positive voltage was applied, cations began to drift into the PEDOT:PSS, first de-doping the region near the electrolyte and causing its optical absorption near 600 nm to increase. As time progressed, the optically absorptive region extended farther away from the electrolyte as the ions moved farther into the PEDOT:PSS film. By recording the speed of this “de-doping front” as it extended into the PEDOT:PSS film, E. Stavriniidou et al. obtained a direct measurement of the rate of ion transport through the film. They concluded that the mobility of small metal cations in hydrated PEDOT:PSS is $\sim 10^{-3} \text{ cm}^2 \text{ V}^{-1} \text{ s}^{-1}$, which is the same as the mobility of these ions in water. Additionally, they found that cation mobility dropped by about an order of magnitude when a cross-linker was added to the PEDOT:PSS film. Because adding a cross-linker greatly

enhances PEDOT:PSS film stability in water,¹⁰⁰ the decreased mobility with added cross-linker suggests a steep tradeoff between device speed and stability.

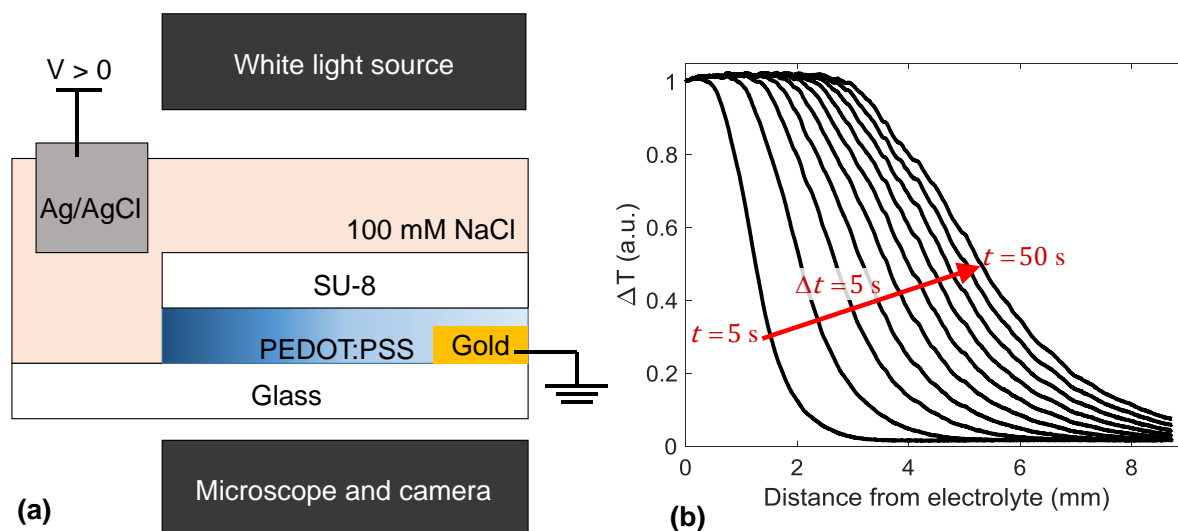


Figure II-5. Device structure and optical measurements of the de-doping front experiment. Panel (a) shows the device structure, and panel (b) shows the position and cross-sectional shape of the de-doping front in terms of the change in the PEDOT:PSS transmittance. In (b), each curve is the profile of the de-doping front at a different time, starting 5 s after the voltage step on the counter electrode and then in 5 s increments after that. Data in (b) come from E. Stavrinidou et al.⁹⁹

In our work, we have executed experiments similar to E. Stavrinidou, et al.'s work, but we included voltage-measurement probes in contact with the PEDOT:PSS film, as shown in Figure II-6a,b. This allowed us to directly measure the amount of voltage dropped at the electrolyte-PEDOT:PSS interface, in the PEDOT:PSS film, and at the PEDOT:PSS-electrode interface. We used ~ 120 nm thick polymer film composed of PEDOT:PSS crosslinked with 3-glycidoxypropyltrimethoxysilane (GOPS). The contact to the PEDOT:PSS was a gold electrode with a chromium adhesion layer, and we used an SU-8 layer as an ion barrier on top of the PEDOT:PSS. Our electrolyte was 100 mM NaCl in water, and the counter electrode was a 2.5 mm × 2.5 mm silver/silver-chloride pellet. The results of our measurements are shown in Figure II-6c-f, and they verify two important points about ion transport in PEDOT:PSS. First, as predicted by the simple model described by E. Stavrinidou, the position of the de-doping front

has a square-root dependence on time. According to that model, the position of the de-doping front follows the relationship $x = \sqrt{2\mu V t}$, where x is the front position, μ is the ion mobility, V is the applied voltage*, and t is the time after the voltage step. Although our data fit reasonably well to the square-root dependence, we extract an ion mobility of $\mu = (4 \pm 2) \times 10^{-3} \text{ cm}^2\text{V}^{-1}\text{s}^{-1}$,† which is ~ 20 times larger than what E. Stavrinidou reported for the K^+ mobility in GOPS-crosslinked PEDOT:PSS. This discrepancy appears partly because E. Stavrinidou assumed that there was no voltage drop at the electrolyte-PEDOT:PSS interface; whereas we account for a 0.7 V drop, according to our voltage measurements. Additionally, Stavrinidou's PEDOT:PSS film was substantially longer than the one we used (32 mm versus $220\mu\text{m}$). Because we used a shorter film, some of the ions in our experiment reached the gold electrode before the optical measurements used for Figure II-6f could be completed. This causes the voltage dropped across the PEDOT:PSS film to change during the experiment – a complication Stavrinidou did not encounter. The second detail about ion transport that our experiment verified is that most of the 1 V applied at the counter electrode drops at the electrolyte-PEDOT:PSS interface and at the PEDOT:PSS-gold interface. The voltage drop at the electrolyte-PEDOT:PSS interface occurs because the electrolyte is a barrier to electronic charge, and the voltage drop at the gold interface occurs because the gold is a barrier to ionic charge. Charge can build up at both of these barriers and create space-charge regions with large electric fields. One unexplained feature we see in our measurements is the drift of the measured voltages more than 150 seconds after the applied voltage step (Figure II-6c). We are unsure what causes

* We use $V = 0.3 \text{ V}$, the voltage across the polymer film rather than the applied voltage here. E. Stavrinidou et al. used the applied voltage, assuming that no voltage was dropped in the electrolyte or at the electrolyte-film interface.

† The uncertainty on extracted mobility is based on a 95% confidence interval of the extracted slope from Figure II-6f.

this voltage drift, but it could be a Faradaic current due to chromium oxidation at the gold electrode.¹⁰¹

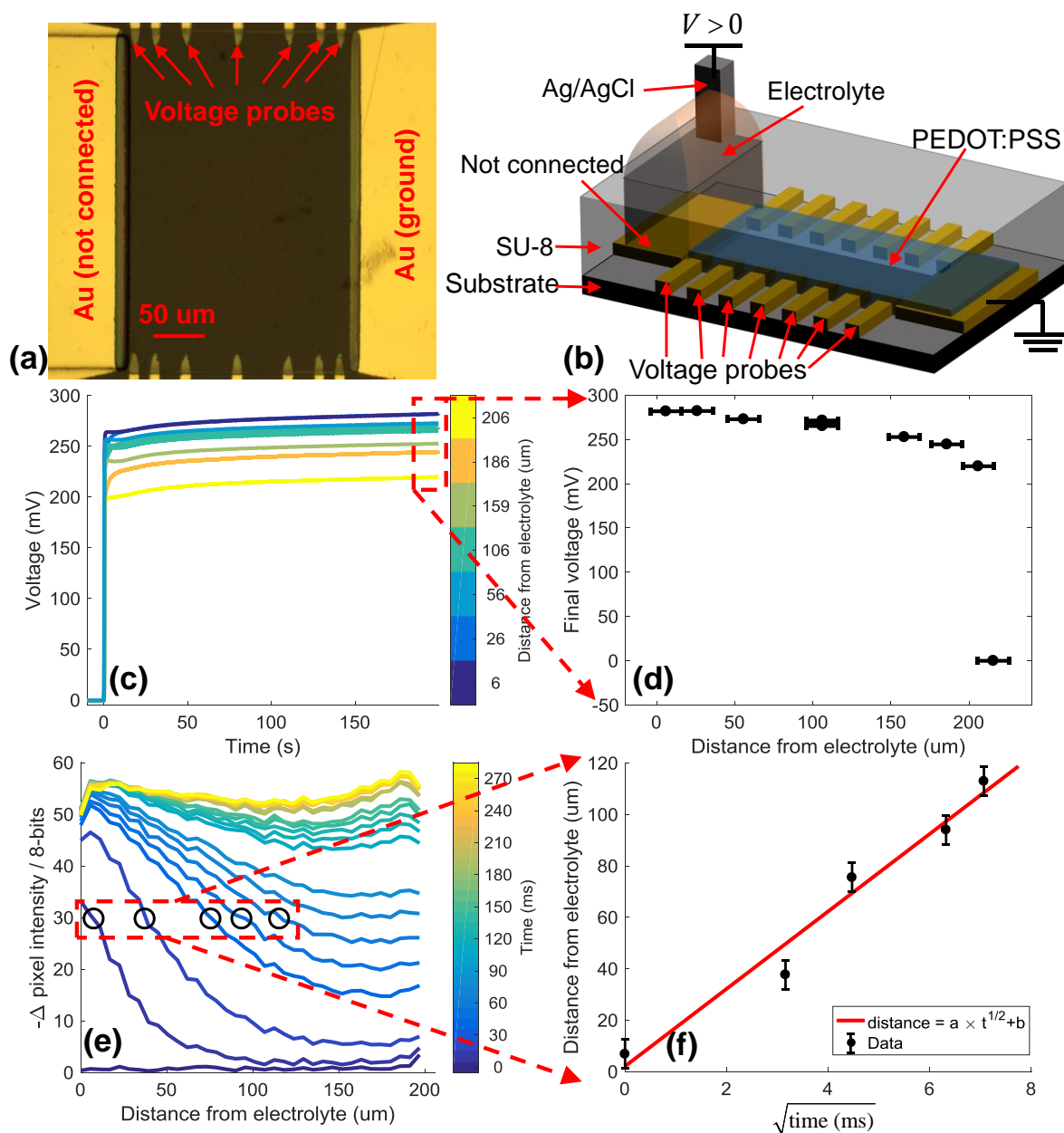


Figure II-6. Device structure and results of de-doping front measurement. Panel (a) is a micrograph of the device before adding the electrolyte. Panel (b) is a diagram describing the device structure. Panel (c) shows the measured voltage at each probe as a function of time. Panel (d) shows the final voltage measured at each probe 200 s after the voltage is stepped at the counter electrode. Panel (e) shows the de-doping front in terms of the measured intensity at each pixel row of the camera. Separate curves were measured at different times after the step at the counter voltage, as indicated in the colorbar. Panel (f) shows the position of the de-doping front as a function of time. The distances plotted in (f) were extracted from panel (e) as the distance at which the change in intensity was -30 counts on the 8-bit detector. The points plotted in panel (f) are circled in panel (e). The vertical error bars in (f) are equal to the pixel pitch in the recorded image of the device. The horizontal error bars in (d) are equal to the width of the voltage probes in the device.

Altogether, the measurements described above provide insight about ion transport in PEDOT:PSS and motivate optical techniques to study the operation of OECTs. To this end, we have made simultaneous optical and electrical measurements of PEDOT:PSS-based OECTs, as discussed below.

C. Optical measurements revealing non-uniform hole mobility in OECTs

Theoretical predictions and experimental results show that the carrier mobility in conjugated polymers depends on carrier concentration. However, existing models for OECTs assume uniform carrier mobility along the transistor channel despite variations in carrier concentration. In this section, we develop a model incorporating non-uniform mobility to describe the steady-state behavior of OECTs. We tested this model using in situ optical measurements of an OECT channel to decouple the mobility and carrier concentration contributions to channel conductivity. We found that unlike existing models, the non-uniform mobility model agrees with these measurements. Furthermore, we found that the model matches current-voltage data over a wide range of device geometries and two different device architectures. Finally, we show that we can obtain a 120 % improvement of transconductance by operating a sensor according to device parameters given by the non-uniform mobility model rather than those extracted from an existing model that assumes a uniform mobility. Ultimately, the model in this section allows more accurate measurement of material properties via transistor characterization. This will enable better-informed material optimization, development of more accurate transient models for OECTs, and more effective use of OECTs made from existing materials.

D. Development of a non-uniform mobility model

As discussed in chapter I, a basic understanding of OECT operating principles has allowed OECTs to be successfully used in numerous sensing^{23,27,54,57,60,63,65–67,69,84,102–104} and

logic applications;^{33–35} however, understanding of OECT device physics and material science is still limited. Existing models for OECTs either fail to provide quantitative predictions for device behavior²⁴ or fail to account for well-known material properties of conjugated polymers.²⁶ For instance, Bernardis and Malliaras provided an early model for OECT behavior.²⁶ This model adapts the standard treatment of long-channel depletion-mode inorganic field-effect transistors¹³ by incorporating an ionic coupling between the gate and channel. While this model has been used to explain OECT behavior in numerous applications,^{27,53,62,64,105} its accuracy is limited because it treats the OECT channel as if it were a well-ordered, crystalline semiconductor. Therefore, this work – and much of the OECT literature^{26,30,53,104,106–108} – assumes that mobility is a constant and independent of carrier concentration. Numerous theoretical^{109–115} and experimental^{109,115–118} studies have shown that this assumption is false. These reports show that carrier mobility depends on carrier concentration and have found that this dependence is due to the exponentially distributed density of states (DOS) near the band edges in disordered organic semiconductors. As the “trap states” near the band edge are filled, carriers begin to occupy states at higher energies, where the DOS is much larger. Because the DOS is larger, more sites are available for carriers to hop into. Consequently, carriers deeper into the DOS have a larger mobility than if they were near the band edge. According to this explanation, the dependence of mobility on carrier density should follow the relationship

$$\mu(p) = \mu_0 \times \left[\frac{p}{p_0} \right]^{\frac{E_0}{kT} - 1} \quad (\text{II.1})$$

where μ is the hole mobility, p is the hole concentration, E_0 is the disorder parameter describing the energetic width of the tail of the density of states, k is Boltzmann’s constant, T is temperature; μ_0 is a mobility prefactor that is independent of carrier concentration but might depend on other factors such as temperature; and p_0 is the zero-field hole concentration.^{109,119}

Researchers have observed the dependence of mobility on carrier concentration in OECTs with various combinations of semiconductor and electrolyte materials.^{120–122} However, none of these authors integrate their empirical findings about carrier mobility into a closed-form expression for OECT channel current as a function of gate and drain voltage.

Other authors, in particular, Berggren et al., do include a nonlinear conductivity versus hole concentration relationship in their current-voltage equations for OECTs. By assuming a conductivity of the form $\sigma = \sigma_0 \times [\varepsilon + (\frac{p}{p_0})^\gamma]$, where ε and γ are empirically determined constants, these authors have implicitly assumed a mobility with the form given by

(II.1). Berggren et al. show that their model predicts a voltage drop along the OECT channel that steepens as it nears the negatively biased drain electrode.²⁴ Their spatially-resolved voltage measurements and their optical measurements qualitatively agree with their predictions. However, their model contains too many free variables to quantitatively compare it to measurements or to extract meaningful device parameters.^{24,26} Furthermore, for a fixed gate voltage, their model fails to predict a decrease in the average carrier density as the drain voltage is made more negative. Later, the Berggren group developed a model for electrolyte-gated field-effect transistors that addressed these shortcomings, but they did not compare it to spatially resolved measurements along the transistor channel.^{123,124} Despite these weaknesses, their models demonstrate the importance of non-uniform hole mobility along the OECT channel.

In the present section, we follow the work done by the Berggren and Malliaras groups and introduce a non-uniform mobility into the Bernards model.²⁶ The resulting model is simpler than the Berggren models and fits experimental current-voltage data better than the Bernards model. Furthermore, unlike the Bernards model, the non-uniform mobility model also explains spatially-resolved optical data.

The Bernards model starts with the assumption that each injected cation removes one hole from the PEDOT:PSS. Thus the hole concentration in the channel can be found as shown in Equation (II.3)

$$dQ(x) = cWdx[V_G - V(x)] \quad (\text{II.2})$$

$$p(x) = p_0 \left[1 - \frac{dQ(x)}{p_0 q W h dx} \right] = p_0 \left[1 - \frac{V_G - V(x)}{V_P} \right], \quad (\text{II.3})$$

where dQ/dx is the cationic charge density injected into the transistor channel, x is the distance along the OECT channel away from the source electrode, c is the ionic capacitance per unit area, W is the channel width, h is the channel thickness, V_G is the gate voltage, $V(x)$ is the voltage in the channel at position x , p_0 is the hole density before any cations are injected, and $V_P \equiv qp_0h/c$ is the channel pinch-off voltage. The ionic capacitance, c , is given by the capacitance of two capacitors in series. One of these capacitors is at the gate/electrolyte interface, and the other is the capacitance of the OECT channel.^{27,28,125} Inserting Equation (II.2) and (II.3) into the differential form of Ohm's law, $J = \sigma \frac{dV}{dx}$, yields

$$J = q\mu_0 p_0 \left[1 - \frac{V_G - V(x)}{V_P} \right]^{\frac{E_0}{kT}} \frac{dV}{dx} \quad (\text{II.4})$$

where J is the current density through the channel, and σ is channel conductivity. Equation (II.4) is identical to Equation (5) of the Bernards model except for the E_0/kT power that comes from Equation (II.1).

Because the steady-state current density throughout the OECT channel is constant, the integration to obtain the current-voltage relationship is straightforward.

$$\int_{x=0}^L J dx = \int_{V=0}^{V_D} q\mu_0 p_0 \left[1 - \frac{V_G - V(x)}{V_P} \right]^{\frac{E_0}{kT}} dV \quad (\text{II.5})$$

$$I = \frac{GV_P}{\frac{E_0}{kT}+1} \times \left[\left[1 - \frac{V_G - V_D}{V_P} \right]^{\frac{E_0}{kT}+1} - \left[1 - \frac{V_G}{V_P} \right]^{\frac{E_0}{kT}+1} \right], V_D > V_{D,sat} \quad (\text{II.6})$$

or, in the saturation regime,

$$I = -\frac{GV_P}{\frac{E_0}{kT}+1} \times \left[1 - \frac{V_G}{V_P} \right]^{\frac{E_0}{kT}+1}, V_D < V_{D,sat} \quad (\text{II.7})$$

where $G \equiv \frac{q\mu_0 p_0 W h}{L}$ is the channel conductance under zero applied field, and V_D is the drain

voltage. When $V_D < V_{D,sat} \equiv V_G - V_P$, the proposed model assumes the typical pinch-off behavior exhibited by long-channel transistors,¹³ as indicated by Equation (II.7). After obtaining the I - V relationship given by Equation (II.6) and (II.7), we integrate Equation (II.5) from the source to an arbitrary distance x . This yields

$$Ix = \frac{GLV_P}{\frac{E_0}{kT}+1} \times \left[\left[1 - \frac{V_G - V(x)}{V_P} \right]^{\frac{E_0}{kT}+1} - \left[1 - \frac{V_G}{V_P} \right]^{\frac{E_0}{kT}+1} \right] \quad (\text{II.8})$$

Using Equation (II.6) for the linear regime or Equation (II.7) for the saturation regime, this

expression can be solved for $1 - \frac{V_G - V(x)}{V_P}$, which can be substituted into Equation (II.3) to find

the hole concentration as a function of position along the channel,

$$\frac{p(x)}{p_0} = \left[\frac{Ix \left[\frac{E_0}{kT} + 1 \right]}{GLV_P} + \left[1 - \frac{V_G}{V_P} \right]^{\frac{E_0}{kT}+1} \right]^{\frac{kT}{E_0 + kT}}, \quad (\text{II.9})$$

which is valid in both the linear and saturation regimes, as long as the appropriate expression is used for I .

1. Optical evidence for non-uniform hole mobility

We tested the theory presented in section C-D by fabricating OEETs with the lateral geometry shown in Figure II-7 and making current-voltage measurements simultaneously with optical absorption measurements. These OEETs used a transparent gel as the electrolyte and gold as the gate electrode. For the current-voltage measurements, we used a two-channel source meter

unit, and for the optical measurements, we used the setup shown in Figure II-7d. More experimental details are provided in Appendix I.

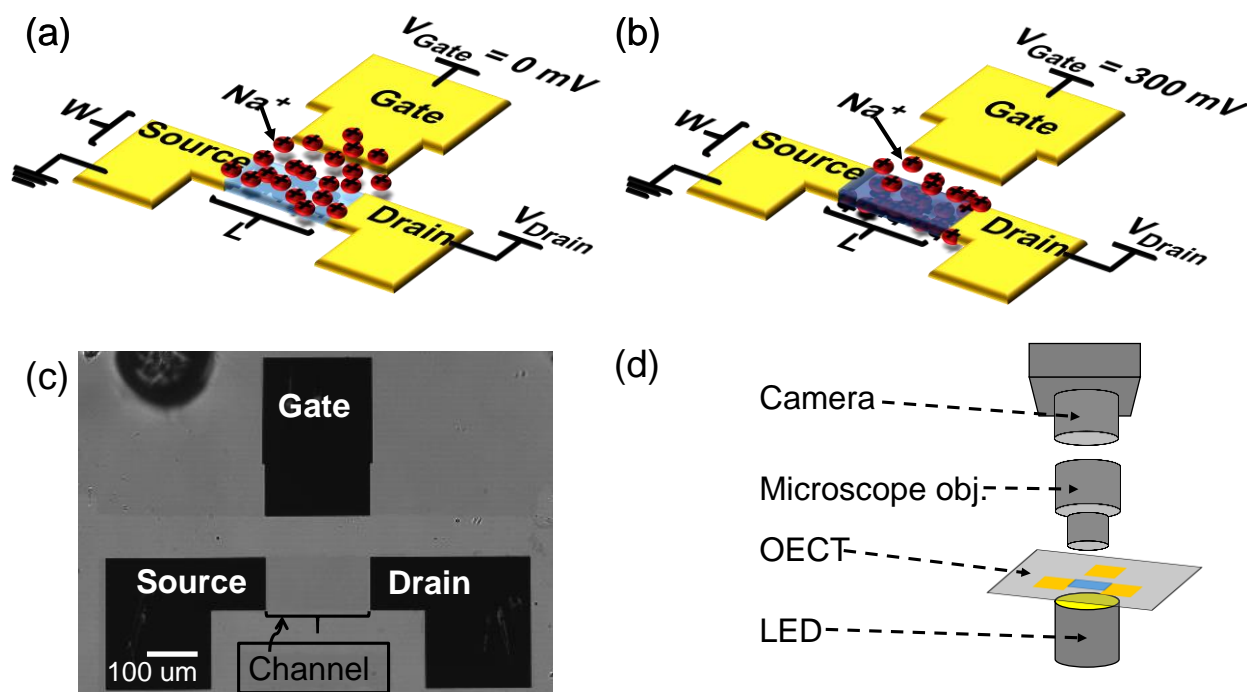


Figure II-7. Diagrams showing a lateral OEET in the high conductivity a) and low conductivity b) states. c) Micrograph of a lateral OEET used for this study. d) Schematic of the setup for optical measurements.

As shown in Figure II-8a,b, the current-voltage data quantitatively fit both the Bernards model and the proposed non-uniform mobility model.* Both models predict similar zero-field conductance of $\sim 0.65 - 0.75$ mS, but the non-uniform mobility model predicts an onset of saturation at 720 mV – about 40% higher than the value predicted by the Bernards model. In Figure II-8c,d, we show the hole concentration predicted by the non-uniform mobility model as well as the response from our optical measurements. The optical data agree qualitatively with the proposed model; however, without a priori knowledge of how hole concentration and optical response are related, we cannot make a quantitative comparison. To examine this relationship,

* Although the Bernards model fits nicely to the data for $V_D > V_{D,sat}$, it does not fit as well in the saturation regime. Using an F-Test to compare the quality of fits for the Bernards model and the non-uniform mobility model, we find that the non-uniform mobility model is a better fit with a p-value of $p < 10^{-5}$ for the data shown in Figure II-10.

we plot optical absorption at every V_D, V_G combination as a function of the predicted hole concentration parameterized by the position along the OECT channel. As shown in Figure II-9a, the Bernards model does not yield the expected one-to-one relationship between the predicted hole density and the optical response. However, if we take into account non-uniform mobility, all of the curves collapse onto a universal curve that holds for every combination of V_D and V_G (Figure II-9b).

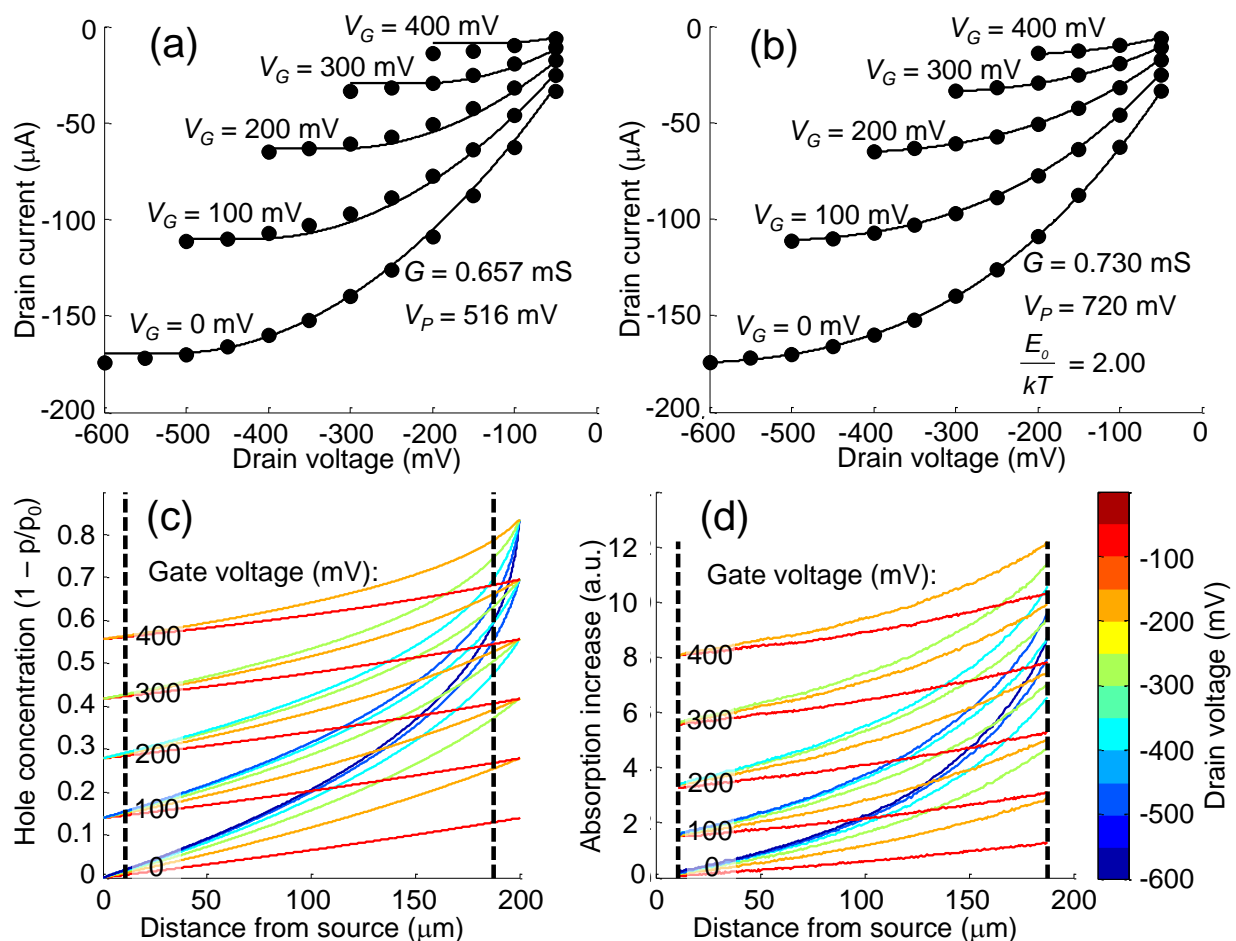


Figure II-8. Output curves and hole concentration for a lateral OEET. Panels (a) and (b) are the output curves of the OEET where dots are data and solid lines are the fit to the model. In (a), the Bernards model is used for the fit. In (b), the non-uniform mobility model is used. The free parameters used for the model fits are inset in (a) and (b). Panel (c) shows the hole concentration along the OEET channel predicted by the non-uniform hole mobility model with $E_0/kT = 2$. (d) Measured optical absorption increase along the OEET channel. In (c) and (d), the drain voltage of each curve is encoded by the color bar on the right side of (d), and the gate voltage is labeled inside the left edge of (c) and (d). Optical measurements could not be taken outside of the vertical dashed lines shown in (c) and (d) because of shading and interference ringing at the electrode edges.

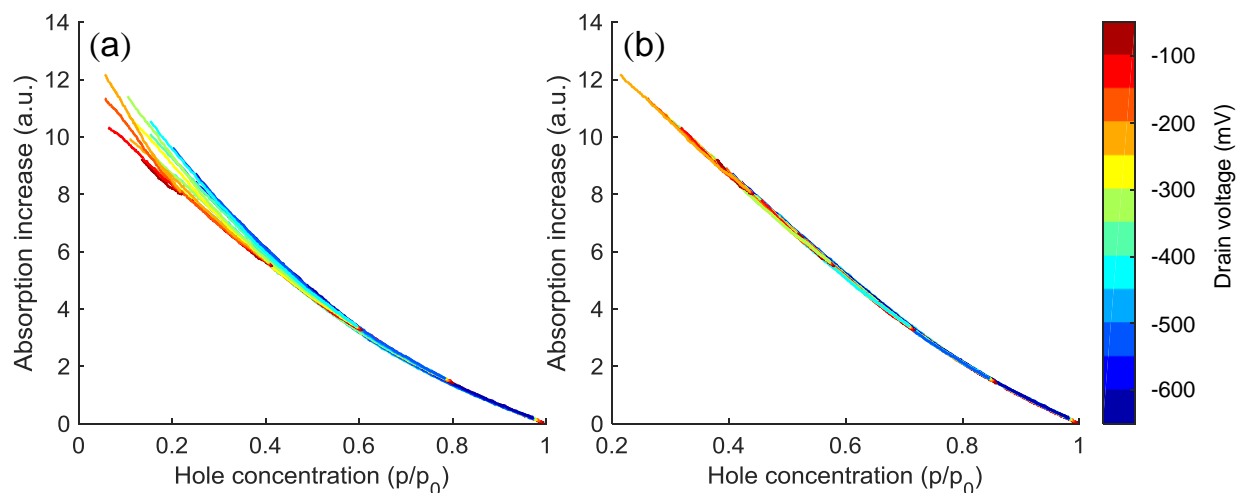


Figure II-9. The measured optical absorption increase plotted as a function of the hole concentration predicted by the Bernards model (a) and the non-uniform mobility model with $E_0/kT = 2$ (b). We note that in (a) the curves spread out monotonically with drain voltage, indicating a systematic error in the model.

The lack of a universal curve in Figure II-9a demonstrates that the Bernards model does not contain all of the relevant physics. As explained above, removing holes from the system reduces the number of polarons. Because a decrease in the hole concentration should increase the visible absorption of PEDOT:PSS, there must be a one-to-one (but not necessarily linear) relationship between hole concentration and absorption, regardless of the drain and gate voltages. This is not experimentally observed unless energetic disorder in the density of states is accounted for by including a non-uniform mobility in the proposed model. Furthermore, we found that other modifications to the Bernards model, such as taking into account channel length modulation, contact resistance, or a voltage-dependent ionic capacitance all failed to generate a universal curve (see Appendix I section B). However, a modification that assumes an exponential dependence of mobility (rather than the power law dependence described in section C-D) on hole concentration does yield a universal curve (see Appendix I section B). This supports the argument that the correct modification to the Bernards model involves a hole-concentration-dependent mobility. Although the exponential dependence gives results

comparable to the power law dependence, we prefer the power law model because it is based on experimentally and theoretically justified physics. Moreover, the extracted disorder parameter of $E_0 = 2kT$ is consistent with typical experimental results for conjugated polymers.¹²⁶

Another element of interest is the shape of the optical response versus hole concentration relationship shown in Figure II-9b. If the change in the optical absorption does not depend on the energy of the hole removed, there would be a linear relationship between visible absorption and hole concentration. Figure II-9b and Figure VII-15 (in Appendix I), show a nearly linear relationship, as one would expect if the number of visible photons absorbed was directly proportional to the density of neutral PEDOT molecules. However, this linear relationship breaks down at high hole concentrations. This could be due to the fact that at these carrier concentrations, the presence of bipolarons in addition to polarons and neutral PEDOT molecules complicates the absorption properties of the material. Although we do not have a detailed explanation for this departure from linearity, we note that similar behavior in the optical response at high conductivities has been reported by others.¹²⁷⁻¹³⁰

2. Geometrical scaling of transistor parameters

To further test the validity of the non-uniform mobility model, we checked to see if it holds for devices with different architecture and geometries. Not only did we test devices with the lateral geometry shown in Figure II-7, but we also tested devices with a vertical geometry where the Ag/AgCl gate electrode is suspended in a liquid electrolyte (100 mM NaCl), as described in Figure I-2. Using the vertical geometry with a liquid electrolyte and a Ag/AgCl gate instead of gold leads to higher ionic mobility, the presence of mobile anions, and a gate electrode with greatly reduced polarizability. Despite these effects and others, we did not expect the changes to our experimental system to invalidate the assumptions of our model. Therefore, using

both sets of experimental conditions is a stringent test of our model. Furthermore, we not only tested a different architecture, but we also measured devices with six different channel width-to-length ratios ranging from 0.14 to 5.5. The I - V data for the devices with the smallest and largest width to length ratios are shown in Figure II-10. The non-uniform mobility model yields an excellent fit to the I - V data even for devices with width-to-length ratios differing by more than an order of magnitude. However, the Bernards model fails to accurately describe the saturation behavior of these devices. This distinction between the two models is most apparent at higher gate voltage values.

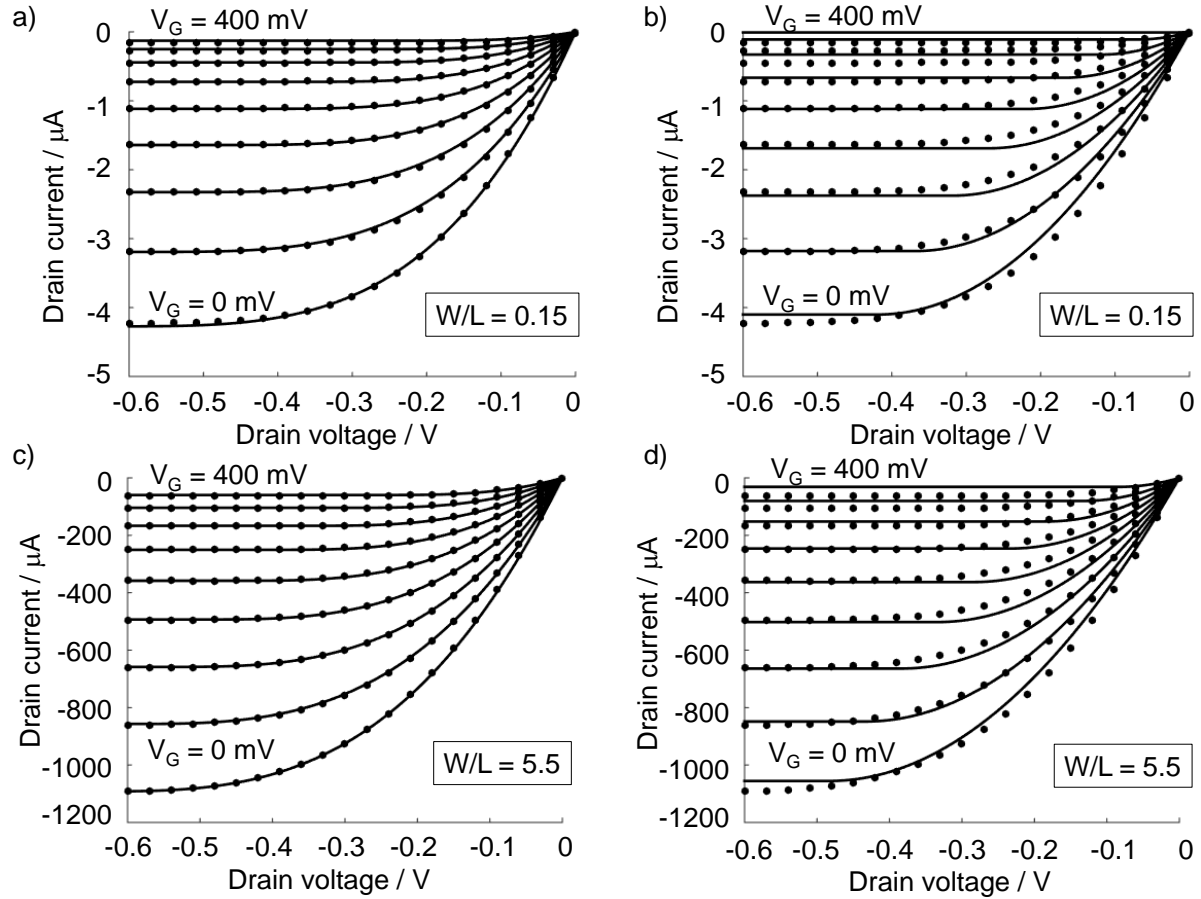


Figure II-10. Comparison of experimental data (circles) to model fits (solid lines) for devices with the vertical OECT geometry. Panels (a) and (b) are the data and fits for a device with width/length = $33.2 \mu\text{m}/238 \mu\text{m}$. Panels (c) and (d) are the data and fits for a device with width/length = $250 \mu\text{m}/45.6 \mu\text{m}$. The nonuniform mobility model fits are in panels (a) and (c), while the Bernardis–Malliaras model fits are shown in panels (b) and (d). Each curve is for a different gate voltage starting from $V_G = 0 \text{ mV}$ and increasing in 50 mV steps up to 400 mV , as indicated by the labels on the top and bottom curves.

Although Figure II-10 clearly shows that the non-uniform mobility model fits device data for a wide range of geometries, the robustness of this model to geometry variations cannot be confirmed without analyzing the trends in the fit parameters. In Figure II-11, each fit parameter is plotted as a function of the channel width to length ratio. Figure II-11a shows that the extracted zero-field channel conductance, G , scales linearly with W/L . When the linear fit to these data is forced to cross the origin, the degree-of-freedom-adjusted coefficient of correlation is $r^2 = 0.99$. The slope of this linear fit is 0.88 mS , and the dry-film thickness of the channel is \sim

100 nm (the hydrated film is somewhat thicker). Thus we obtain a conductivity of approximately 90 S/cm, which is similar to previous measurements for the same PEDOT:PSS formulation.⁸⁴ In contrast to the linear relationship between channel conductance and W/L , neither the pinch-off voltage, nor the disorder parameter has a strong dependence on W/L , as shown in Figure II-11b,c. These results demonstrate that the proposed model not only fits the data for a wide range of geometries, but it also extracts reasonable device and material parameters over this range. Furthermore, the geometry scaling of these parameters rules out several other possible explanations for the departure of device behavior from the Bernards model. For instance, if parasitic series resistance were responsible for the observed behavior, the departure from the Bernards model would be greatest for devices with large W/L , which is clearly not the case. Similarly, channel length modulation would affect short-channel devices the most, but, as shown in Figure II-11d, disagreement with the Bernards model tends to increase slowly with channel length. This tendency is not predicted by the proposed model, and we cannot offer a theoretical explanation for this behavior. However, we note that even for an $\sim 400\%$ increase in channel length, the extracted disorder parameter varies by less than 40%. Moreover, even if the trend is extrapolated to $L = 0$, the disorder parameter would still be 90% greater than what would be extracted if the Bernards model were valid.

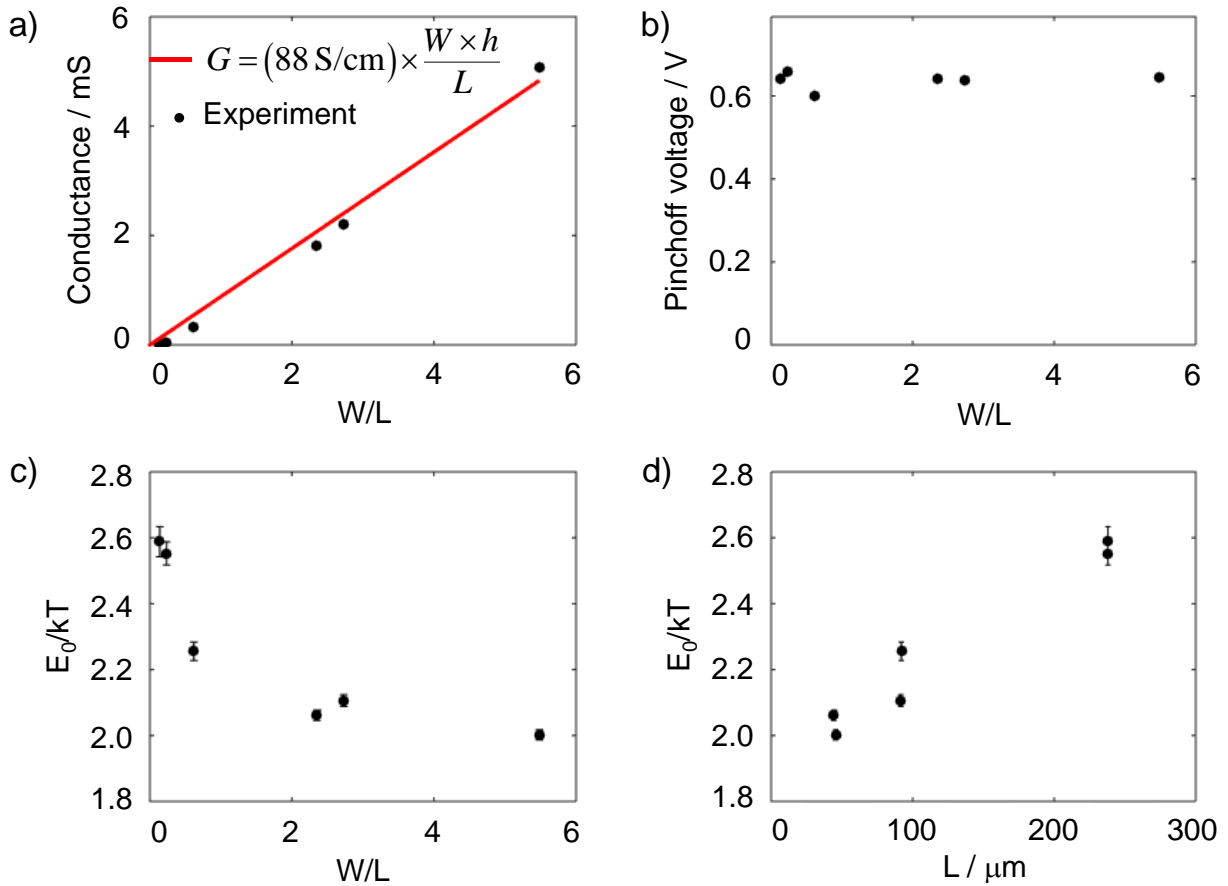


Figure II-11. Geometry scaling of fit parameters according to the nonuniform mobility model. Error bars are the 95% confidence intervals of the extracted parameters from the least squares fitting. The error bars are too small to be visible in panels (a) and (b).

3. Transconductance optimization

In section D-1, we demonstrated that the pinch-off voltage provided by the non-uniform mobility model is substantially larger than that provided by the Bernards model. This discrepancy has significant implications for the use of OECTs as biosensors. It can be shown (see Appendix I equation (VII.13)) that the transconductance, $g_m \equiv \left(\frac{\partial I_D}{\partial V_G} \right)_{V_D}$, increases monotonically as the drain voltage is made more negative, up to the saturation voltage. Because many OECT-based sensing platforms use a fixed drain voltage,^{23,54,67,69,103,131} the signal to noise

ratio can be optimized by tuning the drain voltage. Setting the drain voltage at $V_D = V_{D,sat}$ maximizes the transconductance while minimizing bias stress on the device and damage to any biological systems being measured.¹³² As shown above, the Bernards model significantly underestimates the pinch-off voltage. Because $V_{D,sat} = V_G - V_P$, an underestimate of V_P translates to an underestimate of $|V_{D,sat}|$ (for $V_P > V_G$) and leads to suboptimal transconductance. Figure II-12a demonstrates this effect for a device operated at $V_G = 225$ mV. If the data for this device are fit using the Bernards model, the extracted pinch-off voltage is $V_P = 425$ mV; whereas, the non-uniform mobility model yields $V_P = 593$ mV. Therefore, at $V_G = 225$ mV, the saturation voltage is $V_{D,sat}^{Bernards} = -200$ mV, according to the Bernards model, and $V_{D,sat} = -373$ mV, according to the non-uniform mobility model. One can define % improvement of the transconductance as

$$\%Improvement = \frac{g(V_{D,sat}) - g(V_{D,sat}^{Bernards})}{g(V_{D,sat}^{Bernards})} \times 100\%, \quad (II.10)$$

where $V_{D,sat}$ is calculated with V_P extracted from the fit to the non-uniform mobility model and $V_{D,sat}^{Bernards}$ is calculated with V_P extracted from the fit to the Bernards model. With this definition, we find that operating the device at the saturation voltage given by the non-uniform mobility model results in a 19% improvement in transconductance over what would be obtained if the device were operated at the saturation voltage given by the Bernards model. As shown in Figure II-12b, this effect becomes more pronounced at increased gate voltage, providing a 127% improvement when the gate voltage is 375 mV, the highest gate voltage for which we could use the Bernards model. Because transconductance increases monotonically with drain voltage and

because the Bernards model consistently underestimates the saturation voltage, using the non-uniform mobility model will consistently improve transconductance.

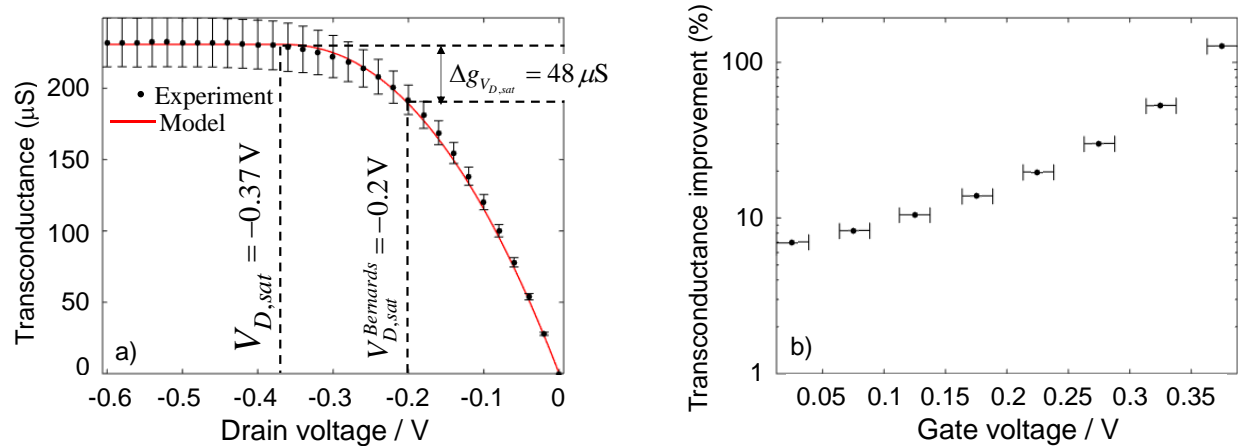


Figure II-12. Transconductance obtained by numerical differentiation of the transfer curves for each drain voltage. The transfer curves were obtained from measurements of a device with the vertical geometry and width/length = $50 \mu\text{m}/50 \mu\text{m}$. In panel (a), the transconductance is plotted as a function of drain voltage for $V_G = 225 \text{ mV}$. The solid line shows the expected transconductance calculated according to the non-uniform mobility model. The dashed lines show the saturation voltage and corresponding transconductance for the Bernards model ($V_{D,sat}^{\text{Bernards}} = -0.2 \text{ V}$) and the non-uniform mobility model ($V_{D,sat} = -0.37 \text{ V}$). In panel (b) the improvement in transconductance obtained by using the non-uniform mobility model to extract the saturation voltage rather than the Bernards model is plotted. The error bars are calculated by propagating the uncertainty in gate voltage due to the finite step size between measurements. We assume that this uncertainty is \pm one-half of the 50 mV step size between gate voltage measurements.

E. Conclusion

In conclusion, we have shown several uses for electrochromism in PEDOT:PSS. For instance, we fabricated and characterized electrically-switchable Fresnel lenses, and we used simultaneous absorption and voltage measurements to understand the ion mobility in PEDOT:PSS films. Finally, we used electrochromism in PEDOT:PSS to show that the assumption of uniform mobility in an OECT channel is incorrect. We developed a non-uniform mobility model and experimentally showed its validity for a wide range of device geometries and two substantially different device architectures. This model provides more accurate information

about the properties of the active material in an OECT, such as the conductivity, zero-field mobility, disorder parameter, and the ratio of the zero-field hole concentration to the ionic capacitance (which can be obtained from the pinch-off voltage²⁸). Knowledge of these material parameters will enhance understanding of charge transport in conjugated polymers and will enable more effective material screening for the development of new polymers to be used in OECTs. Additionally, the improved knowledge of material properties allows more effective use of OECTs in biosensing applications. In particular, using the non-uniform mobility model instead of the Bernards model to extract the saturation voltage can lead to more than a 120% improvement in transconductance. Furthermore, we expect that the improved understanding of mobility in OECTs provided by the non-uniform mobility model will be useful in developing a more accurate transient model of OECT behavior. Such a model could be used to quantitatively explain numerous disagreements in the literature between observations and theoretical predictions of transient behavior.^{26,108,133}

Although the non-uniform mobility model provides many improvements over previous models, it also has several drawbacks. In particular, it is mathematically undefined for $V_G > V_P$, and it does not fit well to data for $V_G < 0$. Therefore, it is worthwhile to introduce a more detailed model that takes into account unique physics that occur in the abovementioned voltage ranges. Such a model is the topic of the next chapter.

CHAPTER III

INFLUENCE OF DISORDER ON TRANSFER CHARACTERISTICS OF ORGANIC ELECTROCHEMICAL TRANSISTORS

The non-monotonic dependence of transconductance on gate voltage is a ubiquitous property of OECTs. However, this behavior is not described by existing models, including the non-uniform mobility model described in chapter II. We show that the non-monotonic transconductance arises from the influence of disorder on the electronic transport properties of the organic semiconductor and occurs even in the absence of contact resistance. To explain this behavior, we present a model based on the physics of electronic conduction in disordered materials. This model fits experimental transconductance curves and describes strategies for rational material design to improve OECT performance in sensing applications.

A. Introduction

As discussed in the previous chapters, OECTs transduce voltage signals in the gate circuit to changes in the drain current with significant amplification of signal power.^{30,84} This makes OECTs useful in many biosensing applications,⁵¹ especially the recording of sub-mV electrophysiological signals.^{67,69,134} Transistor signal transduction is characterized by transfer curves, which describe the dependence of drain current, I_D , on gate voltage, V_G . The derivative of the transfer curve is transconductance, $g_m \equiv \frac{\partial I_D}{\partial V_G}$, which is a figure-of-merit for describing transduction efficiency. As discussed in chapter I, the volumetric doping in OECTs endows these devices with transconductance values exceeding that of other transistor technologies.^{28,30} However, OECT transconductance has a non-monotonic dependence on gate voltage, decreasing at both high and low gate voltage. This behavior has been observed since the first OECTs were reported in the seminal work of Wrighton et al., in 1984.¹ It is a ubiquitous property of OECTs, reported in devices made with different organic semiconductors – including polythiophenes,

polyaniline, polypyrrole, and polyacetylene^{18,19} as well as different source-drain electrodes – such as gold,³⁰ PEDOT:PSS,⁶¹ and carbon.¹³⁵ Moreover, non-monotonic transconductance occurs for various electrode geometries^{1,15,16,61,136} and a wide range of fabrication technologies – including orthogonal photolithography,¹³⁷ parylene-based photolithography,³⁰ screen printing,¹³⁸ and inkjet printing.¹³⁹

Despite numerous reports of bell-shaped transconductance in OECTs, existing models do not predict this behavior. For example, the Bernards model predicts that transconductance is constant in the linear regime and decreases linearly with gate voltage in the saturation regime.²⁶ Other models for OECTs assume a non-linear relationship between conductivity and charge carrier concentration in the polymer,^{24,140} and, as noted in chapter II, hopping transport would cause such a relationship. Although these models fit experimental results showing non-constant transconductance in the linear regime, they do not predict a bell-shaped dependence of transconductance on gate voltage. Nonetheless, the partial success of these models suggests that material disorder causes non-linear transfer curves in OECTs.

Another proposed explanation for this behavior is a gate-dependent contact resistance. Gate-dependent contact resistance causes bell-shaped transconductance in organic FETs,^{141,142} and this effect was recently explored in OECTs.⁷ V. Kaphle et al. used an empirical model for the dependence of contact resistance on gate voltage and showed that this can lead to a non-monotonic transconductance. These results suggest that this behavior is not an intrinsic property of OECTs, but rather a result of poor electrical contact to the channel.

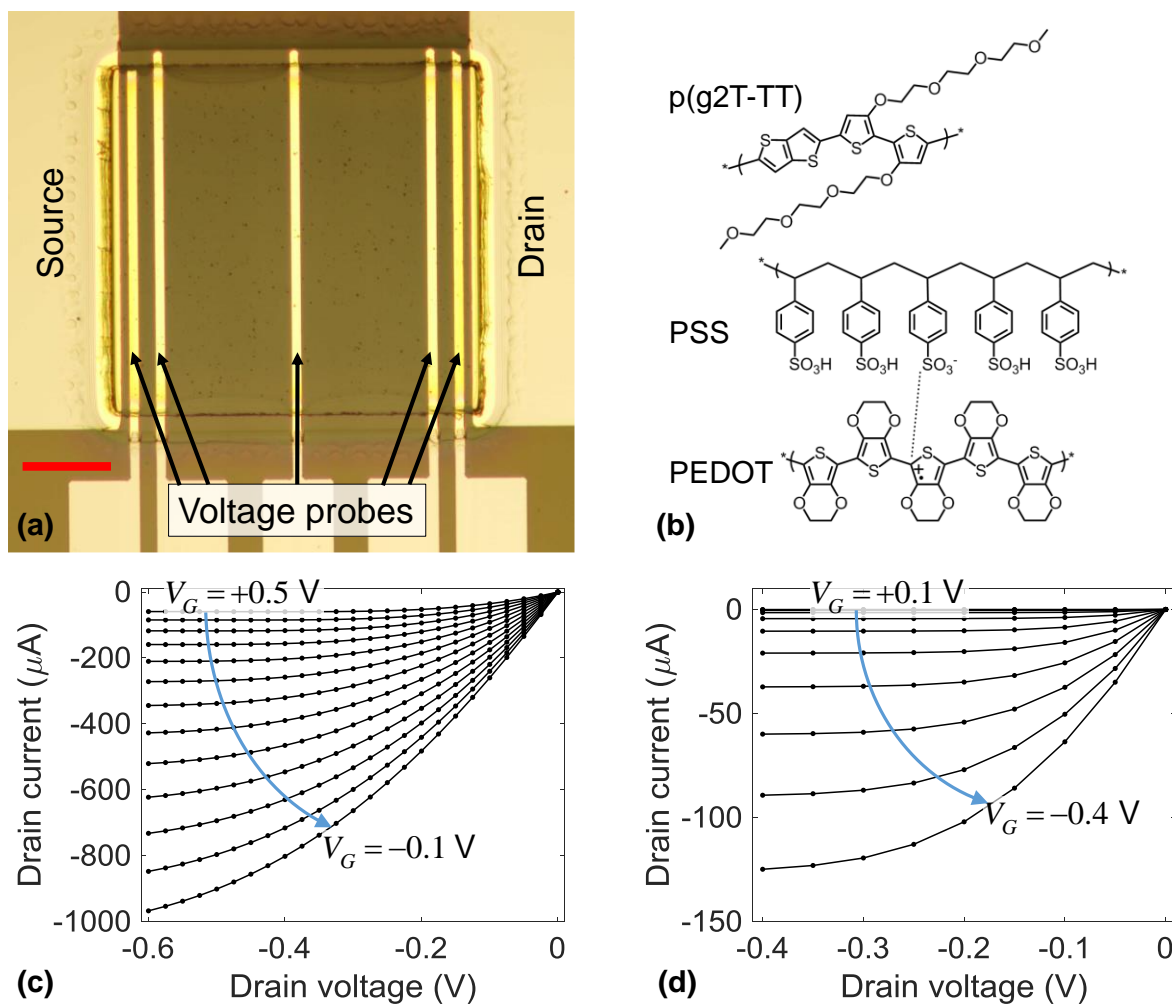


Figure III-1. OEFT geometry, polymer structures, and steady-state characteristics. (a) Bright-field image of an OEFT with voltage probes. The scale bar is $50 \mu\text{m}$. (b) Structure of poly(2-(3,3-bis(2-(2-(2-methoxyethoxy)ethoxy)ethoxy)-[2,2'-bithiophen]-5-yl)thieno[3,2-b]thiophene) – abbreviated p(g2T-TT) (top) and PEDOT:PSS (bottom). (c) – (d) Output curves of an OEFT with (c) a PEDOT:PSS channel and (d) a p(g2T-TT) channel.

To examine the cause of the non-monotonic transconductance in OEFTs, we fabricated OEFTs on glass substrates with gold source and drain contacts, and we included probes for voltage measurements at five positions along the OEFT channel, as shown in Figure III-1a. We used these probes for two purposes. First, we measured the voltage along the OEFT channel and extracted the voltage drop at the source electrode due to contact resistance. Second, we made 4-wire conductance measurements by using the outermost voltage probes for the sense contacts while using the source and drain as force contacts in a standard Kelvin configuration. The OEFT

channels consisted of either PEDOT:PSS or p(g2T-TT) as the semiconductor (see Figure III-1b). PEDOT:PSS is a two-phase polymer salt where the semiconducting PEDOT phase is doped by PSS (see chapter I); whereas, p(g2T-TT) is single-phase polymer without any native dopants.¹⁰ This material distinction allows fabrication of both depletion and accumulation mode OECTs (see chapter I), and hence provides an opportunity to probe the generality of our conclusions. We used a typical OECT geometry with 100 mM NaCl in water as the electrolyte and a 12.5 mm² Ag/AgCl pellet as the gate electrode. Additional experimental details are available in Appendix II.

B. Effect of contact resistance on transfer curves

Figure III-2a shows the contact resistance for a PEDOT:PSS-based transistor. Although it is not possible to measure contact resistance at the drain electrode because of depletion effects, if we assume that it is nearly the same as at the source electrode, we find that the total contact resistance in the PEDOT:PSS-based OECT could be up to 20% of the total resistance (see Figure VIII-4 in Appendix II). Therefore, in PEDOT:PSS-based OECTs with this W/L ratio geometry, contact resistance noticeably influences the transfer characteristics. In contrast to the PEDOT:PSS-based OECT, the p(g2T-TT)-based OECT (Figure III-2b) has contact resistance that contributes negligibly to the total resistance. Figure III-2c and Figure III-2d show how contact resistance affects the transfer and transconductance curves. Contact resistance has an effect on the transfer curves for 2-wire measurements, but it has no effect on 4-wire measurements because separate electrodes are used for supplying voltage and measuring current, as in typical four point probe measurements. By comparing the 2-wire and 4-wire measurements, one can see that contact resistance in PEDOT:PSS-based OECTs reduces the transconductance by about 10% at gate voltages less than 0.2 V. Nonetheless, non-monotonic transconductance is

evident in the 4-wire measurements for both PEDOT:PSS and p(g2T-TT), even though these measurements are unaffected by contact resistance. Therefore, contact resistance is not the primary cause of non-monotonic transconductance.

In addition to 4-wire measurements, we also made transmission line measurements using PEDOT:PSS-based OEETs with different channel lengths and widths. For each device, we extracted the total ON-state resistance by fitting the current vs. voltage curve to a straight line in the linear regime of operation ($V_G = -0.4$ V and -0.1 V $< V_D < 0.1$ V). To find contact resistance, we plotted total channel resistance as a function of channel length, width, and thickness in a manner similar to the modified transmission line method of Xu et al.¹⁴³ Fitting these curves to a straight line yields the channel resistivity (y-intercept) and the contact resistance (slope). The results are plotted in Figure III-3a, and the best fit was obtained with a contact resistance of 64 Ω and a channel conductivity of 380 S/cm. Therefore, we expect that contact resistance contributes negligibly to the total resistance of the OEET with a channel width of 10 μm , a channel length of 250 μm , and a total resistance of more than 4500 Ω . Even though this device has negligible contact resistance ($< 2\%$ of total resistance), the transconductance clearly still has a non-monotonic dependence on gate voltage (Figure III-3b). Therefore, the transmission line measurements support the conclusion from the 4-wire measurements; contact resistance is not the primary cause of non-monotonic transconductance.

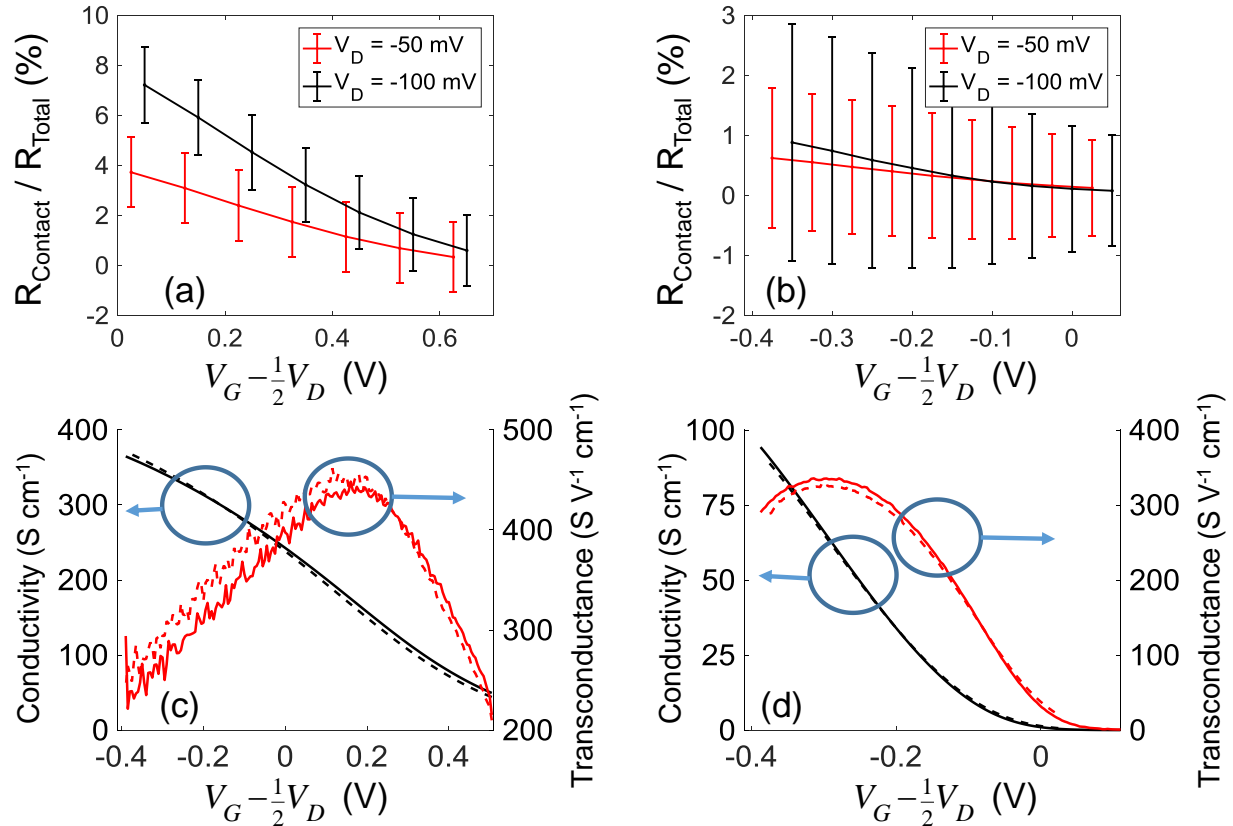


Figure III-2. Effect of contact resistance. (a) – (b) Contact resistance at the source electrode divided by the total resistance (contact resistance plus channel resistance) for (a) a PEDOT:PSS-based OEET and (b) a p(g2T-TT)-based OEET. (c) – (d) Channel conductivity and normalized transconductance ($g'_m \equiv g_m/|V_D| \times L/(Wh)$, where V_D is the drain voltage and L, W, h are the channel length, width, and thickness, respectively) for (c) a PEDOT:PSS-based OEET and (d) a p(g2T-TT)-based OEET. In (c) and (d), dashed lines are 4-wire measurements, and solid lines are 2-wire measurements. Error bars in (a) and (b) are calculated as described in the supplementary material. In (c), both the 2-wire and 4-wire measurements were made with $V_D = -10$ mV. In (d) $V_D = -25$ mV for the 2-wire measurements, and $V_D = -50$ mV for the 4-wire measurements. In (a)-(d), instead of using the gate voltage, V_G , we have used the median gate-channel voltage, $V_G - V_D/2$ on the horizontal axis to facilitate comparison between measurements made at different drain voltages. Both devices have $W = 200 \mu\text{m} \times L = 200 \mu\text{m}$ for 2-wire measurements and $L = 180 \mu\text{m}$ for 4-wire measurements. For PEDOT:PSS $h \approx 100$ nm, and for p(g2T-TT) $h \approx 85$ nm.

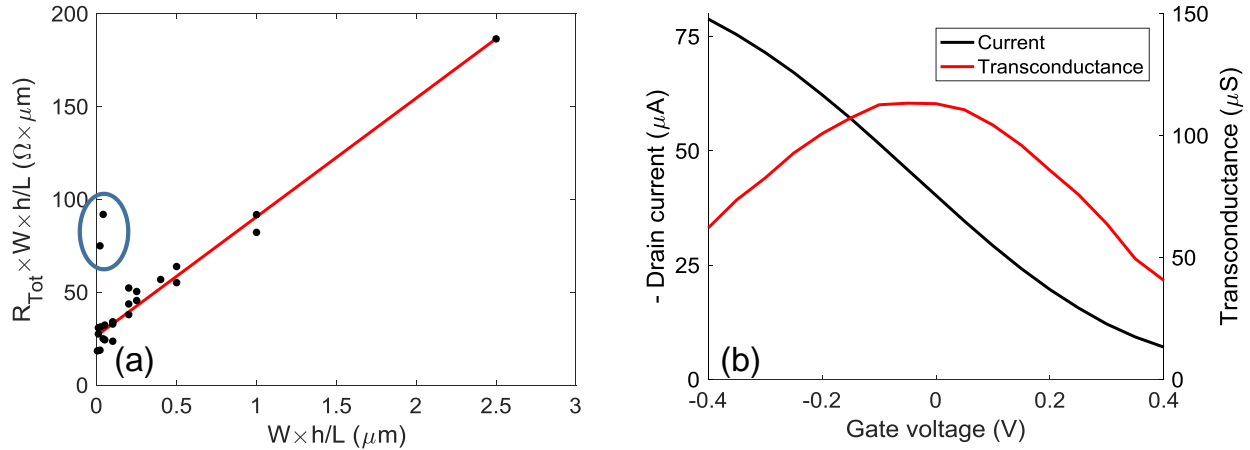


Figure III-3. Transmission line method measurements. In panel (a) the solid line is the best linear fit to the data. The two data points enclosed in a circle were excluded from the fit. (b). Transfer and transconductance curves for the transistor with $W = 10 \mu\text{m}$ and $L = 250 \mu\text{m}$ at $V_D = -0.4 \text{ V}$. All measurements used 2-wire local sensing on the channel, not 4-wire Kelvin measurements.

C. The disorder model

1. Model description and data fitting

Because we found that contact resistance is not the primary cause of the non-ideal transfer curves, we modeled OECT behavior using a modified form of Ambegaokar, Halperin, and Langer's theory for hopping conduction in disordered materials.¹⁴⁴ Figure III-4 shows the fit between this model and the experimental data. Briefly, the model assumes a Gaussian-shaped energy density of states (DOS) and a Miller-Abrahams form of detailed balance for transition rates between nearest-neighbor hopping sites.¹⁴⁵ The present model is discussed in more detail in the supplementary material and predicts that as the gate voltage is made more negative, more holes are added to the semiconductor, filling the DOS. At first, when the DOS is much less than half full, adding holes increases both the hole concentration and the hole mobility. In this regime, transconductance increases as the gate voltage is made more negative. As the DOS becomes nearly half full, the rate of increase of both hole concentration and mobility slows, causing a decrease in transconductance as the gate voltage is made more negative. When the DOS is more

than half full, adding more holes decreases hole mobility, and the transconductance becomes negative (see Figure VIII-1 in Appendix II). These predictions qualitatively agree with other theoretical and experimental studies that show a non-linear relationship between conductivity and charge carrier concentration.^{112,114,146-148}

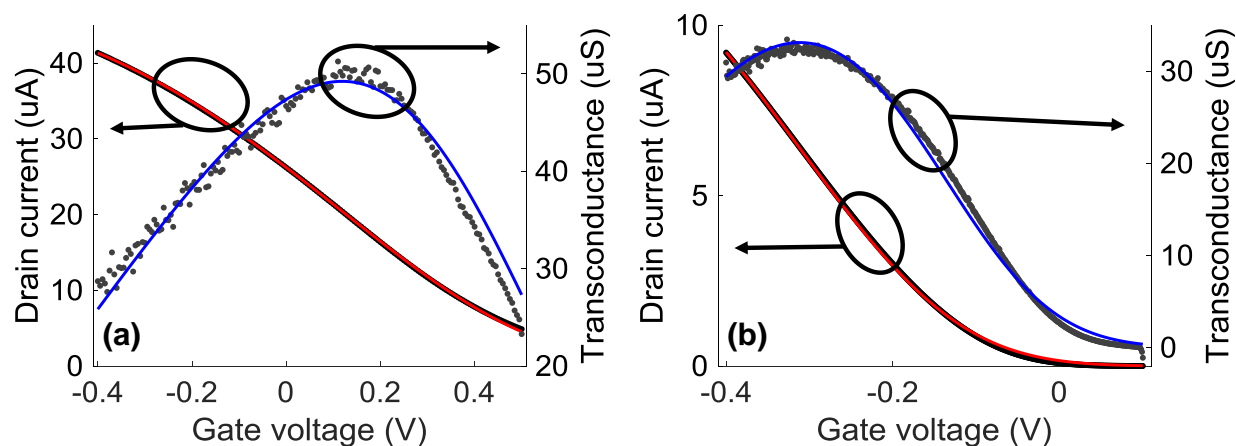


Figure III-4. Disorder model fit to OECT transconductance for (a) a PEDOT:PSS-based OECT and (b) a p(g2T-TT)-based OECT. In both figures, the solid blue curve is the fit to the transconductance, the solid red curve is the model prediction for the drain current, the black dots are the experimentally measured drain current, and the gray dots are the experimentally measured transconductance. $V_D = -10$ mV and 4-wire sensing is used for both (a) and (b).

2. Discussion of fit parameters

The proposed model fits the transconductance curves of both PEDOT:PSS-based and p(g2T-TT)-based OECTs with four free parameters. As predicted by the model, these polymers exhibit an initial increase and subsequent decrease of transconductance as gate voltage becomes more negative. The model further predicts that at more negative gate voltages the transconductance will become negative, but we were not able to observe this behavior because we had to avoid the over-oxidation of PEDOT and the electrolysis of water. Other polymer/electrolyte systems are stable at more negative gate voltages, and OECTs with those materials do exhibit the full range of predicted features – including negative transconductance.^{19,122} Extracted values for the four fit parameters are listed in Table III-A; σ_0 is

the polymer conductivity at $V_G = 0$ V for PEDOT:PSS and at $V_G = -0.4$ V for p(g2T-TT); E_0 is the energetic position of the peak of the DOS with respect to the Ag/AgCl electrode; σ_{DOS}^2 is the DOS variance; and η is the critical probability of bond connectivity required for percolation.

Table III-A. Fit parameters for the disorder model.

	σ_0 (S/m)	σ_{DOS} (meV)	E_0 (meV)	η (%)
PEDOT:PSS	278 +/- 0.6	950 +/- 30	-830 +/- 60	0.1 +/- 0.01
p(g2T-TT)	96 +/- 0.5	410 +/- 10	-640 +/- 10	1.0 +/- 0.1

The extracted σ_0 values are similar to reported values for PEDOT:PSS and p(g2T-TT),^{4,14,28} and the extracted DOS widths (σ_{DOS}) are about one order of magnitude larger than that reported for dry films of polythiophenes.^{149,150} However, DOS widths for electrochemically doped polythiophenes can broaden significantly.^{122,151,152} The critical bond connectivity, η , extracted by the proposed model for p(g2T-TT) is about one order of magnitude smaller than expected for close-packed spheres, and for PEDOT:PSS it is about two orders of magnitude smaller than expected.¹⁴⁴ However, η decreases strongly as the aspect ratio of conducting structures increases,¹⁵³ and conduction in polymers depends on high aspect ratio structures due to carrier delocalization along polymer backbones¹⁵⁴ and anisotropic phase segregation.¹⁵⁵ Therefore, η is expected to be much smaller in polymers than in systems composed of close-packed spheres.

3. Comparison with non-uniform mobility model

In chapter II, we presented a model for the steady-state behavior of OECTs, and in this chapter, we developed a different model that also describes OECT steady-state behavior. Therefore, it makes sense to consider the strengths and weaknesses of these two models as well as the different assumptions they rely on. Both the non-uniform mobility model (chapter II) and the disorder model (chapter III) are based on the work of V. Ambegaokar, B. I. Halperin, and J. S. Langer (AHL) regarding hopping conductivity in disordered systems.¹⁴⁴ The non-uniform

mobility model derives almost directly from the work of M. C. J. M. Vissenberg and M. Matters (VM), who built on AHL's work by showing the effects of hopping conductivity in disordered materials with an exponential DOS.¹¹⁹ VM showed that the hole mobility in such a system has a power law dependence on hole concentration (see equation (II.1)). The non-uniform mobility model uses this expression for the mobility and relies on the assumption of a constant capacitance to calculate hole concentration (see equations (II.2) and (II.3)). Like the non-uniform mobility model, the disorder model follows the work of AHL. However, unlike the VM and non-uniform mobility models, the disorder model assumes a Gaussian-shaped DOS and a linear relationship between Fermi-level and applied voltage. This assumption, combined with a Gaussian DOS and Fermi-Dirac statistics, implies a non-constant ionic capacitance in the OECT.

Because the tail of the Gaussian DOS resembles an exponential, the disorder model is more comparable to the VM and non-uniform mobility models at low hole concentrations (see Figure III-5a). In this regime, the VM model predicts that conductivity depends exponentially on Fermi level with a slope of $1/(kT)$ regardless of the slope of the exponential DOS. One can recognize this prediction by considering equations (4) and (8) from VM.

$$\sigma = \sigma_0 \exp(-s_c) \text{ -- VM eqn (4)}$$

$$B_c \approx \pi \left(\frac{T_0}{2\alpha T} \right)^3 N_t \exp\left(\frac{-E_F + s_c kT}{kT} \right) \text{ -- VM eqn (8)}$$

Solving these equations yields an exponential dependence of conductivity on Fermi level as shown below

$$\sigma \approx \sigma_0 \left(\frac{\pi N_t}{B_c} \right)^{\frac{T_0}{T}} \left(\frac{T_0}{2\alpha T} \right)^{\frac{3T_0}{T}} \exp\left(\frac{-E_F}{kT} \right), \quad (\text{III.1})$$

where σ is the conductivity; σ_0 is an unknown prefactor; s_c is the exponent for the critical conductivity; B_c is the critical bond connectivity; T_0 describes the slope of the exponential DOS; α is a wavefunction overlap parameter; T is the temperature; N_t is the total number of hopping

sites per unit volume; E_F is the Fermi level; and k is the Boltzmann constant. Because the disorder model has a nearly exponential DOS for energies greater than ~ 200 meV, we expect it to agree with VM and predict a conductivity that depends exponentially on E_F . Figure III-5b shows that the disorder model does in fact yield an exponential conductivity with a slope of $\sigma \propto \exp\left(-\frac{qV_G}{kT}\right)$. Because the disorder model assumes $E_F = q \times [V_G - V_0]$ the exponential slope in Figure III-5b agrees with VM. On the other hand, the non-uniform mobility model predicts a super-exponential decrease in conductivity.

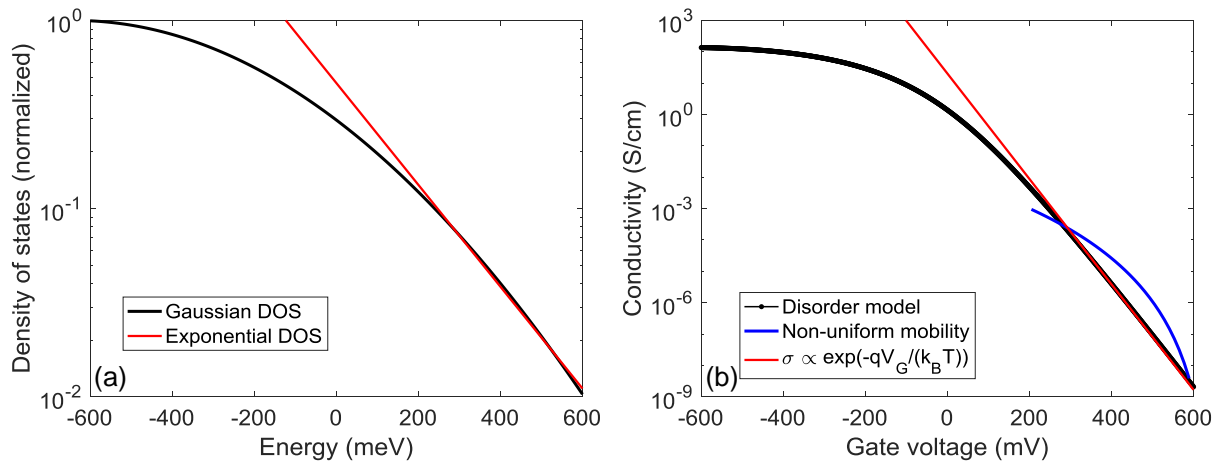


Figure III-5. Comparison of disorder model (chapter III) with the non-uniform mobility model (chapter II) and the VM model.¹¹⁹ Panel (a) shows an exponential fit to the Gaussian DOS used in the disorder model. Panel (b) shows the predictions of the three different models for low hole concentrations.

In addition to this discrepancy at low hole concentrations, the non-uniform mobility model and the disorder model make substantially different predictions at high hole concentrations. In particular, the non-uniform mobility model uses a strictly monotonic DOS, so it cannot explain non-monotonic transconductance. Despite this shortcoming, the non-uniform mobility model possesses a significant advantage; it provides a closed-form expression for channel current; whereas, the disorder model requires numerical calculations. Therefore, if one needs an analytic model for OECT behavior, the non-uniform mobility model is the best choice,

but one must be careful to only use it in the regime of small positive gate voltages, where we have shown that it agrees with experimental measurements (see chapter II). Otherwise, the disorder model is a better choice.

4. Discussion

Non-monotonic transconductance induced by material disorder has several implications for OECT research. For instance, if contact resistance were the primary cause of the non-monotonic transconductance, as proposed by V. Kaphle et al.,⁷ the decrease in transconductance with more negative gate voltages could be prevented by changing the metals used for source/drain contacts and engineering the interfaces at these contacts. However, because non-monotonic transconductance is an intrinsic property of OECTs, such strategies will not eliminate the transconductance decrease at negative gate voltages. Our results suggest that researchers developing new materials should focus not only on maximizing transconductance, but also on ensuring that high transconductance occurs over a broad voltage window. In this respect, our model predicts a tradeoff in OECT performance; decreasing the DOS width increases the peak transconductance, conductance, and mobility but also decreases the width of the voltage range over which transconductance remains near its peak. However, our model suggests that one can work around this tradeoff by engineering η because as η decreases, the transconductance peak becomes higher without becoming narrower (see Figure VIII-1g,f in Appendix II). Therefore, designing materials with highly anisotropic conducting structures could improve OECT performance. Unfortunately, it is not clear in the present model whether anisotropy is most important at the molecular level of carrier delocalization or at the microscopic level of phase segregation. Finally, new materials should be designed such that the maximum transconductance occurs at voltages within the stable operating regime of the transistor/electrolyte system. This

could be accomplished by adjusting the electronegativity of side-chain constituents to shift the HOMO level of the semiconducting polymer.¹⁵⁶ Altogether, the present model suggests several design strategies for OECT materials:

- (1) Increase the anisotropy of conducting structures.
- (2) Adjust the HOMO level so that peak transconductance occurs within the operational voltage range.
- (3) Tailor the DOS width on a case-by-case basis according to the tradeoff between maximizing peak transconductance and broadening the window of high transconductance.

D. Conclusion

In conclusion, we fabricated accumulation-mode and depletion-mode OECTs based on two different polymer semiconductors, and we showed that both materials exhibit non-monotonic transconductance. Using 4-wire conductance measurements and transmission line measurements, we showed that non-monotonic transconductance occurs even in the absence of contact resistance. We developed a model based on hopping transport in disordered materials and demonstrated that it explains the transconductance of OECTs, thus supporting the conclusion that non-monotonic transconductance is an intrinsic property in OECTs. The model presented in this chapter provides predictions about how material parameters, such as delocalization length, HOMO level, and DOS width, affect OECT transfer characteristics. These results will inform the design of materials for improved OECT performance in sensor applications.

CHAPTER IV TIME DOMAIN MODELING OF OECT BEHAVIOR

A. Introduction

As mentioned in previous chapters, OECTs are promising platforms for biosensing applications.^{51,53,157,158} For instance, OECTs can be used for in vivo electrocorticographic (ECoG) arrays to detect epileptic activity⁶⁹ or in vitro to detect the activity of cardiac cells.¹⁵⁹ OECTs have also been used for long-term electrocardiogram recordings,^{67,134} measuring metabolite concentration,^{27,54,56,57,60} and monitoring barrier-cell properties.^{63,64,102,131,160} Several reports also demonstrate OECT implementations of digital logic^{33–35,161} and neuromorphic circuits.^{74,75,162} The transient behavior of OECTs is critical in all of the applications mentioned above. For example, 10-100 kHz operation is necessary for high-accuracy resolution of neuron action potentials. In neuromorphic applications, the response speed following a gate pulse determines learning times, and in digital logic circuits transistor bandwidth is an important performance specification. Unfortunately, OECTs are slow devices, with time constants typically on the order of 1-100 ms^{67,105,136,163} and sometimes larger than 1 s.^{108,164–167} These slow speeds are an inherent consequence of the switching mechanism in OECTs, which relies on the injection of ions into the transistor channel. The time constant for ion injection determines the limiting speed for the OECT, independent of hole drift times along the channel. This ionic speed is a severe limitation for device performance because strategies to increase the ionic speed degrade other performance parameters. For instance, decreasing channel thickness increases switching speed but causes a proportional decrease in transconductance.^{28,30} Similarly, decreasing the concentration of secondary polar dopants increases device speed but decreases channel conductance and transconductance.⁹⁷ Also, removing the crosslinker 3-

glycidoxypropyltrimethoxysilane increases device speed but allows delamination during device operation.^{99,137}

In this chapter, we demonstrate that the slow ionic speed of OECTs need not limit their performance. We show that the OECT response can be made 30 times faster than its ionic speed when the drain bias is tuned to the step-response voltage, V_{step} . Furthermore, we provide a model that accounts for this high-speed behavior and can be used to understand the transient response of OECTs in a variety of applications.

B. Faster than ionic response

1. Background

As described in chapter I and shown in Figure IV-1, a positive input voltage at the gate electrode modulates the channel current by pushing cations from the electrolyte into the PEDOT:PSS matrix. The cations form ionic bonds with the PSS, compensating the counter charge for holes and thus decreasing the hole concentration in the PEDOT. Removing holes from the PEDOT makes the channel less conductive and decreases the OECT's output current. Alternatively, a negative gate voltage pushes anions into the channel, increasing the hole concentration and thus increasing the OECT's output current. To date, every reported OECT has operated no faster than the time required to charge the transistor channel with the ionic species. This ionic time constant is analogous to the RC time constant of a simple resistor-capacitor circuit, and because OECTs have large capacitances (~ 50 nF for $100 \mu\text{m} \times 100 \mu\text{m}$ devices),²⁸

the time constant is typically quite slow – even reportedly fast devices have time constants of approximately 1 ms.¹³⁶

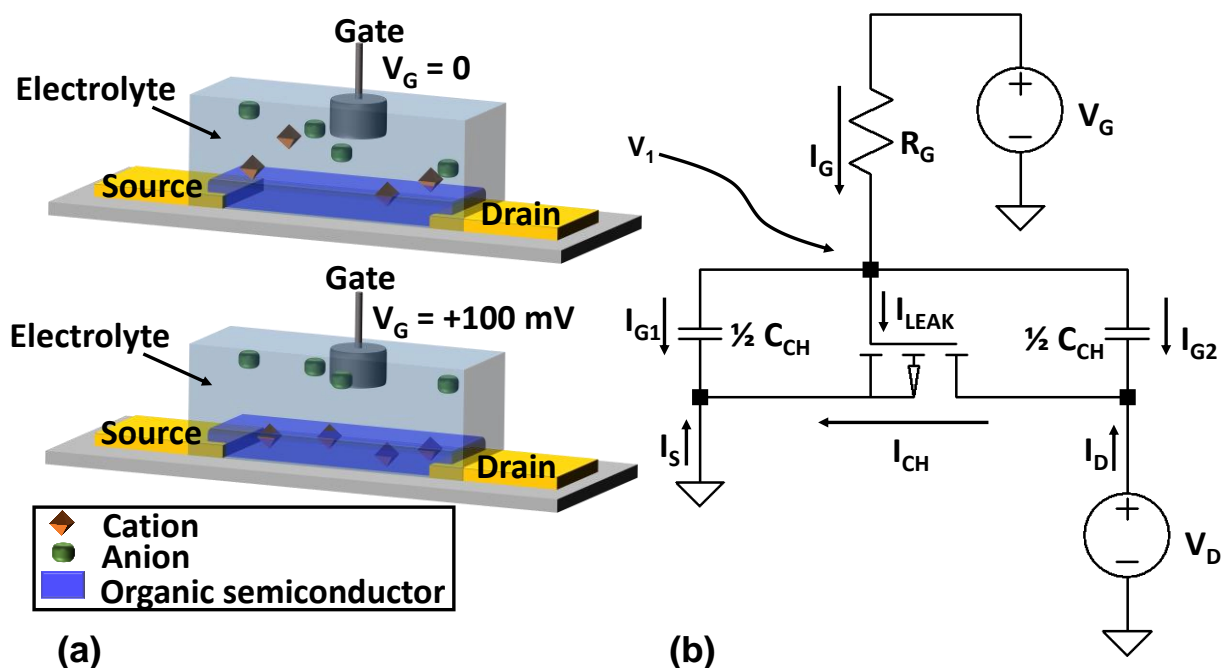


Figure IV-1. (a) Structure and operation of a typical OEET with a PEDOT:PSS channel. Top: OEET channel in the high-conductivity state with a gate voltage of 0 V. Bottom: The gate voltage of +100 mV pushes cations into the OEET channel. These cations de-dope the organic semiconductor, lowering its conductivity. (b) Circuit diagram of the discrete model showing the gate current branches and the distinct source (I_S), drain (I_D), and channel (I_{CH}) currents.

2. 20 μ s step response

Although ion transport is an essential part of OEET operation and usually determines the response speed, we show that it is possible to overcome this limitation. Figure IV-2 shows the source current response to a gate voltage step from 20 mV to 0 mV with a constant drain voltage. We tested the OEET with the drain voltage fixed at -30 mV (Figure IV-2a,d), -80 mV (Figure IV-2b,e), and -130 mV (Figure IV-2c,f). At -30 mV and -130 mV the source current exponentially relaxes to steady-state in ~ 600 μ s, but in Figure IV-2b the change in source current settles to within 10% of its final value in only 20 μ s. We can compare this 20 μ s

response to the ionic speed by measuring the gate current, which is equal to the ionic charging current of the OECT. Figure IV-2e shows the gate current corresponding to the source current shown in Figure IV-2b. The gate current is an exponential function with a time constant of 300 μs and requires more than 690 μs to settle to less than 10% of its peak value. Therefore, the source current response exceeds the speed of the ionic circuit by more than a factor of 30.

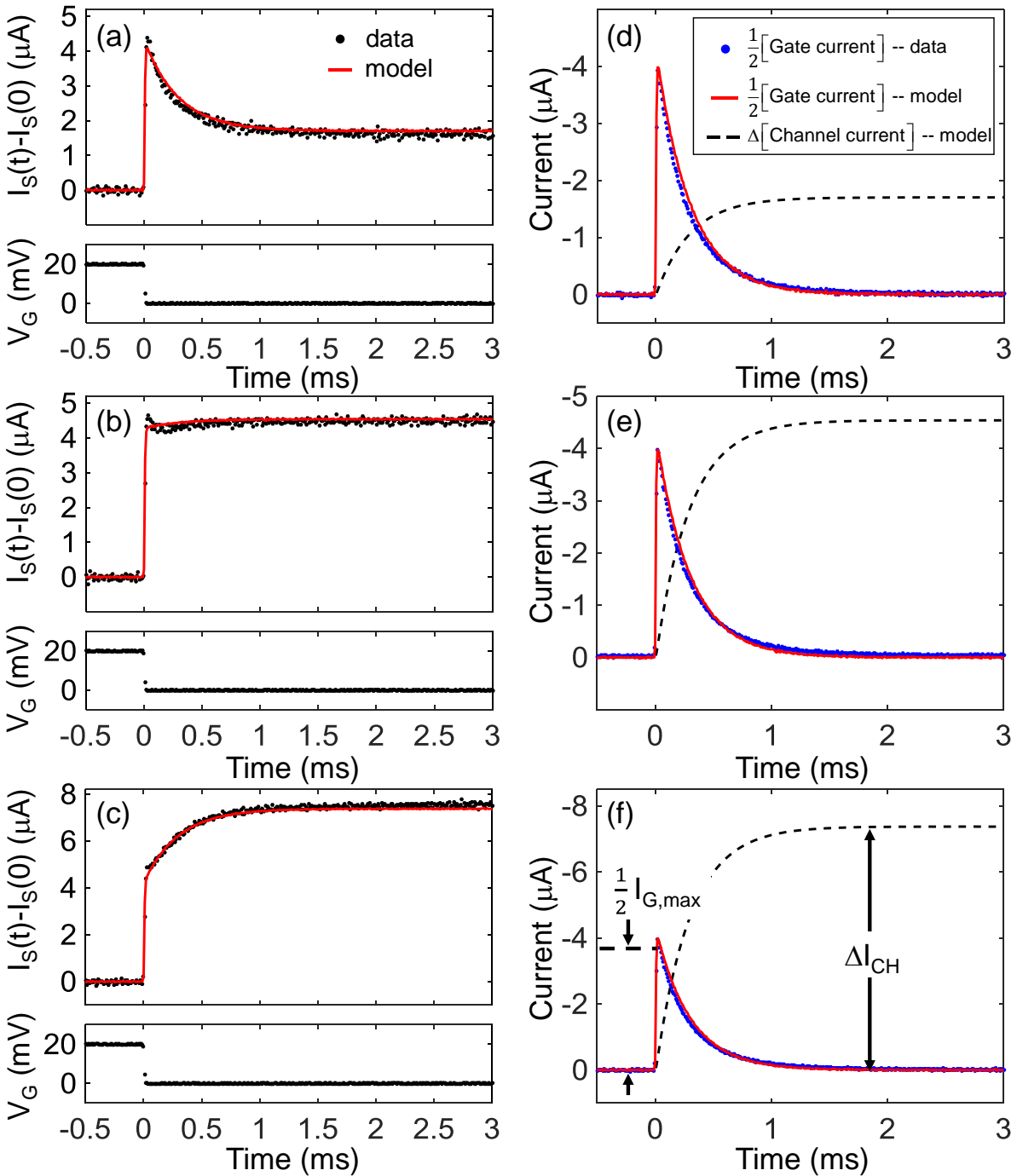


Figure IV-2. (a)-(c) Change in the source current following a gate voltage step. (d)-(f) Gate current and the change in channel current corresponding to the source currents shown in (a)-(c). The drain voltage is -30 mV for (a) and (d), -80 mV for (b) and (e), and -130 mV for (c) and (f). The gate voltage waveform is shown in the lower 1/3 of the panel in (a)-(c). In all panels, the data were averaged over 16 repeated waveforms. The resulting averages are plotted as dots and model fits are plotted as solid lines. The device had a channel width of $W = 260 \mu\text{m}$, a channel

length of $L = 100 \mu\text{m}$, and a channel thickness of approximately $h = 150 \text{ nm}$. The values $\frac{1}{2}I_{G,max}$ and ΔI_{CH} are labeled in (f).

C. Discrete circuit model for OECT transient response

This observation of source current response speed exceeding the ionic speed has not been previously reported. However, we can explain this faster-than-ionic response by building on previous descriptions of OECT behavior.^{24,26,27,123,124} Bernards and Malliaras modeled OECT behavior with a standard long-channel field-effect transistor (FET) and a series resistor-capacitor (RC) circuit between the gate and channel.²⁶ The FET describes the steady-state behavior of the OECT, and the RC circuit describes the ionic coupling through the electrolyte between the gate and the channel. This RC series can be understood as an approximation for equivalent circuits typically used to describe ion transport.^{52,168–170} The RC time constant of this *ionic* circuit determines the limiting speed of the *electronic* OECT response, regardless of electronic transit times along the channel.²⁶ Despite finding this, the Bernards model does not provide a closed-form expression for OECT transient behavior because it fails to account for spatially varying hole currents in the channel before steady-state is reached. Forchheimer et al. provide a model without this shortcoming by describing the transient behavior of electrolyte-gated FETs with the Ward-Dutton partition scheme.¹²⁴ Forchheimer et al.'s model highlights the fact that the source and drain currents are not necessarily equal because the transient gate current contributes differently at the source and drain terminals. Our discrete model follows the work of Bernards and Forchheimer, describing the ionic circuit with a series RC, and allowing unequal source and drain currents in the transient regime.

The discrete model is depicted in Figure IV-1b and consists of four discrete circuit elements – a resistor describing the ionic resistance between the gate electrode and the transistor channel,^{26,106} two capacitors describing the accumulation of ionic charge in the transistor

channel,^{26,28} and an ideal p-channel FET describing the OEET's steady-state current-voltage relationships.²⁶ The discrete model makes the quasi-static approximation that the charge distribution in the channel and the voltage profile in the channel are given by the steady-state solution to the instantaneous source and drain voltages as well as the instantaneous effective gate voltage (V_1 in Figure IV-1).^{171,172} Additionally, the discrete model assumes that the leakage current, I_{Leak} , is negligible. Under these assumptions, the discrete model predicts the source and drain currents given by

$$\begin{aligned} I_S &= -(I_{CH} + I_{G1}) \\ I_D &= I_{CH} - I_{G2} \end{aligned} .$$

Following the Meyer partition,¹⁷² we can find I_{G1} and I_{G2} by assuming that half of the gate current flows to the source terminal and half flows to the drain terminal. If the gate voltage is a square step, the channel current is $I_{CH}(t) = I_{CH}(0) + \Delta I_{CH}[1 - \exp(-t/\tau_{RC})]$, and the gate current is $I_G(t) = I_{G,max} \exp(-t/\tau_{RC})$ (see Appendix III). The ionic RC time constant, τ_{RC} , limits the response speed of the OEET; however, when $\Delta I_{CH} = \frac{1}{2} I_{G,max}$, the source current will respond to a square voltage step with a square current step. Each row of Figure IV-2 corresponds to a different drain voltage, and, because increasing the drain voltage increases ΔI_{CH} but does not affect $I_{G,max}$, each row of Figure IV-2 also corresponds to a different $\Delta I_{CH}/I_{G,max}$ ratio. Figure IV-2c and Figure IV-2f show the monotonic regime; in this regime the source current has a small positive step followed by an exponential increase until steady state is reached. The monotonic regime occurs when V_D is large enough that $\Delta I_{CH} > \frac{1}{2} I_{G,max}$, as shown in Figure IV-2f. Figure IV-2a and Figure IV-2d describe the opposite behavior, the spike-and-recover regime. In this regime, the source current displays a large positive step followed by an exponential *decrease* until steady-state is reached. As shown in Figure IV-2d, this regime occurs when V_D is small enough that $\frac{1}{2} I_{G,max} > \Delta I_{CH}$. At the boundary between the monotonic and the spike-and-recover

regimes is the step-response voltage, V_{step} . When the constant drain bias equals the step-response voltage, $V_D = V_{step}$, and the gate voltage is a square step, the source current responds with a step function. As shown in Figure IV-2e, this step response occurs when $\frac{1}{2}I_{G,max} = \Delta I_{CH}$. At the step-response voltage, the transient components of the gate and channel currents cancel each other at the source terminal, and the source current steps almost instantaneously from one steady-state value to another.

The shape of the source current varies greatly among Figure IV-2a-c, yet the data all come from the same device with the same intrinsic properties. This is made apparent by Figure IV-2d-f, which shows that the corresponding gate currents can each be fit with a single exponential and a time constant of 300 μ s. This demonstrates that the source current responds faster at -80 mV than at -30 mV and -130 mV even though τ_{RC} is the same for all three cases. Being able to vary the transient operation regime could be useful in applications that require faster-than-ionic responses. For instance, a 20 μ s step response is certainly fast enough to drive video displays,¹⁷³ and in neuromorphic devices, relaxation into the long-term-memory state would be much faster if the OECT were biased at V_{step} . However, restrictions on the step-response regime may limit its usefulness in other applications. For instance, V_{step} may not be large enough to drive an LED and will lead to a less than unity current gain ($\Delta I_D/\Delta I_G$) at high frequencies (\gtrsim 400 Hz). Also, logic circuits will have to be carefully designed to rely on the response speed at the positive end of the OECT channel (source current) rather than at the negative end of the channel (drain current).

The results in Figure IV-2 not only demonstrate a method of exceeding the ionic speed of an OECT, but they also demonstrate the robustness of our discrete model. This model uses four parameters to describe the OECT response to an arbitrary gate voltage. The four parameters are

the ionic resistance, R_G ; the ionic capacitance, C_{CH} ; a hole mobility, μ , describing the electronic mobility of the holes in the transistor channel; and a pinch-off voltage, V_P describing the voltage at which the OECT transitions from linear to saturation behavior.^{24,26,28} In this chapter, all measurements are made in the linear regime, so V_P can be eliminated from the expressions for changes in the source, drain, and gate currents. The discrete model's fit to the source and gate currents is shown with solid red lines in Figure IV-2. Even though Figure IV-2 shows all three transient operating regimes, the data are all simultaneously fit by the discrete model with the same three fit parameters: $R_G = 2340 \pm 90 \Omega$; $C_{CH} = 127 \pm 6 \text{ nF}$; and $\mu = 2.2 \pm 0.1 \text{ cm}^2\text{V}^{-1}\text{s}^{-1}$.

D. Discrete model results

1. Predicting OECT output

Not only does the discrete model predict faster-than-ionic OECT operation but it also predicts the response to arbitrary gate voltage waveforms. Figure IV-3 shows the source and drain currents as well as the discrete model's prediction for the response to a 20 mV gate voltage step (Figure IV-3a), a 1 mV Lorentzian gate voltage spike (Figure IV-3b), and a series of 10 mV sine waves at different frequencies (Figure IV-3c). These input waveforms were chosen because of their relevance to several OECT sensing and logic applications. Square inputs have been used for enzymatic sensing,⁵⁴ detecting barrier cell integrity,^{64,102,131} digital logic circuits,^{34,35} and neuromorphic processing.^{74,75} Lorentzian spikes mimic the shape of neuron action potentials that might be detected by ECoG arrays, and sine waves are used to characterize the frequency-domain behavior of OECTs for biosensing applications and analog circuit performance.^{84,134,160}

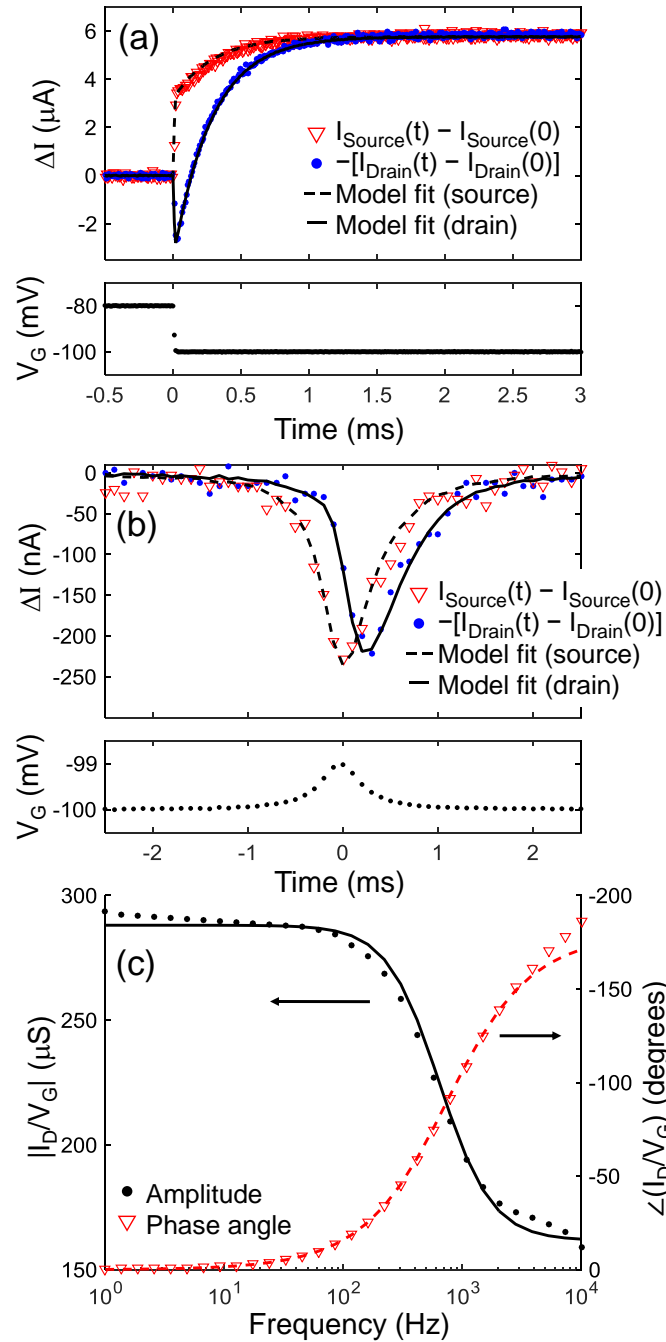


Figure IV-3. (a) Change in source and drain currents, ΔI , responding to a square gate voltage step (b) ΔI for a Lorentzian voltage spike. (c) Amplitude and phase of the transconductance as a function of the frequency of the sinusoidal gate voltage. In (a) and (b), the gate voltage waveform is on the lower 1/3 of the panel. In (a)-(c), the drain voltage is kept constant at $V_D = -100$ mV. In (a) and (b) the drain current is always negative, and the source current is always positive. We plotted the negative change in the drain current to facilitate comparison between the source and drain currents. In (a) and (b), the data were averaged over 19 and 24 waveform cycles, respectively. In (c) four frequency sweeps were performed. In (a)-(c) the resulting

averages are plotted as dots, and the model fits are plotted as solid lines. The device geometry was $W = 255 \mu\text{m}$; $L = 100 \mu\text{m}$; and $h \approx 150 \text{ nm}$.

Figure IV-3 shows that the discrete model simultaneously fits the responses to these different waveform shapes, amplitudes, and frequencies using only three free parameters. These model fits are shown in Figure IV-3 as solid lines, and the device parameters extracted from the fits are $R_G = 3090 \pm 50 \Omega$; $C_{CH} = 92 \pm 1 \text{ nF}$; and $\mu = 3.19 \pm 0.05 \text{ cm}^2\text{V}^{-1}\text{s}^{-1}$ – all of which are within the range of typical values reported in the literature.^{28,140,174}

Figure IV-3 demonstrates that the utility of our discrete model reaches beyond the scope of applications that require faster-than-ionic responses. In particular, the discrete model highlights the difference between the source and drain currents in high-frequency measurements, such as those shown in Figure IV-3a and Figure IV-3b. Figure IV-3b shows the source and drain responses to a Lorentzian-shaped gate voltage pulse. As predicted by the discrete model, the source current lags behind the gate excitation by less than $100 \mu\text{s}$, but the drain current lags behind the excitation by approximately $300 \mu\text{s}$. Without the discrete model, this time delay could confound the interpretation of transient measurements. For instance, neuron action potentials generate voltage signals with shapes similar to the input voltage used for Figure IV-3b, and delay times between action potentials from different neurons indicate the presence or lack of neural connections.¹⁷⁵ Therefore, mapping neural connectivity with OECT-based arrays depends on a complete understanding of the time delays between input voltages and output currents.

While proper design, operation, and interpretation of results are critical for OECT applications, the development of new materials is equally important. PEDOT:PSS is currently the most commonly-used material for OECTs, but because it contains the dopant PSS⁻, it can only be used for depletion-mode OECTs.^{8,26,33,84} This is a major drawback for both sensing and logic applications, and several materials for accumulation-mode OECTs have been developed.^{8,9}

We tested the generality of our model by fabricating an accumulation-mode OECT using an undoped polythiophene, p(g2T-TT) (see Figure III-1).¹⁰ We found that our model fits the time domain response of this accumulation-mode OECT and that the OECT is capable of a step response when biased at $V_D = V_{step}$ (see Figure IV-4).

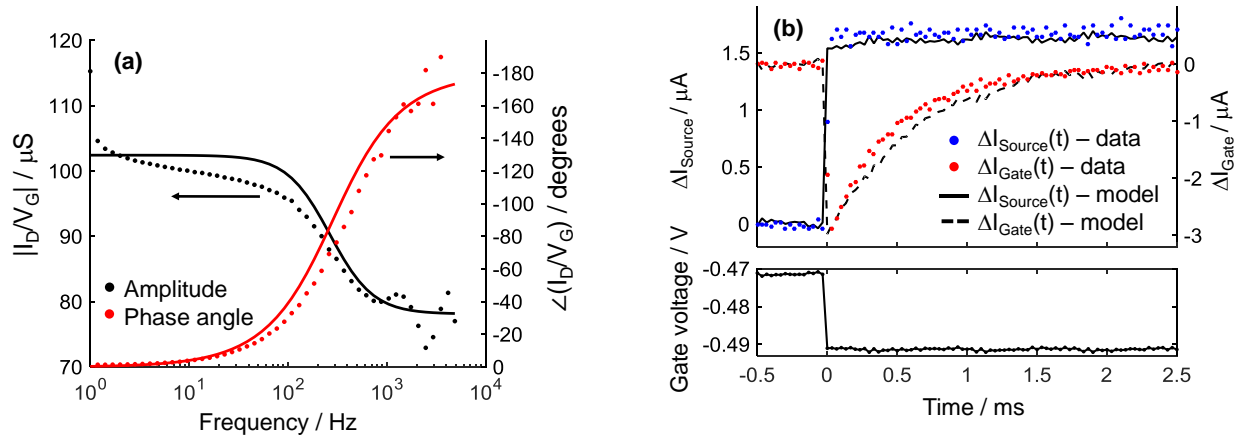


Figure IV-4. Frequency domain (a) and time domain (b) data for an OECT made with the undoped polythiophene, p(g2T-TT). The model fits are lines, and the data are dots. These results show that our model is able to fit data for more than one kind of OECT material and they show that even the accumulation-mode transistor yields a step-response at the source terminal when we apply the constant drain bias $V_{step} = -\frac{L^2}{2\mu R_G C_{CH}} = -80$ mV. The model parameters for these fits are $\mu = 1.3 \text{ cm}^2 \text{V}^{-1} \text{s}^{-1}$; $R_G = 6.1 \text{ k}\Omega$; and $C_{CH} = 74 \text{ nF}$. The device had a channel width of $72 \mu\text{m}$ and a channel length of $97 \mu\text{m}$.

2. Extracting material and device parameters

Because the discrete model is valid for OECTs made with any organic semiconductor, it is not only useful for interpreting high-frequency measurements, but it also can be used to estimate device and material parameters. The discrete model even describes a frequency-domain measurement of mobility that does not rely on estimates of any other parameters. As shown in section A of Appendix III, the gate and drain current amplitudes are equal at the frequency given by equation (IV.1)

$$\omega_0 = \frac{2\mu V_D}{\sqrt{3} \times L^2}, \quad (\text{IV.1})$$

where ω_0 is radial frequency, μ is hole mobility, V_D is drain voltage, and L is channel length. We have shown that this measurement technique yields a mobility of $2.3 \pm 0.4 \text{ cm}^2\text{V}^{-1}\text{s}^{-1}$ for the OECT used in Figure IV-2 and a mobility of $3.18 \pm 0.6 \text{ cm}^2\text{V}^{-1}\text{s}^{-1}$ for the OECT used in Figure IV-3. These values agree with the mobilities from the time-domain measurements and are within the experimentally reported values for PEDOT:PSS-based OECTs.^{28,174}

3. Limitations of the discrete model

The discrete model accurately describes transient behavior for a variety of input waveforms and biases, but it fails to take into account several non-idealities that affect OECTs. For example, previous chapters have shown that the ideal FET model is only valid over a limited voltage range because of the effects of disorder on charge transport in organic semiconductors. Because the long-channel FET model is only valid for a limited range of voltages, the discrete model works best for small-signal excitations of less than 100 mV. This will not decrease the utility of the discrete model for biosensing because many biosensing applications involve measuring small excitations on the order of millivolts. For instance, action potentials only produce an ~ 100 mV signal, which may be attenuated by tissue before reaching the OECT.^{159,176,177} Another complication for OECTs is the presence of current drift even after $t \gg \tau_{RC}$. This effect is noticeable in our devices, but only after $t > 10\tau_{RC}$ (~ 3 ms) and with an amplitude of less than 500 nA (see Figure IX-3 in Appendix III), so it has a limited effect on transient measurements. This long-time-scale drift could be due to a number of processes, such as conformational changes in the polymer matrix,⁸⁰ concentration-dependent ionic mobility,^{85,98} gradual redox processes due to dissolved hydrogen and oxygen in the electrolyte,^{178–180} or oxidation of chromium after it diffuses from under the source and drain electrodes.¹⁰¹ These processes might also cause asymmetric turn-on and turn-off speeds, especially for large voltage

steps. Designing OECTs with thick channels ($h \approx 2\sqrt{D\tau_{RC}} \approx 1.8 \mu\text{m}$, where D is the ionic diffusion coefficient) will add further complications because diffusion of the ions into the channel will be slower than polarization of the electrolyte and ion drift in the electrolyte.^{181,182} Although the discrete model overlooks these complexities inherent in OECTs, it is accurate for transient measurements in the small-signal regime, and one can adapt the model to describe non-idealities. For instance, non-uniform hole mobility can be accounted for by adding a disorder parameter to the steady-state equations used in the long-channel FET model (see chapter II), and certain non-ideal transient behavior can be described by allowing the capacitances to be dependent on voltage.¹²⁴ The discrete model strikes a balance between simplicity and accuracy, and, as shown in the next section, the model can be made more accurate at the expense of increased complexity.

4. Extending the discrete model – non-monotonic transconductance

As discussed above, the simplicity of the discrete model make it useful for predicting OECT output currents and extracting device and material parameters. However, in the previous section, we noted that the discrete model is only accurate over a limited voltage window. Therefore, in this section, we extend the discrete model by using the disorder model (chapter III) to describe the OECT channel while continuing to use the same RC circuit to describe the ionic current. We also continue to use the Meyer partition and the quasi-static approximation. Figure IV-5e,f shows the different predictions for the OECT transient response using the disorder model (Figure IV-5e) and the long-channel PMOS model (Figure IV-5f) to describe the OECT channel. Notice that both models provide accurate predictions for the current response when the gate voltage steps from 0 V to 125 mV. However, the long-channel PMOS model fails as the gate voltage step becomes larger. This failure occurs because the long-channel PMOS model cannot

accurately describe the conductivity of a disordered semiconductor over a large range of carrier concentrations. On the other hand, the disorder model accounts for changes in hole mobility as hole concentration increases. Therefore, it is accurate over a wide range of carrier concentrations and consequently a wide range of input voltages.

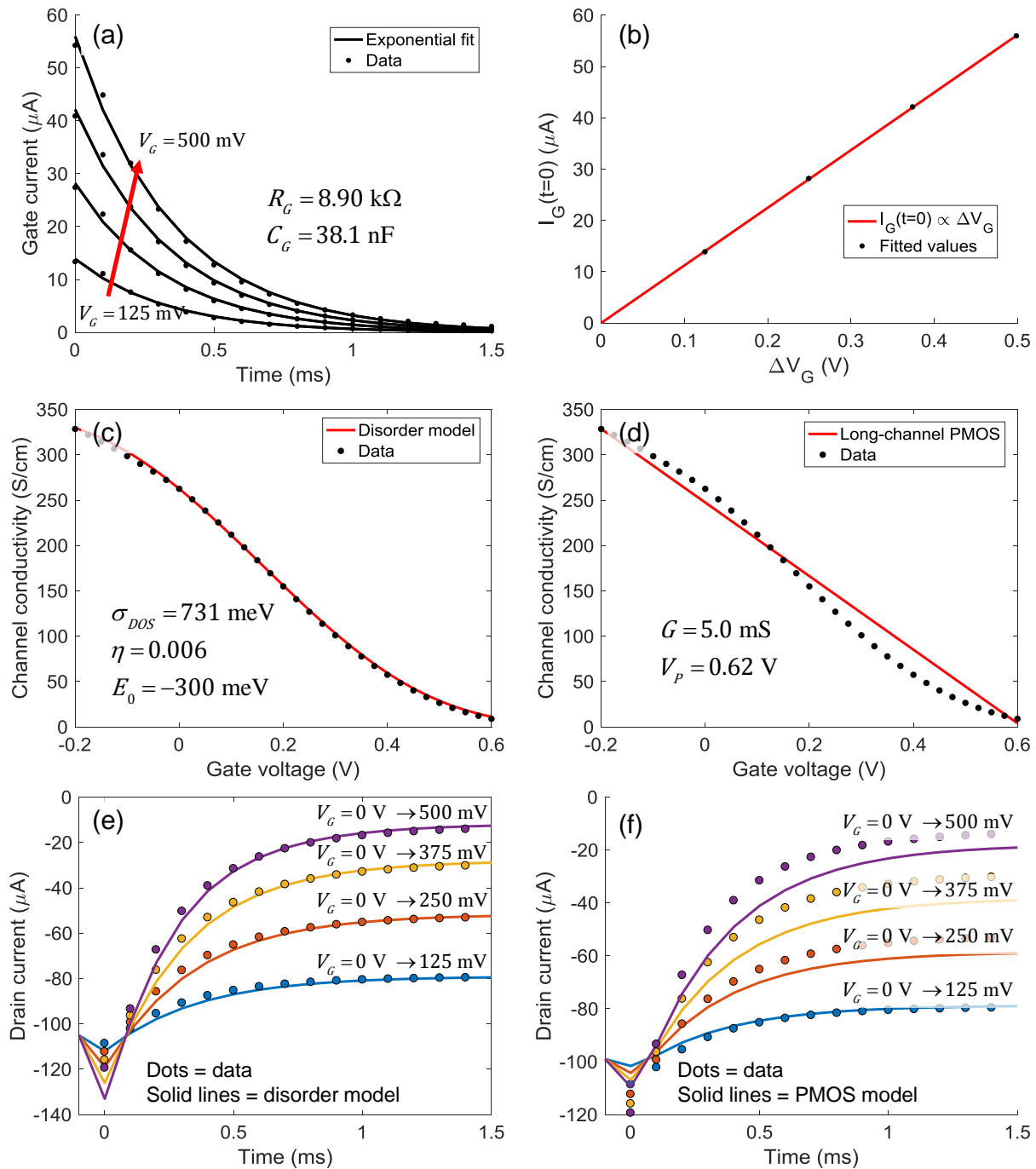


Figure IV-5. Extending the discrete model by incorporating the disorder model. Panel (a) shows an exponential fit to the gate current response to a gate voltage step. Each curve is for a different magnitude of the gate voltage step. In each step the gate voltage was stepped from 0 V to V_G . The values of V_G for each curve in the figure are 125 mV, 250 mV, 375 mV, and 500 mV, as indicated in the figure. Panel (b) shows the magnitude of the exponential fits as a function of the magnitude of the voltage step. Panel (c) shows the disorder model fit to the experimental transfer curve, and panel (d) shows the fit with the long-channel PMOS model. Panels (e) and (f) show the drain current response to the same gate voltage steps that were used for panel (a). In panels

(e) and (f), the dots are measured data, and the solid lines are the model fits. Each different color represents a different gate voltage step, as indicated in the panels. The device used for this figure was a PEDOT:PSS OECT with width, length, and thickness of $W = 40 \mu\text{m}$; $L = 40 \mu\text{m}$; $h \approx 200 \text{ nm}$ in 100 mM NaCl gated with a $2.5 \text{ mm} \times 2.5 \text{ mm}$ Ag/AgCl pellet.

As shown in Figure IV-5, we compared the long-channel PMOS approximation to the disorder model by making a series of measurements in which we stepped the gate voltage from 0 V to a higher voltage at time $t = 0$. Because the gate current is equal to the ionic current in the OECT, we used the gate current to extract the ionic R_G and C_{CH} values via an exponential fit (see equation (IX.8) in Appendix III). Figure IV-5a shows these exponential fits to the gate current, and Figure IV-5b shows that the gate current at $t = 0$ is directly proportional to the size of the gate voltage step, as expected. Once we extracted the parameters for the ionic current, we used steady-state measurements to extract parameters for describing the OECT channel's electronic conductivity. In Figure IV-5c and Figure IV-5d, we show the best fit to the steady-state data using the disorder model and the long-channel PMOS model, respectively. As discussed in chapters II and III, the disorder model accurately describes the curvature of the OECT transfer curve; whereas the long-channel PMOS model predicts a linear response to the gate voltage. Therefore, as shown in Figure IV-5f, the long-channel PMOS model is only accurate for a small portion of the transfer curve.

Overall, the disorder model is certainly more accurate than the long-channel PMOS model, but it is also more complicated. Because it is numerical, it cannot be easily implemented in SPICE, and it requires more computation time. Most importantly, it cannot be easily inverted, so it is less useful for calculating unknown input signals. Therefore, researchers should consider whether their application requires accuracy over a wide range of input voltages or an analytical model that can be easily inverted. In the former case, they should incorporate the disorder model

into the discrete model, as described in this section. In the latter case, they should use the discrete model with the long-channel PMOS approximation.

5. Extracting the input signal

So far in this chapter, we have shown that given a known input signal, the discrete model can predict an OECT's output current and provide estimates for device and material parameters. In this section, we show that the discrete model can also be inverted and used to extract an unknown input signal from a measured output signal. Inverting the discrete model is useful in biosensing applications when the input signal is not known. For instance, researchers use OECTs in ECoG arrays and directly measure the current response of the OECT. However, the signal of interest is actually a voltage perturbation, ΔV_G , caused by a local field potential or a neuron action potential, and it is not known a priori. Based on the OECT's current response, one can infer the input voltage signal and learn about the brain being tested. For instance, given the current response shown in Figure IV-6a, one could infer that the input voltage had a lorentzian-like shape. However, without a quantitative model, one might assume that the voltage signal is simply given by a proportionality, $\Delta V_G = \alpha \times \Delta I_D$. Such an assumption does not take into account the finite response speed of the OECT and results in the naïve reconstruction shown in blue in Figure IV-6b. Clearly a simple inference about the voltage input does not accurately represent the relative time delay between the input signal and the OECT response. Furthermore, the finite response speed of the OECT distorts the shape of the input signal. This effect is evident in Figure IV-6a, which shows that the current response is asymmetric about the peak of the spike; whereas, the original signal, shown in Figure IV-6b is symmetric about the peak. The naïve $\Delta V_G = \alpha \times \Delta I_D$ signal reconstruction preserves the asymmetric artifact from the current

response, but the signal reconstructed with the discrete model reproduces the symmetry of the original signal, as shown in Figure IV-6b.

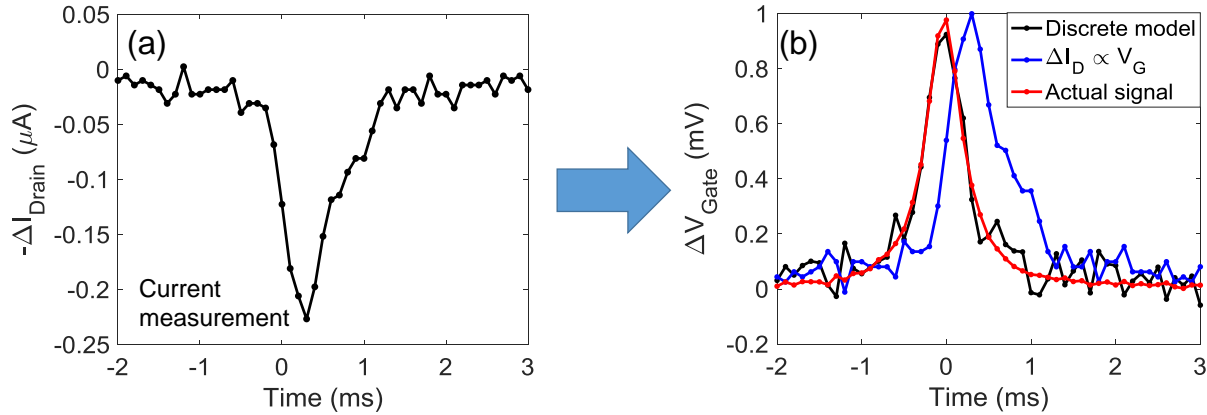


Figure IV-6. Measured current response (a) and extracted voltage input for an OECT (b). In panel (b), the reconstructed signals are calculated without any a priori information about the input voltage. In panel (b), the black curve is the signal reconstructed with the discrete model, the blue curve is the signal reconstructed assuming $\Delta I_D = \alpha \times \Delta V_G$, and the red curve is the measured signal. Although we did not use the measured voltage signal to calculate the reconstructed signal, we plot it in panel (b) for comparison to the reconstructions.

The reconstructions in Figure IV-6b were obtained by using the transfer function,

$H(\omega) = \frac{I_D(\omega)}{V_G(\omega)}$, from the discrete model (where ω is the radial frequency). Because this transfer

function can be inverted, we have a straightforward method to extract input voltage from a measured output current. First, calibrate the OECT by measuring the frequency response to extract the device parameters R_G , C_{CH} , and μ . Next, use these device parameters to calculate the OECT transfer function, $H(\omega)$, given by the discrete model.* Then multiply the Fourier transform of the measured current by the reciprocal of the transfer function, $V_G(\omega) = I_D(\omega) \times \frac{1}{H(\omega)}$, where $I_D(\omega) \equiv F(i_D(t))$. Finally, apply the inverse Fourier transform to obtain the input voltage, $v_G(t) = F^{-1}(V_G(\omega))$.

* The transfer function for the discrete model is given by equation (IX.13) in section A of Appendix III.

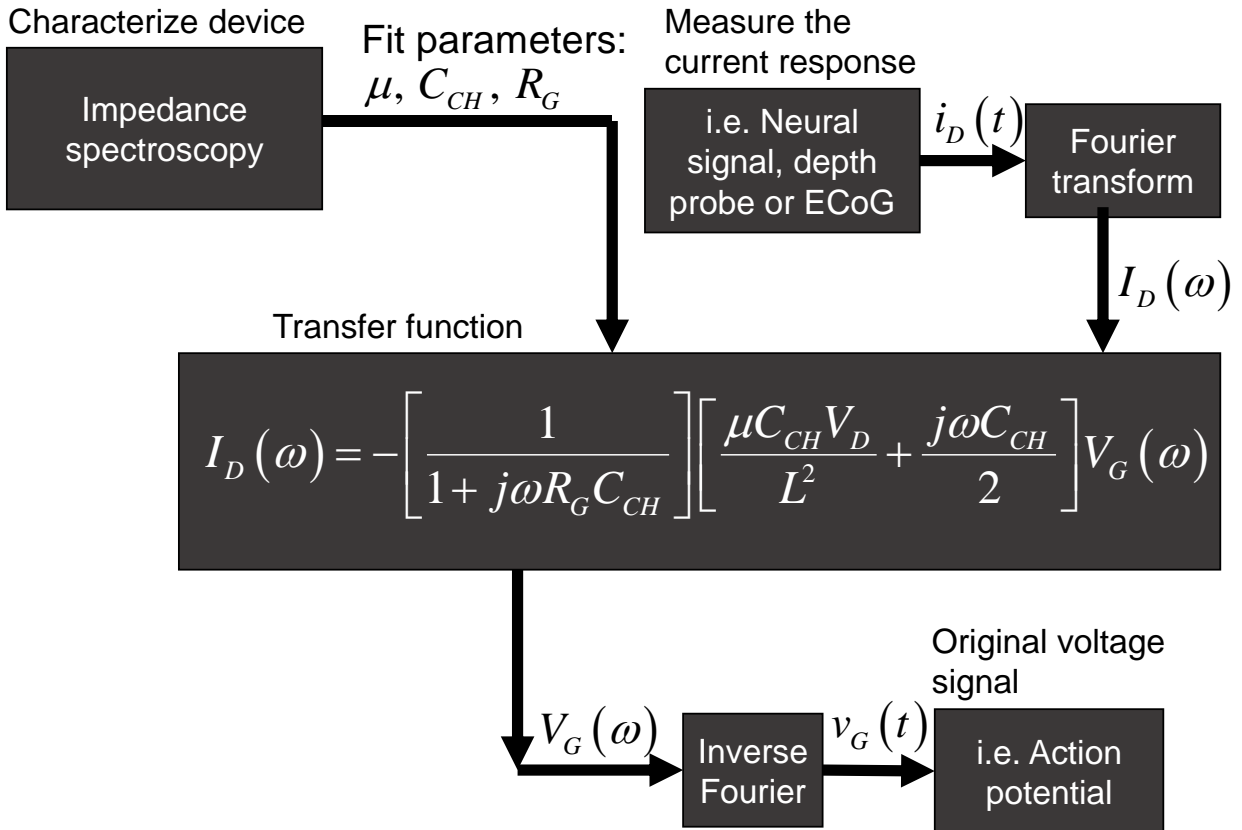


Figure IV-7. Block diagram describing the method for using the discrete model to extract an unknown voltage signal from a measured current response.

E. Conclusion

In this chapter, we showed that when OEETs are biased at a constant drain voltage of $V_D = V_{step}$, they respond more than 30 times faster than the speed of the ionic charging circuit. We demonstrated that these high-speed transistors responded to a step input voltage with a step output current, settling to within 10% of the steady-state current in only 20 μ s

. We also developed a simple discrete model that described this high-speed behavior and can be used to predict the current response following an arbitrary gate input. This simple model uses only three fit parameters and can be implemented in circuit simulation software or described with closed-form expressions, so it will be useful for a wide range of OEET applications.

Additionally, we show that the disorder model from chapter III can be used to describe channel conductivity in the discrete model for transient behavior. Using the disorder model improves the discrete model's accuracy and widens the range of input voltages for which it is valid. Overall, our work reveals that the shape and speed of the OECT transient response depends strongly on the applied drain bias, and that at the right bias, the current response can reach its steady-state value almost instantaneously.

CHAPTER V FUTURE WORK

Although OECTs are promising for biosensing, neuromorphic, and logic applications, many important questions about OECT behavior remain unanswered. In this chapter, we discuss several studies which could improve understanding of OECT behavior and therefore inform the development of better materials and device design for optimal operation in new and existing applications. In particular, we discuss the sub-threshold voltage swing in OECTs, OECT-based implementations of neuromorphic circuits, and the environmental stability of OECTs.

A. Sub-threshold voltage swing

The voltage swing of a transistor is defined as the change in gate voltage required to increase the channel current by a factor of ten. Voltage swing, S , is expressed in units of millivolts/decade of drain current. The value of S in the sub-threshold bias regime is a key figure of merit for low-power electronics; when S is minimal, the transistor can switch ON at a low voltage and has a very low OFF-state channel current. In MOSFETs, S is bounded by a theoretical lower limit of 60 mV/dec at room temperature,^{13,183} but this limit might not apply to OECTs. If OECTs can operate with $S < 60$ mV/dec, then they will be able to outperform conventional transistors in lower-power applications. Therefore, future research should explore whether OECTs are limited by the 60 mV/dec figure.

Using the model described in chapter III, we can predict S for a typical OECT. Figure V-1 shows the sub-threshold swing of a typical OECT assuming different widths of the Gaussian density of states (DOS) for the polymer semiconductor. We find that regardless of the DOS width, S asymptotes to a minimum of 60 mV/dec. Interestingly, this behavior is not expected for a MOSFET with a narrow DOS. According to K.P. Cheung, a MOSFET with a narrow DOS could have $S < 60$ mV/dec.¹⁸³ Cheung pointed out that the 60 mV/dec limit is only valid for

materials with a partially filled band described by a monotonically increasing DOS. For materials with a narrow partially filled band, the DOS may begin to decrease as charge carrier energy increases. Convolving this decreasing DOS with Fermi-Dirac statistics leads to a faster than exponential decrease in carrier concentration as a function of energy above the Fermi level. This leads to an OFF-state diffusion current that decreases faster than 60 mV/dec as a function of gate voltage.

One might expect the same reasoning to apply to OECTs, but the model described in chapter III does not predict $S < 60$ mV/dec even when the DOS width, σ , is less than the thermal energy. Furthermore, the lowest experimental sub-threshold swing reported for an OECT is 60 mV/dec.¹⁰ One can understand this behavior by recognizing that the voltage swing is the ratio of drain current to transconductance as shown below:

$$S \equiv \frac{\Delta V_G}{\Delta \log_{10}(I_D)} = \left[\frac{d \log_{10}(I_D)}{d V_G} \right]^{-1} = \log(10) I_D \left[\frac{d I_D}{d V_G} \right]^{-1} \equiv \log(10) \frac{I_D}{g_m}, \quad (\text{V.1})$$

where V_G is the gate voltage, I_D is the drain current, and g_m is the transconductance. Figure V-1 shows how drain current and transconductance depend on gate voltage. For a narrow DOS, the drain current decreases super-exponentially with gate voltage. However, transconductance also decreases at a super-exponential rate, as shown in Figure V-1b. Therefore, the ratio of drain current to transconductance does not necessarily decrease at a super-exponential rate. This reasoning suggests that OECTs are subject to a lower limit on S , but future work should put these ideas on more solid theoretical footing. Future work should also explore what material or device engineering would make it possible for OECTs to overcome the 60 mV/dec limit.

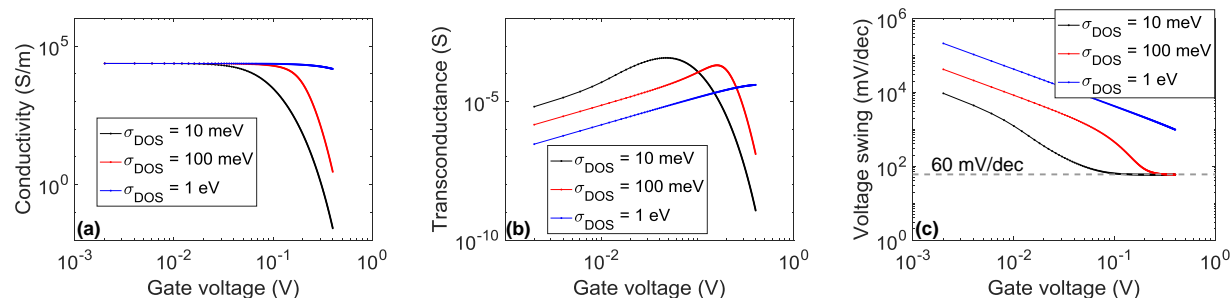


Figure V-1. Conductivity, transconductance, and voltage swing predicted by the disorder model introduced in chapter III. The simulation was executed assuming an OECT with length, width, and thickness of $L = 178 \mu\text{m}$, $W = 200 \mu\text{m}$, and $h \approx 100 \text{ nm}$, respectively. The percolation fraction used for these calculations was $\eta = 0.01$, and the conductivity at a gate voltage of 0 V was 236 S/cm.

B. OECT-based neuromorphic devices

In the past several years, many examples of OECT-based neuromorphic circuits and devices have been reported. In these examples, OECTs are operated so that they mimic the behavior of biological neurons. For instance, OECTs can exhibit memory capabilities,^{74,80,81} spike-timing-dependent plasticity,^{74,75,79,81} and soft connections between OECTs sharing a common electrolyte.⁸² The primary motivation for developing these neuromorphic circuits is the hypothesis that brain-like computation can perform certain tasks, such as image classification, as fast and accurately as conventional Von-Neumann-based computing systems but require substantially less power and physical volume than conventional systems.^{73,184}

Yoeri van de Burgt et al. recently reported an OECT-based Electrochemical Neuromorphic Organic Device (ENODE) as a hardware implementation of a synapse in neuromorphic circuits.⁸¹ This device, described in Figure V-2 has the same structure and function as an OECT. The only differences between the ENODE and an OECT are that the ENODE is operated differently and that a reducing agent, poly(ethyleneimine) (PEI), is blended with PEDOT:PSS in the device channel. This reducing agent counteracts the environmental oxidation of PEDOT and allows the device to maintain a programmable, non-volatile, open-

circuit potential even in the presence of water and oxygen. To show the similarity between ENODEs and OECTs and to demonstrate the importance of PEI, we fabricated a PEDOT:PSS-based ENODE using the exact same device structure and materials as an OECT without PEI. Figure V-3 shows the operation of this device, which, like an ENODE, displays low-voltage operation and a large number of stable conductance states. However, unlike PEI-based ENODEs, this device has a state-retention time of ~ 100 s in the open circuit configuration; whereas, ENODEs with PEI can retain an open-circuit conductance state for at least several days.⁸¹

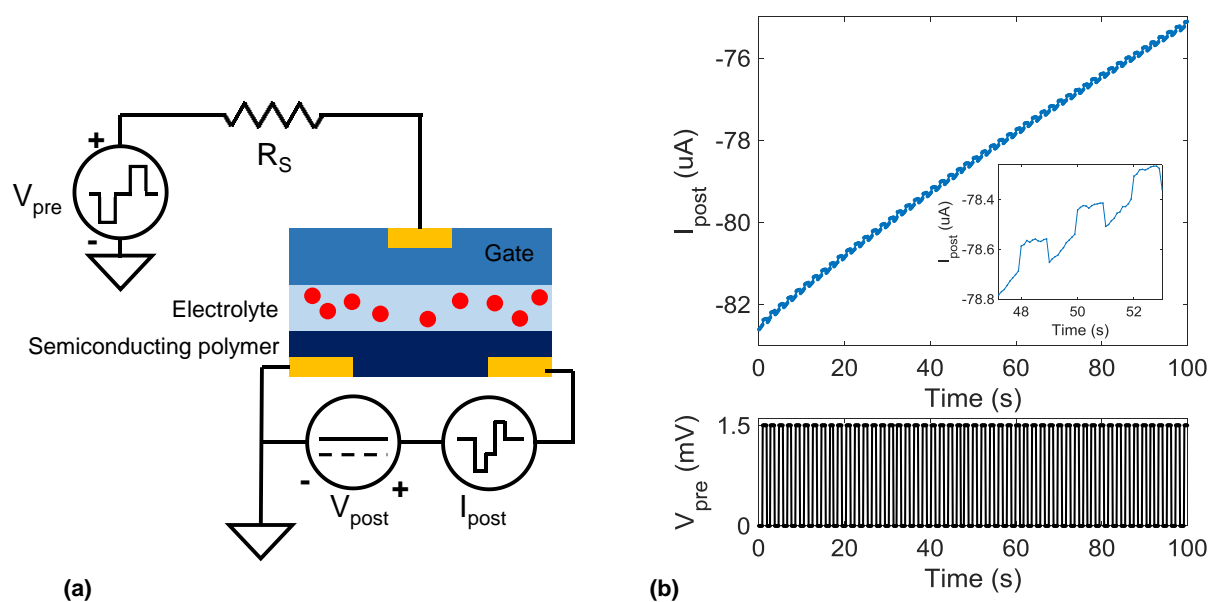


Figure V-2. ENODE layout (a) and typical pre-synaptic and post-synaptic time series (b). The inset in panel (b) is an enlarged view of the post-synaptic current between 47 s and 53 s. Data in (b) are from Van de Burgt et al.⁸¹

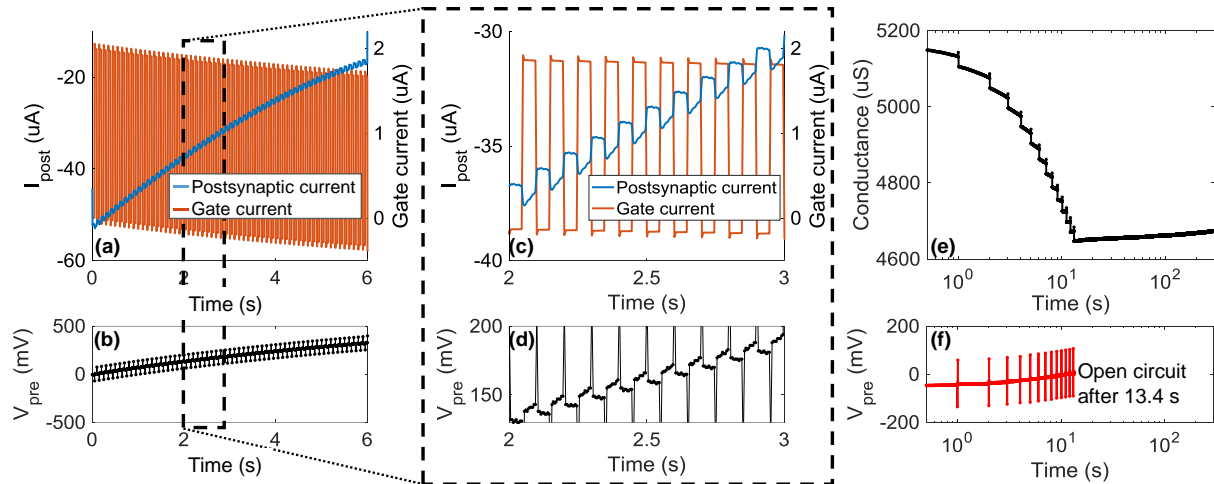


Figure V-3. Presynaptic voltage and postsynaptic current for a PEDOT:PSS-based ENODE (a)-(d). Panels (c) and (d) are magnified views of the response between 2 and 3 s. Panels (e) and (f) show the programmable conductance states and open-circuit retention of the same PEDOT:PSS-based ENODE. All data were collected with a $1\text{ M}\Omega$ resistor between the gate input and the ENODE itself. The reported presynaptic voltages are the voltages across the ENODE itself, after subtracting the voltage dropped over the input resistor. The ENODE has channel length, width, and thickness of $L = 1280\text{ }\mu\text{m}$; $W = 1280\text{ }\mu\text{m}$; $h \approx 200\text{ nm}$, respectively. The applied drain voltage is $V_{\text{Drain}} = -10\text{ mV}$.

Because ENODEs operate according to the same principles as OECTs, one can model them with the same SPICE circuit described in chapter IV. Figure V-4 shows the output of a SPICE simulation representing an ENODE with typical device and material characteristics. Notice that the ENODE channel can be modeled in exactly the same way as an OECT channel because environmental oxidation was neglected in the model proposed in chapter IV. However, the input node of an ENODE requires special consideration. Figure V-4 shows three different possible input configurations and their output behavior. Figure V-4a shows an ENODE with a series resistor between the voltage input and the ENODE itself. This is the input configuration used by Van de Burgt et al. The input resistor has two principle purposes. First, if its resistance is much larger than the electrolyte resistance, it transforms a voltage source into a current source at the input. Secondly, it increases the charging time constant of the ionic circuit between the input and the ENODE channel. This slows down both the programming and the discharging of the ENODE channel, thus allowing it to be biased into a metastable conductance state. The

disadvantage of the input resistor is that a large amount of voltage can be dropped across it. For instance, in the work of Van de Burgt et al. an input voltage of 1 V was applied even though only 1.5 mV of this was dropped across the ENODE itself. Also, even though the input resistor slows the discharge time of the ENODE, it does not eliminate discharge completely. Therefore, only a metastable state, rather than a truly non-volatile state, can be stored. Figure V-4b and Figure V-4c show a current source as the ENODE input and a switch-regulated voltage source at the input, respectively. These are both possible alternatives to the input resistor. They produce similar dynamic responses compared to the ENODE with an input resistor, but they allow for non-volatile conductance states. Additionally, the ENODE with the switch-regulated voltage source requires a lower applied voltage. Although the current source and the switch-regulated voltage source represent promising hypothetical inputs for ENODEs, further work is necessary to determine appropriate hardware implementations of these inputs. This work should focus on optimizing the ENODE input for minimal power consumption, spatial footprint, and drive voltage while maximizing switching speed and state retention.

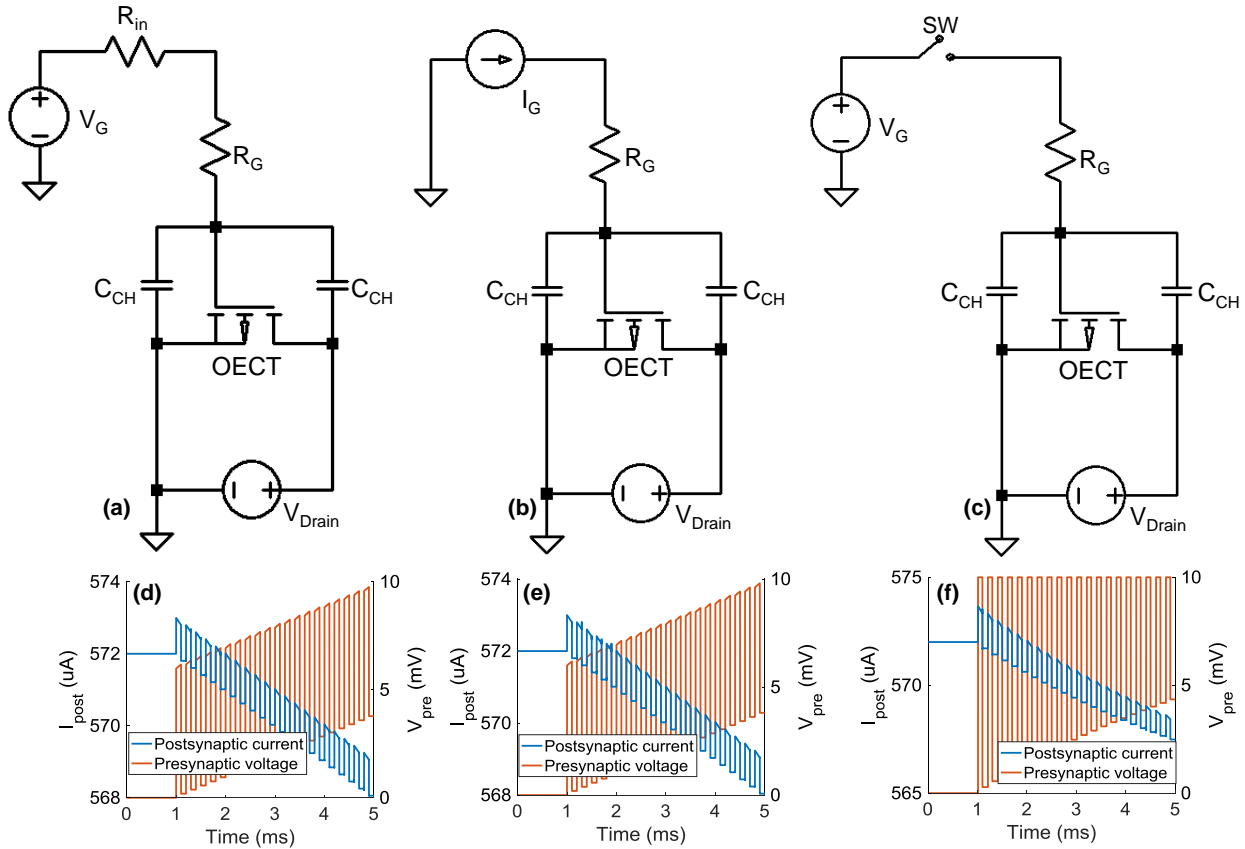


Figure V-4. Circuit diagrams (a)-(c) and input-output characteristics (d)-(f) of SPICE models for ENODEs. The diagrams in (a), (b), and (c) represent ENODEs with an input resistor, current source input, and switch-regulated voltage source input, respectively. The data shown in (d) are simulation results for the ENODE in (a) with 2 V square pulses at V_G . The data shown in (e) are simulation results for the ENODE in (b) with 2 μA square pulses at I_G . The data shown in (f) are simulation results for the ENODE in (c) with 10 mV square voltage pulses at V_G . In (d)-(f), the presynaptic voltage is the voltage at the end of R_G nearest the input and is equal to the total voltage dropped across the ENODE itself. For these simulations, we have assumed that the capacitance at the gate is large enough that it has a negligible effect on the circuit. In (d)-(f), the channel mobility is $\mu = 1 \text{ cm}^2 \text{ V}^{-1} \text{ s}^{-1}$; the channel capacitance is $c^* = 80 \text{ F cm}^{-3}$; the pinch-off voltage is $V_p = 0.6 \text{ V}$; the gate-channel resistance is $R_G = 3 \text{ k}\Omega$; the channel length, width, and thickness are $L = 100 \text{ }\mu\text{m}$, $W = 260 \text{ }\mu\text{m}$, $h = 500 \text{ nm}$, respectively; and the drain voltage is $V_{Drain} = -100 \text{ mV}$.

In addition to optimizing input devices, future work on ENODE development could focus on low-power operation. Van de Burgt et al. projected that with current lithography technology one could make an ENODE that requires only 35 aJ per switching event. However, Van de Burgt et al.'s smallest actual devices were 1000 μm^2 and required 10 pJ per switching event.

According to Kuzum et al. the human brain uses about 10 fJ of energy per synaptic event,

providing a reasonable benchmark for neuromorphic devices.⁷³ While scaling arguments suggest that this benchmark is within reach, future researchers must show that it can be achieved in practice. Many possible setbacks could limit the scaling of ENODEs. For instance, according to Sessolo et al., decreasing OECT area causes a proportional decrease in the signal-to-noise ratio.¹⁸⁵ Other possible difficulties include parasitic losses due to channel/electrode overlap and increased device-to-device variation at the limits of lithographic resolution. Studying and circumventing these difficulties should be a priority for researchers hoping to use ENODEs as low-power synaptic devices.

ENODE research could also work toward the integration of multiple ENODEs into a larger computation circuit. For instance, Van de Burgt et al. simulated a network of ~ 23000 ENODEs and showed that if each device behaved according to the experimental performance of a single ENODE, then the circuit could recognize 8×8 pixel representations of handwritten digits with $> 90\%$ accuracy. Demonstration of a physical circuit with this scale of integration would be an enormous challenge and a significant step forward for the field. Another form of integration would involve only a single ENODE synapse but multiple gate inputs. As noted by Gkoupidenis et al., such a circuit could perform coincidence detection and recognize spatial orientation.^{82,186} One problem in multi-gate ENODE circuits is cross-talk between gates. One can predict the degree of cross-talk between gates using the SPICE model shown in Figure V-5, which has a single ENODE and three gates with switch-regulated voltage sources. This model can represent the case where the gates and channel all share the same electrolyte, as shown in Figure V-5a, or the case where a patterned electrolyte prevents the gates from being directly connected to each other, as shown in Figure V-5b. In the latter case, the gate cross-talk resistance, $R_{X,i-j}$, is substantially larger than in the shared electrolyte configuration. Figure V-6a

shows the time domain response of a multi-gate ENODE in the shared electrolyte configuration. The black line in Figure V-6a shows the response when only one gate is connected to the ENODE while the switches are insulating at the other two gate inputs. Similarly, the red line and the blue line show the response when two and three gates are connected, respectively. Figure V-6b shows the responses in the case of a patterned electrolyte. From the different responses to one, two, and three connected gates, one can deduce the linearity of the multi-gate ENODE. For a perfectly linear response, the change in postsynaptic current would be directly proportional to the number of active gates. Figure V-6c shows that the ENODE with a patterned electrolyte has a more linear response than the ENODE with a shared electrolyte, but it is still not perfectly linear. This nonlinearity occurs because even if $R_{X,i-j}$ is infinite, some current can feed back between the separate gate electrodes by flowing through the gate-channel resistor, $R_{G,i}$, to the channel, and then back through another gate-channel resistor, $R_{G,j}$.

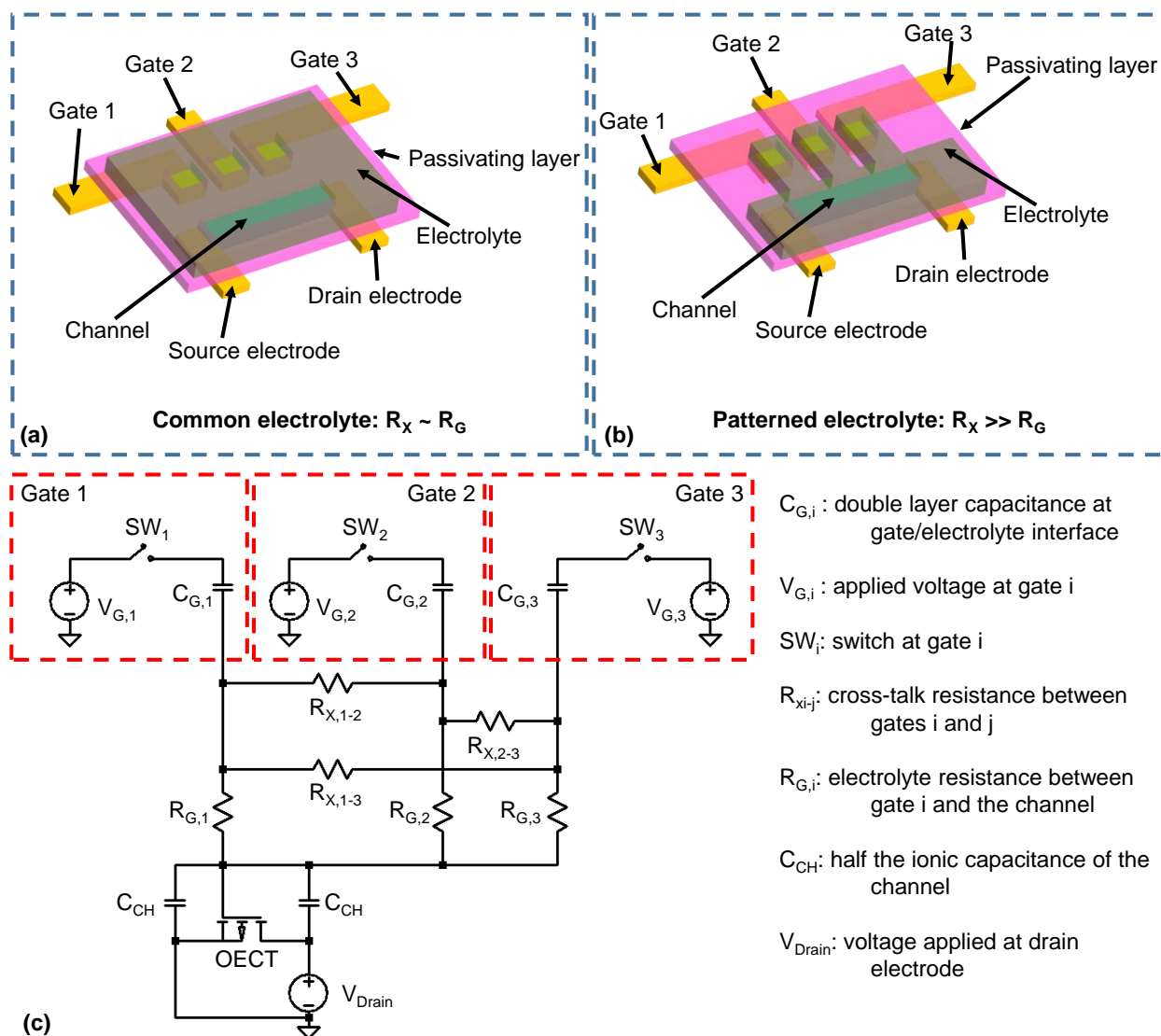


Figure V-5. Physical layout (a) and (b) and SPICE circuit (c) representing the ENODE with multiple gate inputs. Panel (a) shows the layout for an ENODE with a shared electrolyte for all gates. Panel (b) shows the layout for an ENODE with a patterned electrolyte.

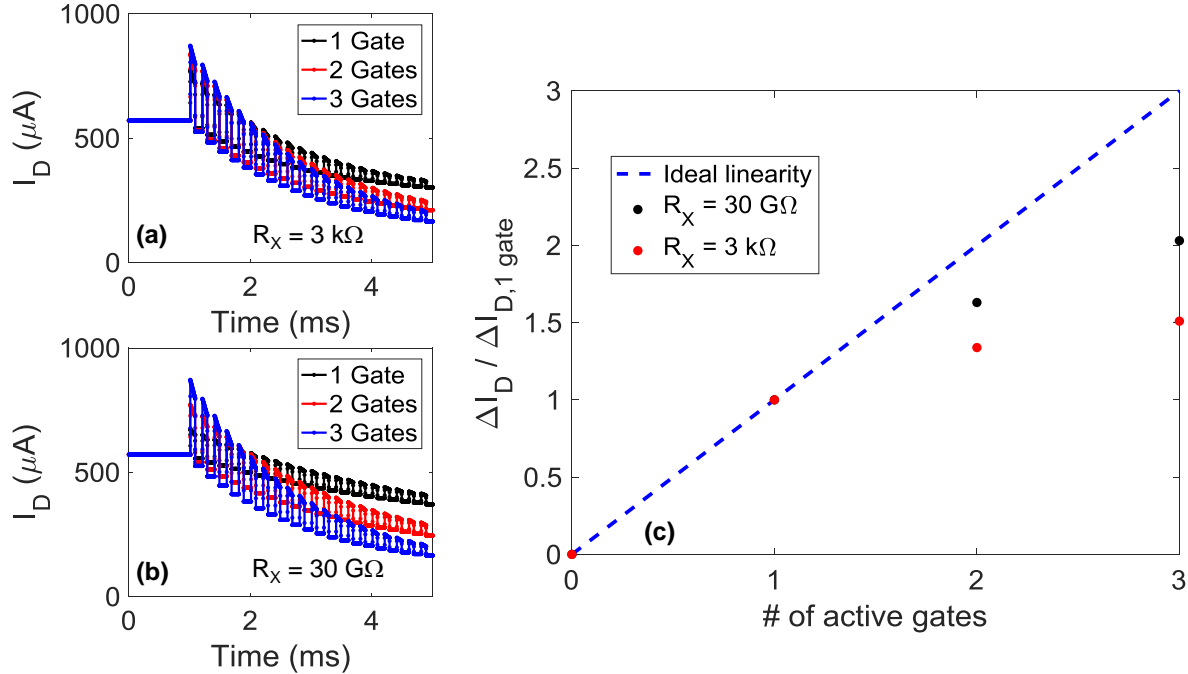


Figure V-6. Time-domain response of an ENODE to one, two, and three connected gates for a cross-talk resistance of $R_{X,i-j} = 3 \text{ k}\Omega$ (a) and $R_{X,i-j} = 30 \text{ G}\Omega$ (b) in the configuration shown in Figure V-5. The input voltages at each gate are square pulses with a base voltage of 0 V and a peak voltage of 0.6 V. The duty cycle and period are 50% and 200 μs , respectively. For connected gates, the switches are conductive for $V_G > 0$ and insulating for $V_G \leq 0$. For disconnected gates the switches are always insulating. Panel (c) shows the change in drain current after 4 ms of gate pulses for 0, 1, 2, and 3 active gates. The dashed line shows the ideal linear response that would occur if n gates had n times the effect of 1 gate. The simulation parameters are $\mu = 1 \text{ cm}^2\text{V}^{-1}\text{s}^{-1}$; $c^* = 80 \text{ Fcm}^{-3}$; $V_P = 0.6 \text{ V}$; $R_{G,i} = 3 \text{ k}\Omega$ for all i ; $C_{G,i} = 1 \text{ }\mu\text{F}$ for all i ; the channel length, width, and thickness are $L = 100 \text{ }\mu\text{m}$, $W = 260 \text{ }\mu\text{m}$, $h = 500 \text{ nm}$, respectively; and the drain voltage is $V_{\text{Drain}} = -100 \text{ mV}$.

C. OECT stability

Most applications for OECTs require operational stability. However, OECTs suffer from many forms of instability, such as current drift under constant bias, current decay during ON-OFF cycling, unwanted redox peaks in cyclic voltammetry, degradation at elevated temperatures, and leakage current between the gate and channel. Strategies for overcoming one or more of these degradation mechanisms have been reported in the literature. For instance, including the silanated cross-linker 3-glycidoxypropyltrimethoxysilane in the PEDOT:PSS dispersion prevents swelling-induced delamination of the OECT channel, which is a common cause of degradation

during ON-OFF cycling.^{99,137} In this section, we will discuss three degradation effects that merit further study. These effects are the non-zero gate current at steady-state, the environmental oxidation of PEDOT, and the appearance of new redox peaks when operating OECTs at elevated temperatures.

An example of the steady-state gate current in OECTs is shown in Figure V-7a. This behavior is widely recognized, and several researchers have even added a parallel leakage path into OECT models to describe this current.^{30,187} The steady-state gate current causes several problems. For instance, it causes OFF-state power consumption, which could prevent OECTs from being used in low-power electronics or in ENODE-based neuromorphic applications where energy consumption is of primary importance. Also, gate-current leakage could cause the gradual decay of drain current even when gate and drain voltages are fixed. This behavior is shown in Figure V-7c, and, although it is rarely discussed in the literature, it is noticeable in many reports of OECT time-domain behavior.^{26,66,67,108,166} A characteristic of this behavior is that the drain current is not an exponential function of time after a gate voltage step. Rather, it fits better to a stretched exponential. At short time scales, the drain current seems to follow single-exponential behavior, as shown in the inset of Figure V-7c, but the drain current continues to decrease long after the initial exponential fit asymptotes to its steady-state value. One might expect that slow diffusion of ions in the electrolyte or into the semiconductor causes this gate leakage. However, this seems unlikely because the leakage persists long after characteristic diffusion times for ion drift/diffusion in PEDOT:PSS and similar materials.^{99,188,189} Another possible cause of the gate leakage is a Faradaic reaction occurring at the gate or source/drain electrodes of the OECT. Two possible Faradaic reactions are the hydrolysis of aqueous electrolytes and the oxidation of chromium. The latter could occur if chromium, which is often used as an adhesion promoter for

gold, diffused from the bottom of the gold layer at the source/drain electrodes to the top of the gold and then oxidized when exposed to the electrolyte.¹⁰¹ If chromium oxidation causes the gate leakage current, then using a more stable metal as an adhesion promoter could eliminate the steady-state current. A study showing whether this strategy works would inform the fabrication of more stable OEETs, and it would reveal whether cytotoxic heavy-metal ions leak from OEET electrodes into the cell media during biosensing experiments.

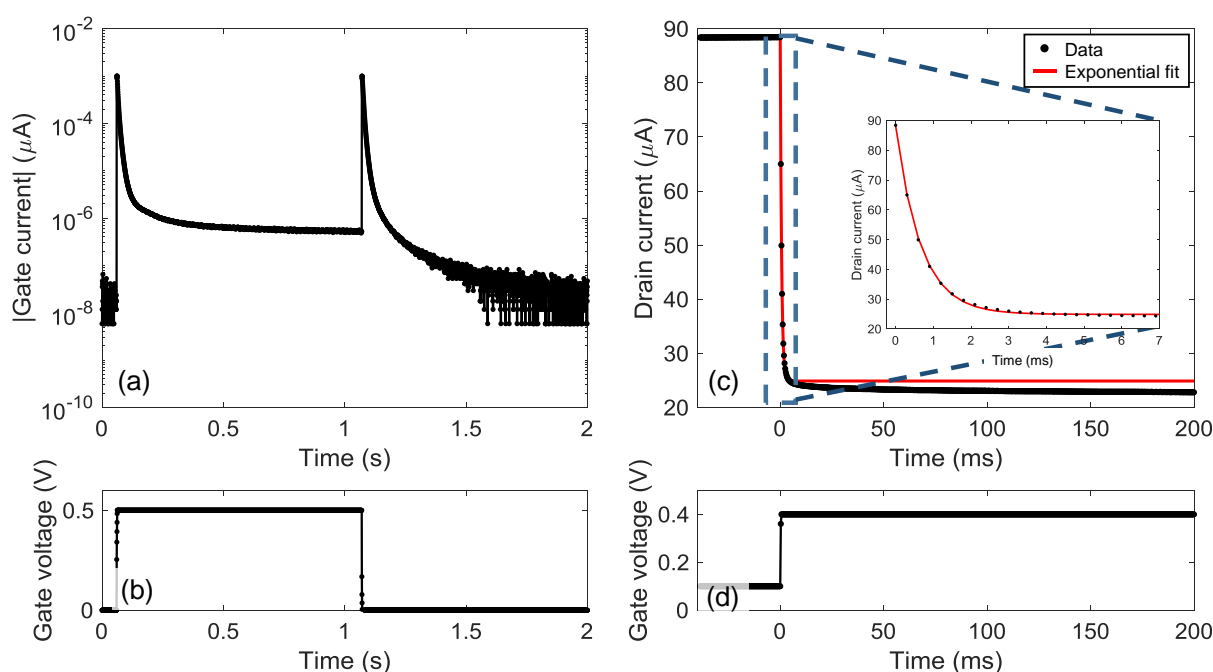


Figure V-7. Gate current (a) and drain current (c) of OEETs. Panels (b) and (d) show the corresponding gate voltages. The OEET in (a) has channel width and length of $1280 \mu\text{m}$. The OEET in (b) has channel width of $250 \mu\text{m}$ and length of $100 \mu\text{m}$. The inset in panel (c) shows an enlarged view of the drain current for 7 ms after the voltage step. The red line in panel (c) is an exponential fit to the first 7 ms after the gate voltage step. Notice in (a) that the gate current is at the noise level of the source-meter-unit when the gate voltage is zero, but the gate current is almost two orders of magnitude larger when the gate voltage is 0.5 V.

Another cause of PEDOT instability is environmental oxidation. Many reports show that the presence of oxygen and water causes PEDOT oxidation.^{81,180,190,191} This oxidation may reduce the ON/OFF ratio of OEETs due to less effective dedoping (reduction) of PEDOT at

positive gate voltage,¹⁸⁰ and it prevents OECTs from maintaining a fixed conductivity state when disconnected from the gate circuit. Because of the latter impact on OECT performance, ENODEs must include PEI to offset PEDOT oxidation, as discussed in section A. Unfortunately, the PEI included in ENODE channels is consumed during device operation and storage. Therefore, PEI consumption defines an upper bound on the lifetime of ENODEs. Research could be undertaken to determine the theoretical lifetime of an ENODE and how downscaling device size affects the lifetime. Additionally, developing an encapsulation scheme for ENODEs to prevent oxygen from reaching the PEDOT channel would eliminate the unwanted oxidation of PEDOT and the need for PEI.

Thermal stability is another matter of grave importance for OECTs. The effects of temperature on PEDOT have been thoroughly studied and reported in the literature. One important result is that PEDOT conductivity can have either a positive or negative correlation with temperature for lightly-doped or heavily-doped samples, respectively.¹⁹² However, at longer time scales (typically on the order of hours), even lightly-doped PEDOT shows a decrease in conductivity at elevated temperatures.¹⁹³ This behavior is poorly understood,¹⁹⁴ and has been attributed to many different mechanisms, including oxidation of sulfur on the thiophene ring,¹⁹⁵ decrease in polaron concentration,^{196,197} and shrinkage of conducting grains.¹⁹³ In most of these studies, degradation only occurs after many hours at temperatures greater than 140 °C, and many researchers using thermogravimetric analysis conclude that PEDOT:PSS is stable at temperatures below 200 °C.^{198–201} In our lab, we have not measured significant temperature-dependent conductivity decreases, but we have noticed the growth of redox peaks while making cyclic voltammetry measurements at elevated temperatures, as shown in Figure V-8. The heights of these redox peaks do not return to their original values after cooling the sample down (Figure

V-8b). This suggests that irreversible electrochemical changes occur in the OECT at temperatures as low as 50 °C. Future studies should be directed at determining the chemical species responsible for the redox peaks in Figure V-8 and learning if they are related to temperature-dependent conductivity degradation in OECTs.

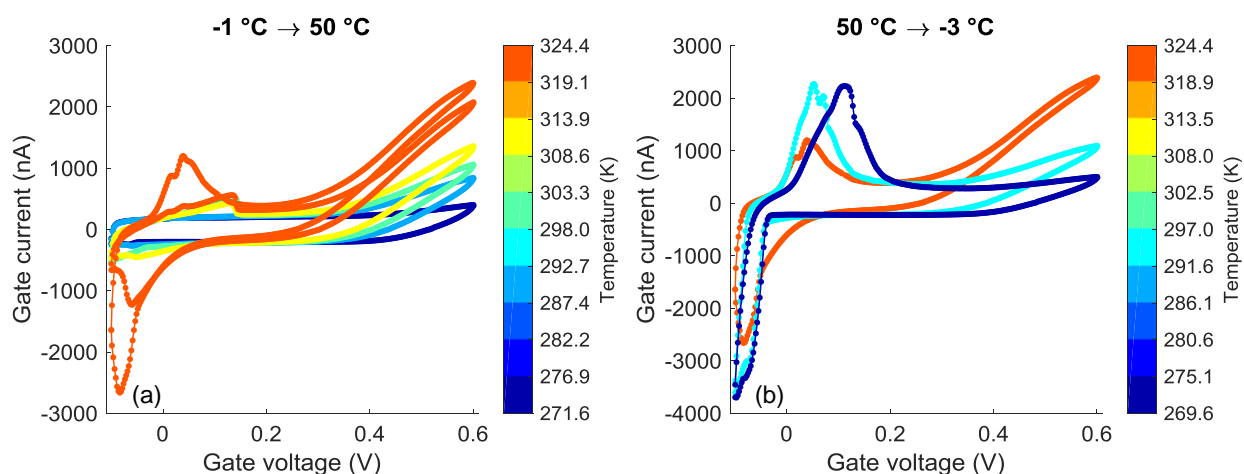


Figure V-8. Cyclic voltammograms of the gate circuit in an OECT. In panel (a), the temperature is increased monotonically from $-1\text{ }^{\circ}\text{C}$ to $50\text{ }^{\circ}\text{C}$. In panel (b), the temperature is decreased monotonically from $50\text{ }^{\circ}\text{C}$ to $-3\text{ }^{\circ}\text{C}$. The channel length, width, and thickness for this device are $L = 200\text{ }\mu\text{m}$, $W = 200\text{ }\mu\text{m}$, and $h \sim 100\text{ nm}$, respectively. The drain voltage was $V_{\text{Drain}} = -10\text{ mV}$.

In conclusion, OECTs show great promise in many applications, as discussed in previous chapters. However, ample research opportunities exist to improve our knowledge of OECT behavior. Investigating OECT subthreshold swing, operation in ENODEs, and device stability will inform optimization of OECTs for new applications and will improve the reliability of OECTs in well-established applications.

BIBLIOGRAPHY

1. White, H. S., Kittlesen, G. P. & Wrighton, M. S. Chemical derivatization of an array of three gold microelectrodes with polypyrrole: fabrication of a molecule-based transistor. *J. Am. Chem. Soc.* **106**, 5375–5377 (1984).
2. Groenendaal, B. L., Jonas, F., Freitag, D., Pielartzik, H. & Reynolds, J. R. Poly(3,4-ethylenedioxythiophene) and Its Derivatives : Past , Present , and Future. *Adv. Funct. Mater.* **12**, 481–494 (2000).
3. Kirchmeyer, S., Reuter, K. & Simpson, J. C. in *Handbook of Conducting Polymers: Conjugated Polymers Processing and Applications* (eds. Skotheim, T. A. & Reynolds, J. R.) (CRC Press: Taylor & Francis Group, 2007). doi:10.1002/marc.201100528
4. Jonas, F., Krafft, W. & Muys, B. Poly(3, 4-ethylenedioxythiophene): Conductive coatings, technical applications and properties. *Macromol. Symp.* **100**, 169–173 (1995).
5. Stöcker, T., Köhler, A. & Moos, R. Why does the electrical conductivity in PEDOT:PSS decrease with PSS content? A study combining thermoelectric measurements with impedance spectroscopy. *J. Polym. Sci. Part B Polym. Phys.* **50**, 976–983 (2012).
6. Lim, K. *et al.* The enhancement of electrical and optical properties of PEDOT:PSS using one-step dynamic etching for flexible application. *Org. Electron. physics, Mater. Appl.* **15**, 1849–1855 (2014).
7. Kaphle, V., Liu, S., Al-Shadeedi, A., Keum, C.-M. & Lüssem, B. Contact Resistance Effects in Highly Doped Organic Electrochemical Transistors. *Adv. Mater.* **28**, 8766–8770 (2016).
8. Inal, S. *et al.* A High Transconductance Accumulation Mode Electrochemical Transistor. *Adv. Mater.* **26**, 7450–7455 (2014).
9. Zeglio, E. *et al.* Conjugated Polyelectrolyte Blends for Electrochromic and Electrochemical Transistor Devices. *Chem. Mater.* **27**, 6385–6393 (2015).
10. Giovannitti, A. *et al.* Controlling the mode of operation of organic transistors through side-chain engineering. *Proc. Natl. Acad. Sci.* **113**, 12017–12022 (2016).
11. Nielsen, C. B. *et al.* Molecular Design of Semiconducting Polymers for High-Performance Organic Electrochemical Transistors Molecular Design of Semiconducting Polymers for High- Performance Organic Electrochemical Transistors. *J. Am. Chem. Soc.* (2016). doi:10.1021/jacs.6b05280
12. Giovannitti, A. *et al.* N-type organic electrochemical transistors with stability in water. *Nat. Commun.* **7**, 13066 (2016).
13. Sze, S. M. & Ng, K. K. in *Physics of Semiconductor Devices* 293–373 (John Wiley & Sons, Inc., 2007). doi:10.1002/9780470068328.ch6

14. Pickup, P. G. & Murray, R. W. Redox conduction in mixed-valent polymers. *J. Am. Chem. Soc.* **105**, 4510–4514 (1983).
15. Pickup, P. G. & Murray, R. W. Redox Conduction: Its Use in Electronic Devices. *J. Electrochem. Soc.* **131**, 833–839 (1984).
16. Chao, S. & Wrighton, M. S. Solid-state microelectrochemistry: electrical characteristics of a solid-state microelectrochemical transistor based on poly(3-methylthiophene). *J. Am. Chem. Soc.* **109**, 2197–2199 (1987).
17. Chao, S. & Wrighton, M. S. Characterization of a solid-state polyaniline-based transistor: water vapor dependent characteristics of a device employing a poly(vinyl alcohol)/phosphoric acid solid-state electrolyte. *J. Am. Chem. Soc.* **109**, 6627–6631 (1987).
18. Ofer, D., Park, L. Y., Schrock, R. R. & Wrighton, M. S. Potential dependence of the conductivity of polyacetylene: finite potential windows of high conductivity. *Chem. Mater.* **3**, 573–575 (1991).
19. Ofer, D., Crooks, R. M. & Wrighton, M. S. Potential dependence of the conductivity of highly oxidized polythiophenes, polypyrroles, and polyaniline: finite windows of high conductivity. *J. Am. Chem. Soc.* **112**, 7869–7879 (1990).
20. Matsue, T., Nishizawa, M., Sawaguchi, T. & Uchida, I. An enzyme switch sensitive to NADH. *J. Chem. Soc. Chem. Commun.* 1029–1031 (1991). doi:10.1039/C39910001029
21. Rani, V. & Santhanam, K. S. V. Polycarbazole-based electrochemical transistor. *J. Solid State Electrochem.* **2**, 99–101 (1998).
22. Nilsson, B. D. *et al.* Bi-stable and Dynamic Current Modulation in Electrochemical Organic Transistors. *Adv. Mater.* **14**, 51–54 (2002).
23. Zhu, Z.-T. *et al.* A simple poly(3,4-ethylene dioxythiophene)/poly(styrene sulfonic acid) transistor for glucose sensing at neutral pH. *Chem. Commun.* 1556–1557 (2004). doi:10.1039/B403327M
24. Robinson, N. D., Svensson, P.-O., Nilsson, D. & Berggren, M. On the Current Saturation Observed in Electrochemical Polymer Transistors. *J. Electrochem. Soc.* **153**, H39 (2006).
25. Lin, Y.-J. *et al.* Organic thin film transistor by using polymer electrolyte to modulate the conductivity of conjugated polymer. *Appl. Phys. Lett.* **89**, 223518 (2006).
26. Bernards, D. A. & Malliaras, G. G. Steady-State and Transient Behavior of Organic Electrochemical Transistors. *Adv. Funct. Mater.* **17**, 3538–3544 (2007).
27. Bernards, D. A. *et al.* Enzymatic sensing with organic electrochemical transistors. *J. Mater. Chem.* **18**, 116 (2008).

28. Rivnay, J. *et al.* High-performance transistors for bioelectronics through tuning of channel thickness. *Sci. Adv.* **1**, e1400251–e1400251 (2015).
29. Cho, S. W. *et al.* The characteristics and interfacial electronic structures of organic thin film transistor devices with ultrathin $(\text{HfO}_2)_x(\text{SiO}_2)_{1-x}$ gate dielectrics. *Appl. Phys. Lett.* **92**, 213302 (2008).
30. Khodagholy, D. *et al.* High transconductance organic electrochemical transistors. *Nat. Commun.* **4**, 2133 (2013).
31. McCoy, C. H. & Wrighton, M. S. Potential-dependent conductivity of conducting polymers yields opportunities for molecule-based devices - A microelectrochemical push-pull amplifier based on 2 different conducting polymer transistors. *Chem. Mater.* **5**, 914–916 (1993).
32. Horowitz, P. & Hill, W. in *The Art of Electronics* 91–92 (Cambridge University Press, 1989).
33. Nilsson, D., Robinson, N., Berggren, M. & Forchheimer, R. Electrochemical Logic Circuits. *Adv. Mater.* **17**, 353–358 (2005).
34. Mannerbro, R., Rånklöf, M., Robinson, N. & Forchheimer, R. Inkjet printed electrochemical organic electronics. *Synth. Met.* **158**, 556–560 (2008).
35. Hutter, P. C., Rothlander, T., Scheipl, G. & Stadlober, B. All Screen-Printed Logic Gates Based on Organic Electrochemical Transistors. *IEEE Trans. Electron Devices* **62**, 4231–4236 (2015).
36. Khodagholy, D. *et al.* High speed and high density organic electrochemical transistor arrays. *Appl. Phys. Lett.* **99**, 163304 (2011).
37. Friedlein, J. T., Donahue, M. J., Shaheen, S. E., Malliaras, G. G. & McLeod, R. R. Microsecond Response in Organic Electrochemical Transistors: Exceeding the Ionic Speed Limit. *Adv. Mater.* **28**, 8398 (2016).
38. Uno, M., Cha, B.-S., Kanaoka, Y. & Takeya, J. High-speed organic transistors with three-dimensional organic channels and organic rectifiers based on them operating above 20MHz. *Org. Electron.* **20**, 119–124 (2015).
39. Semiconductors, N. *BFU725F/N1: NPN wideband silicon germanium RF transistor.* (2011). at <http://www.mouser.com/ds/2/302/BFU725F_N1-1125964.pdf>
40. Ahn, J.-H. *et al.* High-speed mechanically flexible single-crystal silicon thin-film transistors on plastic substrates. *IEEE Electron Device Letters* **27**, 460–462 (2006).
41. Sun, Y. *et al.* Gigahertz operation in flexible transistors on plastic substrates. *Appl. Phys. Lett.* **88**, 183509 (2006).

42. Berggren, M. *et al.* Browsing the Real World using Organic Electronics, Si-Chips, and a Human Touch. *Adv. Mater.* 1–6 (2016). doi:10.1002/adma.201504301
43. Isaksson, J. *et al.* Electronic control of Ca²⁺ signalling in neuronal cells using an organic electronic ion pump. *Nat Mater* **6**, 673–679 (2007).
44. Ludwig, K. A., Uram, J. D., Yang, J., Martin, D. C. & Kipke, D. R. Chronic neural recordings using silicon microelectrode arrays electrochemically deposited with a poly(3,4-ethylenedioxythiophene) (PEDOT) film. *J. Neural Eng.* **3**, 59–70 (2006).
45. Richardson-Burns, S. M., Hendricks, J. L. & Martin, D. C. Electrochemical polymerization of conducting polymers in living neural tissue. *J. Neural Eng.* **4**, L6–L13 (2007).
46. Xiao, Y., Martin, D. C., Cui, X. & Shenai, M. Surface modification of neural probes with conducting polymer poly(hydroxymethylated-3,4-ethylenedioxythiophene) and its biocompatibility. *Appl. Biochem. Biotechnol.* **128**, 117–129 (2006).
47. Yang, J. *et al.* Ordered surfactant-templated poly(3,4-ethylenedioxythiophene) (PEDOT) conducting polymer on microfabricated neural probes. *Acta Biomater.* **1**, 125–136 (2005).
48. Oh, J. Y., Kim, S., Baik, H.-K. & Jeong, U. Conducting Polymer Dough for Deformable Electronics. *Adv. Mater.* **28**, 4455–4461 (2016).
49. Khodagholy, D. *et al.* Highly conformable conducting polymer electrodes for in vivo recordings. *Adv. Mater.* **23**, 268–272 (2011).
50. Svennersten, K., Larsson, K. C., Berggren, M. & Richter-Dahlfors, A. Organic bioelectronics in nanomedicine. *Biochim. Biophys. Acta - Gen. Subj.* **1810**, 276–285 (2011).
51. Strakosas, X., Bongo, M. & Owens, R. M. The organic electrochemical transistor for biological applications. *J. Appl. Polym. Sci.* **132**, 41735 (2015).
52. Venkatraman, S. *et al.* In vitro and in vivo evaluation of PEDOT microelectrodes for neural stimulation and recording. *IEEE Trans. Neural Syst. Rehabil. Eng.* **19**, 307–316 (2011).
53. Lin, P. & Yan, F. Organic Thin-Film Transistors for Chemical and Biological Sensing. *Adv. Mater.* **24**, 34–51 (2012).
54. Yang, S. Y. *et al.* Electrochemical transistors with ionic liquids for enzymatic sensing. *Chem. Commun.* **46**, 7972–7974 (2010).
55. Liao, C. *et al.* Highly selective and sensitive glucose sensors based on organic electrochemical transistors using TiO₂ nanotube arrays-based gate electrodes. *Sensors Actuators B Chem.* **208**, 457–463 (2015).

56. N. Bartlett, P. Measurement of low glucose concentrations using a microelectrochemical enzyme transistor. *Analyst* **123**, 387–392 (1998).
57. Khodagholy, D. *et al.* Organic electrochemical transistor incorporating an ionogel as a solid state electrolyte for lactate sensing. *J. Mater. Chem.* **22**, 4440 (2012).
58. Braendlein, M. *et al.* Lactate Detection in Tumor Cell Cultures Using Organic Transistor Circuits. *Adv. Mater.* 1605744 (2017). doi:10.1002/adma.201605744
59. Nishizawa, M., Matsue, T. & Uchida, I. Penicillin sensor based on a microarray electrode coated with pH-responsive polypyrrole. *Anal. Chem.* **64**, 2642–2644 (1992).
60. Kergoat, L. *et al.* Detection of glutamate and acetylcholine with organic electrochemical transistors based on conducting polymer/platinum nanoparticle composites. *Adv. Mater.* **26**, 5658–5664 (2014).
61. Bihar, E. *et al.* A Disposable paper breathalyzer with an alcohol sensing organic electrochemical transistor. *Sci. Rep.* **6**, 27582 (2016).
62. Tang, H., Lin, P., Chan, H. L. W. & Yan, F. Highly sensitive dopamine biosensors based on organic electrochemical transistors. *Biosens. Bioelectron.* **26**, 4559–4563 (2011).
63. Yao, C. *et al.* Organic Electrochemical Transistor Array for Recording Transepithelial Ion Transport of Human Airway Epithelial Cells. *Adv. Mater.* **25**, 6575–6580 (2013).
64. Ramuz, M. *et al.* Combined optical and electronic sensing of epithelial cells using planar organic transistors. *Adv. Mater.* **26**, 7083–7090 (2014).
65. Tria, S. A. *et al.* Dynamic monitoring of Salmonella typhimurium infection of polarized epithelia using organic transistors. *Adv. Heal. Mater.* **3**, 1053–1060 (2014).
66. Lin, P., Luo, X., Hsing, I. M. & Yan, F. Organic electrochemical transistors integrated in flexible microfluidic systems and used for label-free DNA sensing. *Adv. Mater.* **23**, 4035–4040 (2011).
67. Campana, A., Cramer, T., Simon, D. T., Berggren, M. & Biscarini, F. Electrocardiographic Recording with Conformable Organic Electrochemical Transistor Fabricated on Resorbable Bioscaffold. *Adv. Mater.* **26**, 3874–3878 (2014).
68. Gu, X., Yao, C., Liu, Y. & Hsing, I.-M. 16-Channel Organic Electrochemical Transistor Array for In Vitro Conduction Mapping of Cardiac Action Potential. *Adv. Healthc. Mater.* **5**, 2345–2351 (2016).
69. Khodagholy, D. *et al.* In vivo recordings of brain activity using organic transistors. *Nat. Commun.* **4**, 1575 (2013).
70. Rivnay, J., Owens, R. M. & Malliaras, G. G. The Rise of Organic Bioelectronics. *Chem. Mater.* **26**, 679–685 (2014).

71. Indiveri, G. *et al.* Neuromorphic Silicon Neuron Circuits. *Front. Neurosci.* **5**, 73 (2011).
72. Mead, C. Neuromorphic electronic systems. *Proceedings of the IEEE* **78**, 1629–1636 (1990).
73. Kuzum, D., Yu, S. & Philip Wong, H.-S. Synaptic electronics: materials, devices and applications. *Nanotechnology* **24**, 382001 (2013).
74. Gkoupidenis, P., Schaefer, N., Strakosas, X., Fairfield, J. A. & Malliaras, G. G. Synaptic plasticity functions in an organic electrochemical transistor. *Appl. Phys. Lett.* **107**, 263302 (2015).
75. Gkoupidenis, P., Schaefer, N., Garlan, B. & Malliaras, G. G. Neuromorphic Functions in PEDOT:PSS Organic Electrochemical Transistors. *Adv. Mater.* **27**, 7176–7180 (2015).
76. Zang, Y., Shen, H., Huang, D., Di, C.-A. A. & Zhu, D. A Dual-Organic-Transistor-Based Tactile-Perception System with Signal-Processing Functionality. *Adv. Mater.* **29**, 1606088 (2017).
77. Kong, L. *et al.* Spatially-correlated neuron transistors with ion-gel gating for brain-inspired applications. *Org. Electron. physics, Mater. Appl.* **44**, 25–31 (2017).
78. Qian, C. *et al.* Multi-gate organic neuron transistors for spatiotemporal information processing. *Appl. Phys. Lett.* **110**, 83302 (2017).
79. Qian, C. *et al.* Artificial Synapses Based on In-Plane Gate Organic Electrochemical Transistors. *ACS Appl. Mater. Interfaces* amsami.6b08866 (2016). doi:10.1021/acsami.6b08866
80. Winther-Jensen, B., Kolodziejczyk, B. & Winther-Jensen, O. New one-pot poly(3,4-ethylenedioxythiophene): poly(tetrahydrofuran) memory material for facile fabrication of memory organic electrochemical transistors. *APL Mater.* **3**, 14903 (2015).
81. van de Burgt, Y. *et al.* A non-volatile organic electrochemical device as a low-voltage artificial synapse for neuromorphic computing. *Nat. Mater.* **16**, 414–418 (2017).
82. Gkoupidenis, P., Koutsouras, D. A. & Malliaras, G. G. Neuromorphic device architectures with global connectivity through electrolyte gating. *Nat. Commun.* **8**, 15448 (2017).
83. Turrigiano, G. G. & Nelson, S. B. Homeostatic plasticity in the developing nervous system. *Nat Rev Neurosci* **5**, 97–107 (2004).
84. Rivnay, J. *et al.* Organic electrochemical transistors with maximum transconductance at zero gate bias. *Adv. Mater.* **25**, 7010–7014 (2013).
85. Wang, X. & Smela, E. Color and volume change in PPy(DBS). *J. Phys. Chem. C* **113**, 359–368 (2009).

86. Kim, Y., Kim, Y., Kim, S. & Kim, E. Electrochromic diffraction from nanopatterned poly(3-hexylthiophene). *ACS Nano* **4**, 5277–5284 (2010).
87. Tarver, J. & Loo, Y. L. Mesostuctures of polyaniline films affect polyelectrochromic switching. *Chem. Mater.* **23**, 4402–4409 (2011).
88. Heeger, A. J., Sariciftci, N. S. & Nardas, E. B. *Semiconducting and Metallic Polymers*. (Oxford University Press, 2010).
89. Bubnova, O., Berggren, M. & Crispin, X. Tuning the thermoelectric properties of conducting polymers in an electrochemical transistor Tuning the thermoelectric properties of conducting polymers in an electrochemical transistor. *J. Am. Chem. Soc.* **134**, 16456 (2012).
90. Andersson, P. *et al.* Active matrix displays based on all-organic electrochemical smart pixels printed on paper. *Adv. Mater.* **14**, 1460–1464 (2002).
91. Bhuvana, T., Kim, B., Yang, X., Shin, H. & Kim, E. Reversible Full-Color Generation with Patterned Yellow Electrochromic Polymers. *Angew. Chemie Int. Ed.* **52**, 1180–1184 (2013).
92. Dehmel, R., Nicolas, A., Scherer, M. R. J. & Steiner, U. 3D Nanostructured Conjugated Polymers for Optical Applications. 1–6 (2015). doi:10.1002/adfm.201502392
93. Admassie, S. & Inganäs, O. Electrochromism in Diffractive Conducting Polymer Gratings. *J. Electrochem. Soc.* **151**, H153–H157 (2004).
94. Marks, Z. D. *et al.* Switchable diffractive optics using patterned PEDOT:PSS based electrochromic thin-films. *Org. Electron.* **37**, 271–279 (2016).
95. Tehrani, P. *et al.* Patterning polythiophene films using electrochemical over-oxidation. *Smart Mater. Struct.* **14**, N21–N25 (2005).
96. Inal, S., Malliaras, G. G. & Rivnay, J. Optical study of electrochromic moving fronts for the investigation of ion transport in conducting polymers. *J. Mater. Chem. C* (2016). doi:10.1039/C5TC04354A
97. Rivnay, J. *et al.* Structural control of mixed ionic and electronic transport in conducting polymers. *Nat. Commun.* **7**, 11287 (2016).
98. Wang, X., Shapiro, B. & Smela, E. Development of a Model for Charge Transport in Conjugated Polymers. *J. Phys. Chem. C* **113**, 382–401 (2009).
99. Stavrinidou, E. *et al.* Direct measurement of ion mobility in a conducting polymer. *Adv. Mater.* **25**, 4488–4493 (2013).
100. Håkansson, A. *et al.* Effect of (3-glycidylxypropyl)trimethoxysilane (GOPS) on the electrical properties of PEDOT:PSS films. *J. Polym. Sci. Part B Polym. Phys.* 1–7 (2017).

doi:10.1002/polb.24331

101. Holloway, P. H., Amos, D. E. & Nelson, G. C. Analysis of grain- boundary diffusion in thin films: Chromium in gold. *J. Appl. Phys.* **47**, 3769–3775 (1976).
102. Jimison, L. H. *et al.* Measurement of Barrier Tissue Integrity with an Organic Electrochemical Transistor. *Adv. Mater.* **24**, 5919–5923 (2012).
103. Liao, C., Zhang, M., Niu, L., Zheng, Z. & Yan, F. Highly selective and sensitive glucose sensors based on organic electrochemical transistors with graphene-modified gate electrodes. *J. Mater. Chem. B* **1**, 3820–3829 (2013).
104. Yaghmazadeh, O. *et al.* Optimization of organic electrochemical transistors for sensor applications. *J. Polym. Sci. Part B Polym. Phys.* **49**, 34–39 (2011).
105. Svensson, P.-O., Nilsson, D., Forchheimer, R. & Berggren, M. A sensor circuit using reference-based conductance switching in organic electrochemical transistors. *Appl. Phys. Lett.* **93**, 203301 (2008).
106. Stavrinidou, E. *et al.* A simple model for ion injection and transport in conducting polymers. *J. Appl. Phys.* **113**, 244501 (2013).
107. Gualandi, I. *et al.* A simple all-PEDOT:PSS electrochemical transistor for ascorbic acid sensing. *J. Mater. Chem. B* (2015). doi:10.1039/c5tb00916b
108. Toss, H. *et al.* On the mode of operation in electrolyte-gated thin film transistors based on different substituted polythiophenes. *Org. Electron.* **15**, 2420–2427 (2014).
109. Tanase, C., Meijer, E. J., Blom, P. W. M. & de Leeuw, D. M. Unification of the Hole Transport in Polymeric Field-Effect Transistors and Light-Emitting Diodes. *Phys. Rev. Lett.* **91**, 216601 (2003).
110. Arkhipov, V. I., Heremans, P., Emelianova, E. V., Adriaenssens, G. J. & Bäessler, H. Charge carrier mobility in doped semiconducting polymers. *Appl. Phys. Lett.* **82**, 3245 (2003).
111. Bouhassoune, M., Mensfoort, S. L. M. van, Bobbert, P. A. & Coehoorn, R. Carrier-density and field-dependent charge-carrier mobility in organic semiconductors with correlated Gaussian disorder. *Org. Electron.* **10**, 437–445 (2009).
112. Coehoorn, R., Pasveer, W. F., Bobbert, P. a. & Michels, M. a J. Charge-carrier concentration dependence of the hopping mobility in organic materials with Gaussian disorder. *Phys. Rev. B - Condens. Matter Mater. Phys.* **72**, 155206 (2005).
113. Pasveer, W. F. *et al.* Unified Description of Charge-Carrier Mobilities in Disordered Semiconducting Polymers. *Phys. Rev. Lett.* **94**, 206601 (2005).
114. Zhou, J. *et al.* Monte Carlo simulation of charge transport in electrically doped organic

- solids. *J. Phys. D. Appl. Phys.* **42**, 35103 (2009).
115. Bisquert, J. Interpretation of electron diffusion coefficient in organic and inorganic semiconductors with broad distributions of states. *Phys. Chem. Chem. Phys.* **10**, 3175–3194 (2008).
 116. Xia, Y., Cho, J. H., Lee, J., Ruden, P. P. & Frisbie, C. D. Comparison of the Mobility-Carrier Density Relation in Polymer and Single-Crystal Organic Transistors Employing Vacuum and Liquid Gate Dielectrics. *Adv Mater* **21**, 2174–2179 (2009).
 117. Shen, Y. *et al.* Charge transport in doped organic semiconductors. *Phys. Rev. B* **68**, (2003).
 118. Mozer, A. J. *et al.* Time-dependent mobility and recombination of the photoinduced charge carriers in conjugated polymer/fullerene bulk heterojunction solar cells. *Phys. Rev. B* **72**, 35217 (2005).
 119. Vissenberg, M. C. J. M. & Matters, M. Theory of the field-effect mobility in amorphous organic transistors. *Phys. Rev. B* **57**, 12964–12967 (1998).
 120. Wang, S., Ha, M., Manno, M., Daniel Frisbie, C. & Leighton, C. Hopping transport and the Hall effect near the insulator-metal transition in electrochemically gated poly(3-hexylthiophene) transistors. *Nat Commun* **3**, 1210 (2012).
 121. Hulea, I. N. *et al.* Wide Energy-Window View on the Density of States and Hole Mobility in Poly(p-Phenylene Vinylene). *Phys. Rev. Lett.* **93**, 166601 (2004).
 122. Paulsen, B. D. & Frisbie, C. D. Dependence of Conductivity on Charge Density and Electrochemical Potential in Polymer Semiconductors Gated with Ionic Liquids. *J. Phys. Chem. C* **116**, 3132–3141 (2012).
 123. Tu, D. *et al.* A Static Model for Electrolyte-Gated Organic Field-Effect Transistors. *IEEE Trans. Electron Devices* **58**, 3574–3582 (2011).
 124. Tu, D., Kergoat, L., Crispin, X., Berggren, M. & Forchheimer, R. Transient analysis of electrolyte-gated organic field-effect transistors. *SPIE Organic Photonics+ Electronics* 84780L–84780L–9 (2012).
 125. Stenger-Smith, J. D. *et al.* Poly(3,4-alkylenedioxythiophene)-Based Supercapacitors Using Ionic Liquids as Supporting Electrolytes. *J. Electrochem. Soc.* **149**, A973 (2002).
 126. Kalb, W. L. & Batlogg, B. Calculating the trap density of states in organic field-effect transistors from experiment: A comparison of different methods. *Phys. Rev. B* **81**, 35327 (2010).
 127. Gustafsson, J. C., Liedberg, B. & Inganäs, O. In situ spectroscopic investigations of electrochromism and ion transport in a poly(3,4-ethylenedioxythiophene) electrode in a solid state electrochemical cell. *Solid State Ionics* **69**, 145–152 (1994).

128. Huang, J.-H., Kekuda, D., Chu, C.-W. & Ho, K.-C. Electrochemical characterization of the solvent-enhanced conductivity of poly(3,4-ethylenedioxythiophene) and its application in polymer solar cells. *J. Mater. Chem.* **19**, 3704–3712 (2009).
129. Groenendaal, L., Zotti, G., Aubert, P. H., Waybright, S. M. & Reynolds, J. R. Electrochemistry of Poly(3,4-alkylenedioxythiophene) Derivatives. *Adv Mater* **15**, 855–879 (2003).
130. Chen, X. & Inganäs, O. Three-Step Redox in Polythiophenes: Evidence from Electrochemistry at an Ultramicroelectrode. *J. Phys. Chem.* **100**, 15202–15206 (1996).
131. Ramuz, M. *et al.* Optimization of a Planar All-Polymer Transistor for Characterization of Barrier Tissue. *ChemPhysChem* **16**, 1210–1216 (2015).
132. Bernardis, D. A., Malliaras, G. G., Toombes, G. E. S. & Gruner, S. M. Gating of an organic transistor through a bilayer lipid membrane with ion channels. *Appl. Phys. Lett.* **89**, 53505 (2006).
133. Herlogsson, L. *et al.* Downscaling of Organic Field-Effect Transistors with a Polyelectrolyte Gate Insulator. *Adv Mater* **20**, 4708–4713 (2008).
134. Leleux, P. *et al.* Organic Electrochemical Transistors for Clinical Applications. *Adv. Healthc. Mater.* **4**, 142–147 (2015).
135. Blaudeck, T. *et al.* Simplified large-area manufacturing of organic electrochemical transistors combining printing and a self-aligning laser ablation step. *Adv. Funct. Mater.* **22**, 2939–2948 (2012).
136. Andersson Ersman, P., Nilsson, D., Kawahara, J., Gustafsson, G. & Berggren, M. Fast-switching all-printed organic electrochemical transistors. *Org. Electron.* **14**, 1276–1280 (2013).
137. Zhang, S. *et al.* Water stability and orthogonal patterning of flexible micro-electrochemical transistors on plastic. *J. Mater. Chem. C* **4**, 1382–1385 (2016).
138. Scheiblin, G., Coppard, R., Owens, R. M., Mailley, P. & Malliaras, G. G. Referenceless pH Sensor using Organic Electrochemical Transistors. *Adv. Mater. Technol.* **2**, 1600141 (2017).
139. Demelas, M., Scavetta, E., Basiricò, L., Rogani, R. & Bonfiglio, A. A deeper insight into the operation regime of all-polymeric electrochemical transistors. *Appl. Phys. Lett.* **102**, 193301 (2013).
140. Friedlein, J. T., Shaheen, S. E., Malliaras, G. G. & McLeod, R. R. Optical Measurements Revealing Nonuniform Hole Mobility in Organic Electrochemical Transistors. *Adv. Electron. Mater.* **1**, 1500189 (2015).
141. Bittle, E. G., Basham, J. I., Jackson, T. N., Jurchescu, O. D. & Gundlach, D. J. Mobility

- overestimation due to gated contacts in organic field-effect transistors. *Nat. Commun.* **7**, 10908 (2016).
142. Richards, T. J. & Siringhaus, H. Analysis of the contact resistance in staggered, top-gate organic field-effect transistors. *J. Appl. Phys.* **102**, 94510 (2007).
 143. Xu, Y. *et al.* Modified transmission-line method for contact resistance extraction in organic field-effect transistors. *Appl. Phys. Lett.* **97**, 1–3 (2010).
 144. Ambegaokar, V., Halperin, B. I. & Langer, J. S. Hopping conductivity in disordered systems. *Phys. Rev. B* **4**, 2612–2620 (1971).
 145. Tessler, N., Preezant, Y., Rappaport, N. & Roichman, Y. Charge Transport in Disordered Organic Materials and Its Relevance to Thin-Film Devices: A Tutorial Review. *Adv. Mater.* **21**, 2741–2761 (2009).
 146. Ihnatsenka, S., Crispin, X. & Zozoulenko, I. V. Understanding hopping transport and thermoelectric properties of conducting polymers. *Phys. Rev. B* **92**, 35201 (2015).
 147. Arkhipov, V. I., Emelianova, E. V., Heremans, P. & Bäessler, H. Analytic model of carrier mobility in doped disordered organic semiconductors. *Phys. Rev. B* **72**, 235202 (2005).
 148. Mort, J., Grammatica, S., Sandman, D. J. & Troup, A. Chemical control of conductivity in a molecularly-doped polymer. *J. Electron. Mater.* **9**, 411–418 (1980).
 149. Pingel, P., Schwarzl, R. & Neher, D. Effect of molecular p-doping on hole density and mobility in poly(3-hexylthiophene). *Appl. Phys. Lett.* **100**, 98–101 (2012).
 150. Garcia-Belmonte, G., Boix, P. P., Bisquert, J., Sessolo, M. & Bolink, H. J. Simultaneous determination of carrier lifetime and electron density-of-states in P3HT:PCBM organic solar cells under illumination by impedance spectroscopy. *Sol. Energy Mater. Sol. Cells* **94**, 366–375 (2010).
 151. Garcia-Belmonte, G., Vakarin, E. V., Bisquert, J. & Badiali, J. P. Doping-induced broadening of the hole density-of-states in conducting polymers. *Electrochim. Acta* **55**, 6123–6127 (2010).
 152. Arkhipov, V. I., Heremans, P., Emelianova, E. V. & Bäessler, H. Effect of doping on the density-of-states distribution and carrier hopping in disordered organic semiconductors. *Phys. Rev. B* **71**, 45214 (2005).
 153. Klatt, M. A., Schröder-Turk, G. E. & Mecke, K. Anisotropy in finite continuum percolation: threshold estimation by Minkowski functionals. *J. Stat. Mech. Theory Exp.* **2017**, 023302 (2017).
 154. Stafström, S. & Brédas, J. L. Evolution of the electronic structure of polyacetylene and polythiophene as a function of doping level and lattice conformation. *Phys. Rev. B* **38**, 4180–4191 (1988).

155. Nardes, A. M. *et al.* Microscopic Understanding of the Anisotropic Conductivity of PEDOT:PSS Thin Films. *Adv. Mater.* **19**, 1196–1200 (2007).
156. Hou, J., Chen, H.-Y., Zhang, S. & Yang, Y. Synthesis and Photovoltaic Properties of Two Benzo[1,2-b:3,4-b']dithiophene-Based Conjugated Polymers. *J. Phys. Chem. C* **113**, 21202–21207 (2009).
157. Tarabella, G. *et al.* New opportunities for organic electronics and bioelectronics: ions in action. *Chem. Sci.* **4**, 1395 (2013).
158. Liao, C. *et al.* Flexible Organic Electronics in Biology: Materials and Devices. *Adv. Mater.* **27**, 7493–7527 (2015).
159. Yao, C., Li, Q., Guo, J., Yan, F. & Hsing, I. M. Rigid and Flexible Organic Electrochemical Transistor Arrays for Monitoring Action Potentials from Electrogenic Cells. *Adv. Healthc. Mater.* **4**, 528–533 (2015).
160. Ramuz, M., Hama, A., Rivnay, J., Leleux, P. & Owens, R. M. Monitoring of cell layer coverage and differentiation with the organic electrochemical transistor. *J. Mater. Chem. B* **3**, 5971–5977 (2015).
161. Nilsson, D. An Organic Electrochemical Transistor for Printed Sensors and Logic. *Science And Technology* (Linköping University, 2005).
162. Demin, V. A. *et al.* Hardware elementary perceptron based on polyaniline memristive devices. *Org. Electron.* **25**, 16–20 (2015).
163. Rothlander, T. *et al.* Nanoimprint lithography-structured organic electrochemical transistors and logic circuits. *IEEE Trans. Electron Devices* **61**, 1515–1519 (2014).
164. Tang, H. *et al.* Conducting polymer transistors making use of activated carbon gate electrodes. *ACS Appl. Mater. Interfaces* **7**, 969–73 (2015).
165. Tarabella, G. *et al.* Organic electrochemical transistors monitoring micelle formation. *Chem. Sci.* **3**, 3432 (2012).
166. Mabeck, J. T. *et al.* Microfluidic gating of an organic electrochemical transistor. *Appl. Phys. Lett.* **87**, 13503 (2005).
167. Hütter, P. C., Rothländer, T., Haase, A., Trimmel, G. & Stadlober, B. Influence of geometry variations on the response of organic electrochemical transistors. *Appl. Phys. Lett.* **103**, 15–19 (2013).
168. Abidian, M. R. & Martin, D. C. Experimental and theoretical characterization of implantable neural microelectrodes modified with conducting polymer nanotubes. *Biomaterials* **29**, 1273–1283 (2008).
169. Tsvividis, Y. & Milios, J. A detailed look at electrical equivalents of uniform

- electrochemical diffusion using nonuniform resistance-capacitance ladders. *J. Electroanal. Chem.* **707**, 156–165 (2013).
170. Bobacka, J., Lewenstam, A. & Ivaska, A. Electrochemical impedance spectroscopy of oxidized poly(3,4-ethylenedioxythiophene) film electrodes in aqueous solutions. *J. Electroanal. Chem.* **489**, 17–27 (2000).
171. Oh, S.-Y., Ward, D. E. & Dutton, R. W. Transient analysis of MOS transistors. *IEEE Trans. Electron Devices* **27**, 1571–1578 (1980).
172. Meyer, J. E. MOS models and circuit simulation. *RCA Rev.* **32**, 42–63 (1971).
173. Braga, D., Erickson, N. C., Renn, M. J., Holmes, R. J. & Frisbie, C. D. High-transconductance organic thin-film electrochemical transistors for driving low-voltage red-green-blue active matrix organic light-emitting devices. *Adv. Funct. Mater.* **22**, 1623–1631 (2012).
174. Wei, Q., Mukaida, M., Kirihaara, K., Naitoh, Y. & Ishida, T. Photoinduced Dedoping of Conducting Polymers: An Approach to Precise Control of the Carrier Concentration and Understanding Transport Properties. *ACS Appl. Mater. Interfaces* **8**, 2054–2060 (2016).
175. Barthó, P. *et al.* Characterization of Neocortical Principal Cells and Interneurons by Network Interactions and Extracellular Features. *J. Neurophysiol.* **92**, 600–608 (2004).
176. Khodagholy, D. *et al.* NeuroGrid: recording action potentials from the surface of the brain. *Nat. Neurosci.* **18**, 310–315 (2015).
177. Gold, C., Henze, D. A., Koch, C. & Buzsáki, G. On the origin of the extracellular action potential waveform: A modeling study. *J. Neurophysiol.* **95**, 3113–3128 (2006).
178. Greczynski, G. *et al.* Photoelectron spectroscopy of thin films of PEDOT–PSS conjugated polymer blend: a mini-review and some new results. *J. Electron Spectros. Relat. Phenomena* **121**, 1–17 (2001).
179. Möller, S., Forrest, S. R., Perlov, C., Jackson, W. & Taussig, C. Electrochromic conductive polymer fuses for hybrid organic/inorganic semiconductor memories. *J. Appl. Phys.* **94**, 7811 (2003).
180. Kumar, P. *et al.* Effect of channel thickness , electrolyte ions , and dissolved oxygen on the performance of organic electrochemical transistors Effect of channel thickness , electrolyte ions , and dissolved oxygen on the performance of organic electrochemical transistors. *Appl. Phys. Lett.* **107**, 53303 (2015).
181. Lee, J. Extraction of high charge density of states in electrolyte-gated polymer thin-film transistor with temperature-dependent measurements. *Appl. Phys. Lett.* **108**, 203302 (2016).
182. Gentile, F. *et al.* A theoretical model for the time varying current in organic

- electrochemical transistors in a dynamic regime. *Org. Electron.* **35**, 59–64 (2016).
183. Cheung, K. P. On the 60 mV/dec @300 K limit for MOSFET subthreshold swing. *Proc. 2010 Int. Symp. VLSI Technol. Syst. Appl.* **4**, 72–73 (2010).
184. Modha, D. S. Introducing a brain-inspired computer: TrueNorth's neurons to revolutionize system architecture. *IBM Research* (2014). at <http://www.research.ibm.com/articles/brain-chip.shtml>
185. Stoop, R. L. *et al.* Charge Noise in Organic Electrochemical Transistors. *Phys. Rev. Appl.* **7**, 14009 (2017).
186. Gkoupidenis, P., Koutsouras, D. A., Lonjaret, T., Fairfield, J. A. & Malliaras, G. G. Orientation selectivity in a multi-gated organic electrochemical transistor. *Sci. Rep.* **6**, 27007 (2016).
187. Faria, G. C., Duong, D. T. & Salleo, A. On the transient response of organic electrochemical transistors. *Org. Electron.* **45**, 215–221 (2017).
188. Stavrinidou, E., Sessolo, M., Winther-Jensen, B., Sanaur, S. & Malliaras, G. G. A physical interpretation of impedance at conducting polymer/electrolyte junctions. *AIP Adv.* **4**, 17127 (2014).
189. Inal, S. *et al.* Organic electrochemical transistors based on PEDOT with different anionic polyelectrolyte dopants. *J. Polym. Sci. Part B Polym. Phys.* n/a-n/a (2015). doi:10.1002/polb.23938
190. Wang, J., Gao, F. & Greenham, N. C. Low-power write-once-read-many-times memory devices. *Appl. Phys. Lett.* **97**, 2010–2013 (2010).
191. Xuan, Y., Sandberg, M., Berggren, M. & Crispin, X. An all-polymer-air PEDOT battery. *Org. Electron.* **13**, 632–637 (2012).
192. Bubnova, O. *et al.* Semi-metallic polymers. *Nat. Mater.* **13**, 190–194 (2013).
193. Vitoratos, E. *et al.* Thermal degradation mechanisms of PEDOT:PSS. *Org. Electron. physics, Mater. Appl.* **10**, 61–66 (2009).
194. Stepien, L. *et al.* Thermal operating window for PEDOT:PSS films and its related thermoelectric properties. *Synth. Met.* **225**, 49–54 (2017).
195. Winter, I., Reese, C., Hormes, J., Heywang, G. & Jonas, F. The thermal ageing of poly(3,4-ethylenedioxythiophene). An investigation by X-ray absorption and X-ray photoelectron spectroscopy. *Chem. Phys.* **194**, 207–213 (1995).
196. Lee, S., Paine, D. C. & Gleason, K. K. Heavily Doped poly(3,4-ethylenedioxythiophene) Thin Films with High Carrier Mobility Deposited Using Oxidative CVD: Conductivity Stability and Carrier Transport. *Adv. Funct. Mater.* **24**, 7187–7196 (2014).

197. Pei, Q., Zuccarello, G., Ahlskog, M. & Inganäs, O. Electrochromic and highly stable poly(3,4-ethylenedioxythiophene) switches between opaque blue-black and transparent sky blue. *Polymer (Guildf)*. **35**, 1347–1351 (1994).
198. Takahashi, T., Ishihara, M. & Okuzaki, H. Poly(3,4-ethylenedioxythiophene)/poly(4-styrenesulfonate) microfibers. *Synth. Met.* **152**, 73–76 (2005).
199. Choi, J. W., Han, M. G., Kim, S. Y., Oh, S. G. & Im, S. S. Poly(3,4-ethylenedioxythiophene) nanoparticles prepared in aqueous DBSA solutions. *Synth. Met.* **141**, 293–299 (2004).
200. Huh, P.-H. *et al.* Recovery and characterization of pure poly(3,4-ethylenedioxythiophene) via biomimetic template polymerization. *Polym. Eng. Sci.* **47**, 71–75 (2007).
201. Zhan, L. *et al.* PEDOT: Cathode active material with high specific capacity in novel electrolyte system. *Electrochim. Acta* **53**, 8319–8323 (2008).
202. Zhang, S. *et al.* Solvent-induced changes in PEDOT:PSS films for organic electrochemical transistors. *APL Mater.* **3**, 14911 (2014).
203. Fan, B., Mei, X. & Ouyang, J. Significant Conductivity Enhancement of Conductive Poly(3,4-ethylenedioxythiophene):Poly(styrenesulfonate) Films by Adding Anionic Surfactants into Polymer Solution. *Macromolecules* **41**, 5971–5973 (2008).
204. Ouyang, J. ‘Secondary doping’ methods to significantly enhance the conductivity of PEDOT:PSS for its application as transparent electrode of optoelectronic devices. *Displays* **34**, 423–436 (2013).
205. Oostra, A. J., van den Bos, K. H. W., Blom, P. W. M. & Michels, J. J. Disruption of the Electrical Conductivity of Highly Conductive Poly(3,4-ethylenedioxythiophene):Poly(styrene sulfonate) by Hypochlorite. *J. Phys. Chem. B* **117**, 10929–10935 (2013).
206. Kawahara, J., Ersman, P. A., Engquist, I. & Berggren, M. Improving the color switch contrast in PEDOT:PSS-based electrochromic displays. *Org. Electron.* **13**, 469–474 (2012).
207. Taylor, P. G. *et al.* Orthogonal Patterning of PEDOT:PSS for Organic Electronics using Hydrofluoroether Solvents. *Adv. Mater.* **21**, 2314–2317 (2009).
208. Andersson, P., Forchheimer, R., Tehrani, P. & Berggren, M. Printable All- Organic Electrochromic Active- Matrix Displays. *Adv. Funct. Mater.* **17**, 3074–3082 (2007).
209. Muller, R. S., Kamins, T. I. & Chan, M. *Device Electronics for Integrated Circuits*. (John Wiley & Sons, 2003).
210. Funaki, T. & Hikiyama, T. Characterization and Modeling of the Voltage Dependency of Capacitance and Impedance Frequency Characteristics of Packed EDLCs. *Power*

- Electron. IEEE Trans.* **23**, 1518–1525 (2008).
211. Zubieta, L. & Bonert, R. Characterization of double-layer capacitors for power electronics applications. *Ind. Appl. IEEE Trans.* **36**, 199–205 (2000).
 212. Dieckmann, A., Bäessler, H. & Borsenberger, P. M. An assessment of the role of dipoles on the density-of-states function of disordered molecular solids. *J. Chem. Phys.* **99**, 8136 (1993).
 213. Sessolo, M. *et al.* Easy-to-Fabricate Conducting Polymer Microelectrode Arrays. *Adv. Mater.* **25**, 2135–2139 (2013).
 214. Defranco, J. A., Schmidt, B. S., Lipson, M. & Malliaras, G. G. Photolithographic patterning of organic electronic materials. *Org. Electron.* **7**, 22–28 (2006).
 215. Sedra, A. S. & Smith, K. C. *Microelectronic circuits*. (Oxford University Press, 2010).

APPENDIX I: SUPPORTING MATERIAL FOR CHAPTER II

A. Chapter II experimental details

1. Fresnel lens

To fabricate the switchable organic electrochromic device (OECD), ITO-coated 25 mm × 25 mm glass slides (Sigma-Aldrich) with a sheet resistivity of 8 – 12 Ω/\square were used as substrates. The coated slides were cleaned in soap solution, acetone, and isopropanol in a sonicator (Branson) and subsequently dried by blowing with N₂ gas. The electrochromic solution consisted of PEDOT:PSS (Clevios PH-1000, Heraeus), 5 v/v % glycerol, 0.5 v/v % dodecylbenzenesulfonic acid (DBSA, Sigma-Aldrich), and 1 w/w % (3-glycidyloxypropyl)trimethoxysilane (GOPS, Sigma-Aldrich) and was spin-coated onto the substrate at 1000 rpm for 60 s. The presence of glycerol enhances the conductivity of the PEDOT:PSS formulation while the DBSA serves as a surfactant.²⁰² GOPS enhances the hydrolytic stability of the formulation and prevents delamination from the underlying substrate.^{137,203,204} PEDOT:PSS was also spin-coated onto a blank glass microscope slide as a control in the absence of the ITO layer to measure the thickness and conductivity of the film. After spinning on the PEDOT:PSS solution, the device was baked on a hotplate at 120 °C for 20 min to dry the film. A positive photoresist (AZ 4210, Futurrex) was spin-coated onto the PEDOT:PSS-coated ITO slide and patterned in a Karl Suss MJB3 mask aligner using a photomask with the pattern for the Fresnel lens. The photoresist was developed according to the manufacturer's directions and the patterned device was exposed to a 150 W O₂ plasma for 30 s to descum the surface. The patterned device was subsequently soaked in a 1:4 solution of commercial bleach (Clorox™, 8.25% sodium hypochlorite) and water for 5 s and then rinsed in deionized water. This soak chemically over-oxidizes the PEDOT:PSS and turns the exposed

regions into a non-conductive, transparent, and electrochemically inactive film.²⁰⁵ The photoresist was removed with acetone and methanol and dried by blowing with N₂ gas.

The final device was assembled as a sandwiched structure composed of a gel electrolyte between the PEDOT:PSS/ITO/glass slide and a blank ITO/glass slide, as shown in Figure II-3 of chapter II. Copper tape with conductive adhesive (3M™ Copper Foil Shielding Tape) was wrapped around both the patterned and blank ITO-coated glass slide to make electrical contacts. The gel electrolyte solution was formulated using 40 w/w % of poly(sodium 4-styrenesulfonate) (Na:PSS, Sigma-Aldrich) with an average molecular weight of 70,000 Da, 10 w/w % D-sorbitol, 10 w/w % glycerol, and 40 w/w % deionized water.²⁰⁶ This viscous formulation was then sandwiched between the patterned PEDOT:PSS/ITO/glass slide and the blank ITO/glass slide with the ITO side facing the electrolyte. A rubber shim with a thickness of 1/32 in. was used as a spacer for the electrolyte. The slides were clipped together, and the sandwiched device was then left to dry overnight. Finally, wires were soldered onto the copper tape electrical contacts on the back of the slide for testing.

Device characterization

The thickness and conductivity of the PEDOT:PSS film on the control glass slide were measured using a Dektak profilometer and four-point probe, respectively. The spin-coated PEDOT:PSS film thickness was measured to be 230 nm with a conductivity of 345 S/cm.

The diffraction efficiency (DE) of the OECDs was measured using the optical setup described in Figure VII-1. The DE is defined as the ratio of the optical power in the first-order diffracted spot in the ‘on’ or ‘off’ state to the power of the total transmission through the device in the fully oxidized state at -1 V. Referencing the measurement to the fully oxidized state

accounts for the optical losses in the electrolyte and at the glass interfaces in order to better estimate the intrinsic OECD DE.

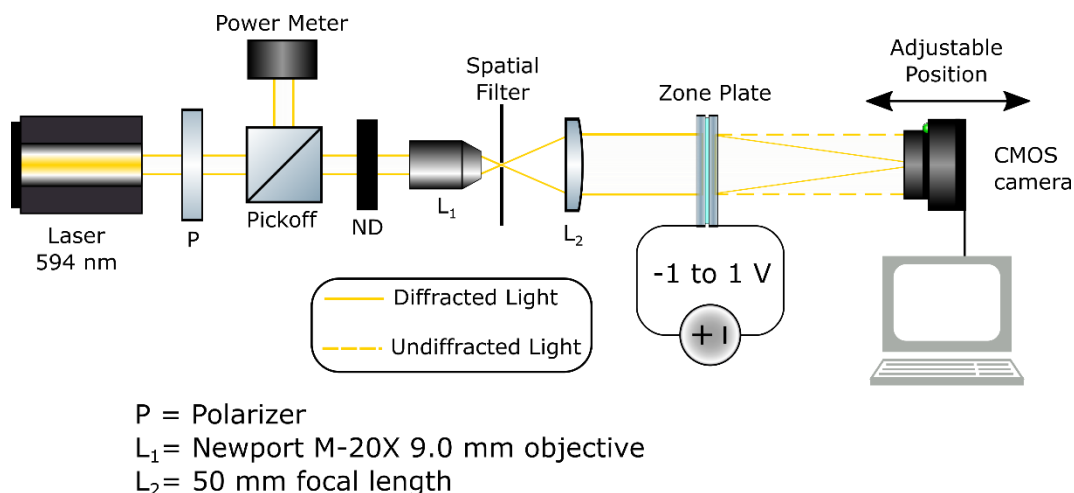


Figure VII-1. Experimental setup for measuring the diffraction efficiency, focal length, and spot size of the Fresnel zone plate lenses. The laser beam is expanded (lenses L_1 and L_2) to fill the back aperture of each FZP and the focused light is recorded by an adjustable rail-mounted CMOS camera.

2. Ion transport measurements

Approximately 100 nm thick gold electrodes were evaporated onto glass substrates with an ~ 5 nm chromium adhesion layer and patterned via standard photolithographic liftoff using Shipley 1813 resist. After patterning the gold, two layers of 2 μm thick parylene C (PaC) was evaporated onto the sample. A silane adhesion agent was included in the evaporation chamber during the first PaC evaporation. 2% micro-90 in water was spun onto the sample as an anti-adhesion layer after the first PaC layer and before the second layer. Both layers of PaC were patterned via reactive ion etching with oxygen plasma and CHF_3 process gases and an etch mask of AZ 9260 photoresist. After etching the PaC, a PEDOT:PSS solution (94 wt% Clevios PH-1000, 5 wt% ethylene glycol, 1 wt% 3-glycidoxypropyltrimethoxysilane, and 0.1 wt% dodecylbenzenesulfonic acid) was spun-cast onto the sample. Two layers of PEDOT:PSS were cast. The first was cast at 3000 rpm for 60 s, and the second layer was cast at 1000 rpm for 60

s. The PEDOT:PSS was baked at 70 °C for 90 s after the first layer and after the second layer. Then, the PEDOT:PSS was patterned by peeling off the sacrificial PaC layer.²⁰⁷ Then the PEDOT:PSS was baked at 125 °C for 75 minutes. The sample was then rinsed with acetone and 2-propanol. Then it was baked at 95 °C for 10 minutes. Next, SU-8 - 10 was patterned on top of the sample to act as an ion barrier. The SU-8 was deposited on the sample and spun on with a three step program as follows: Step 1) 300 rpm, 133 rpm/s, 10 s. Step 2) 3000 rpm, 266 rpm/s, 10 s; Step 3) 3000 rpm, 10000 rpm/s, 60 s. The SU-8 was baked for 2 minutes at 65 °C, then 5 minutes at 95 °C. It was exposed with a mercury-lamp mask aligner. Then the sample was baked for 2 minutes at 65 °C then 5 minutes at 95 °C. The sample was then developed in neat SU-8 developer for 30 s, immediately rinsed in 2-propanol for 30 s, and immediately rinsed in deionized water for 30 s. Finally, the device was annealed for 3 minutes at 60 °C, then 3 minutes at 90 °C, and then 10 minutes at 120 °C.

For optical characterization, we used a Motic SMZ 171 stereomicroscope with a Point Grey Grasshopper USB3 CMOS detector and a 54 LED ring illuminator with a color temperature of 5800 K (Omax part number A9254P). We used the Point Grey FlyCap2 software for image acquisition and captured frames with a bit depth of 8 at a frame rate of 100 frames per second. However, some frames were dropped, as can be noticed upon examination of Figure II-6e.

For the voltage measurements, we used our own software in Test Script Builder and Python 3 to synchronize a Keithley 2636A source-meter-unit and an Agilent B2962a source-meter-unit. Voltage was sourced at the Ag/AgCl counter electrode, and voltage was measured at the voltage probe electrodes by using a source-meter-unit channel to source zero current while measuring voltage. Not all voltage probes could be measured simultaneously because we didn't

have enough source-meter-unit channels. Therefore, three probes were measured at a time for three different sets of measurements to get all seven probes included. The center probe (at a distance of from the electrolyte) was measured in each measurement set. All of the data for the center probe line up on each other and are plotted in Figure II-6d, demonstrating the reproducibility of our measurements.

3. Simultaneous electrical and optical measurements of OECTs

Fabrication of transistors with gel electrolyte

Chromium/gold electrodes (5 nm/100 nm) were evaporated onto clean glass substrates and patterned using standard photolithographic liftoff. The channel length is , and the channel width is . Next, an nm film of a PEDOT:PSS solution (89.66 wt % of Clevios PH-500, 6.87 wt % of ethylene glycol, 3.13 wt % of water, and 0.35 wt % of Zonyl FS-300 fluorosurfactant) was spun-cast onto the chip. The PEDOT:PSS was patterned into transistor channels by scratching the film with a radius tungsten tip controlled with a motorized micropositioning system. After patterning the PEDOT:PSS, an electrolyte gel (94.5 wt % water, 3.5 wt % glycerol, and 2.0 wt % sodium-PSS (Alfa Aesar, MW = 70 000)) was drop-cast over the entire chip and allowed to dry for ~20 hours in ambient conditions.

Fabrication of transistors with liquid electrolyte

The transistors with liquid electrolyte were fabricated according to the parylene lift-off procedure outlined in Rivnay et al.⁸⁴ The PEDOT:PSS dispersion was spun at 3000 rpm for 30s.

Electrical characterization of transistors with gel electrolyte

The current-voltage measurements were made using a Keithley 2636A SMU with custom-written control code. Although the response time of the device is ~30 ms (see

Supporting Information), the current was allowed to settle for 6 s before it was recorded after each gate voltage step. This guarantees that the response reaches a steady state and that the gate current is at least 3 orders of magnitude less than the drain current (see Figure VII-12 and Figure VII-13). Between gate voltage steps, all electrodes were allowed to float for 3 minutes. Note that the gel electrolyte is rather transparent, and its optical absorption is not affected by an applied voltage.²⁰⁸

Electrical characterization of transistors with liquid electrolyte

The transistors with liquid electrolyte were characterized with 100 mM NaCl contained in a PDMS well. A Ag/AgCl pellet (2 mm diameter 2 mm height) was used as the gate electrode. Because the liquid-electrolyte devices are much faster than the gel-electrolyte transistors (see Figure VII-12 and Figure VII-14), the voltages are scanned at a rate of about 40 ms per step. The other details of the characterization are the same as in Rivnay et al.⁸⁴

Optical characterization

The optical measurements were only performed on the devices with the gel electrolyte, and they were made at the same time as the electrical measurements. The optical measurements were recorded with a monochrome, global shutter, CMOS camera (Point Grey G3-U3-23S6M) operated in 8-bit mode. The images were captured through a 10 X/0.25 NA objective using transillumination supplied by a white LED with a spectral cut-off near 650 nm (ThorLabs MCWHL2). The reported absorption increases are pixel intensities at each combination subtracted from the intensities when all electrodes are floating, and no pixels were ever saturated at 0 or 255. Due to interference ringing and shading effects near the electrodes, we do not record the optical response within of the electrode edges. Additionally, two regions are cropped out of the images due to bubbles and wrinkles in the electrolyte (see Figure VII-3).

B. Supplementary details about chapter II

1. Optical measurements

Characterization of the absorption

As stated in section I-3, the optical measurements were recorded with a monochrome CMOS sensor, and absorption increases were measured between the low conductivity state and the state with all electrodes floating. The absorption increases reported in chapter II section D are equal to the difference in pixel intensity from one frame to a later frame. Because the camera was operated in its 8-bit mode, the maximum possible intensity difference for a pixel from one frame to a later frame is 255. In the channel, the maximum pixel value during any test was 177, and the minimum pixel value during any test was 133. Therefore none of the pixels were ever saturated on either the dark end or bright end of the range.

Image processing

To reduce measurement noise, we used both spatial and temporal averaging. For a given frame (that is, a given moment in time), the absorption difference at a distance x from the source was obtained by averaging the intensity differences of all of the pixels in the sensor column imaging a distance x from the source. Additionally, we averaged all of the column averages over a span of 101 frames, or about 2 s. The averaging scheme is described in Figure VII-2. Note that although one edge of the channel is closer to the gate than the opposite edge, averaging across the channel is justified because there is very little variation in color in the direction perpendicular to the channel, as shown in Figure VII-2c. The lack of variation in this perpendicular direction is because the electrolyte is conductive enough that the whole electrolyte gel is at an equipotential. The field lines in the electrolyte are normal to the electrolyte/channel interface. Evidence for this

can be found by noting that in planar OECTs, changing the distance between the gate and channel has no effect on the device behavior.¹³¹

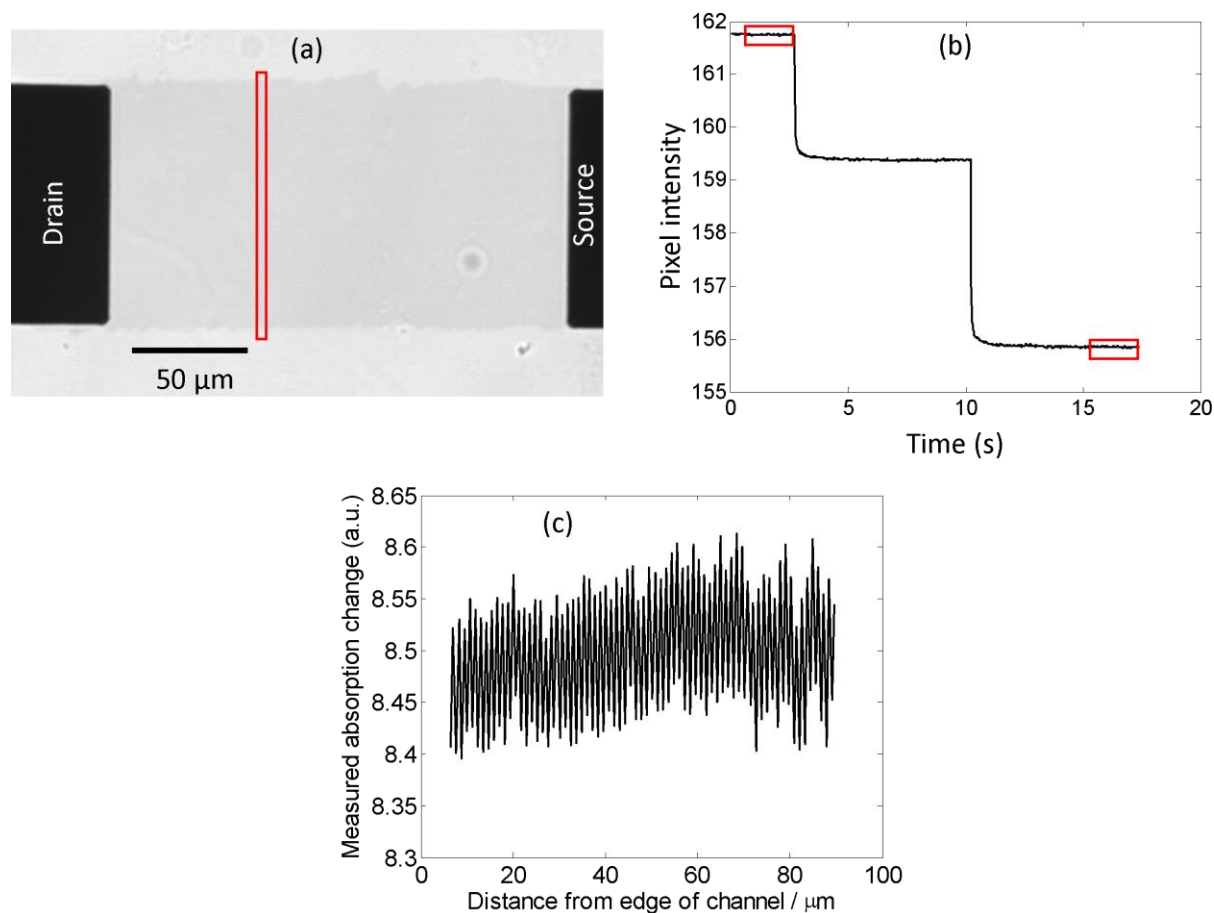


Figure VII-2. (a) Image of the OECT channel showing a slice across the channel. The red box indicates the pixels that are averaged to give an intensity value a distance x away from the source electrode. (Note the box is made wider than one pixel column so that it is easier to visualize. Actual spatial averaging was performed over single pixel columns.) (b) The average intensity over each frame is plotted as a function of time. The first step is the floating electrode state; the second step is the high conductivity state ($V_G = 0$ V); and the third step is the low conductivity state ($V_G > 0$ V). Again, the red boxes indicate which frames are averaged together for our temporal averaging. (c) Measured absorption increase profile in the direction perpendicular to the channel.

In addition to averaging, we also cropped two defective regions out of the images before doing further image analysis. The cropped regions are shown in Figure VII-3. Although significant portions of the image are cropped out, this does not affect the primary results of our

study. The primary results obtained from the uncropped images are shown in Figure VII-4. We only cropped these images because otherwise noticeable bumps appear in individual intensity profiles, as shown in Figure VII-3b.

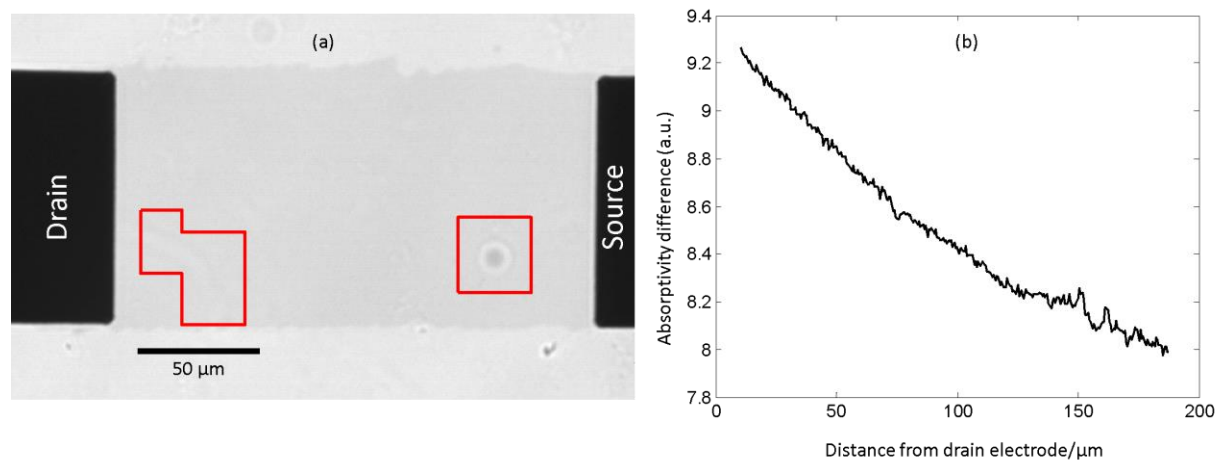


Figure VII-3. (a) OECT channel with the perimeters of the cropped regions shown in red. (b) Absorption profile for the uncropped image with $V_G = 400$ mV and $V_D = -50$ mV. We note that there are the significant bumps at ~ 150 μm.

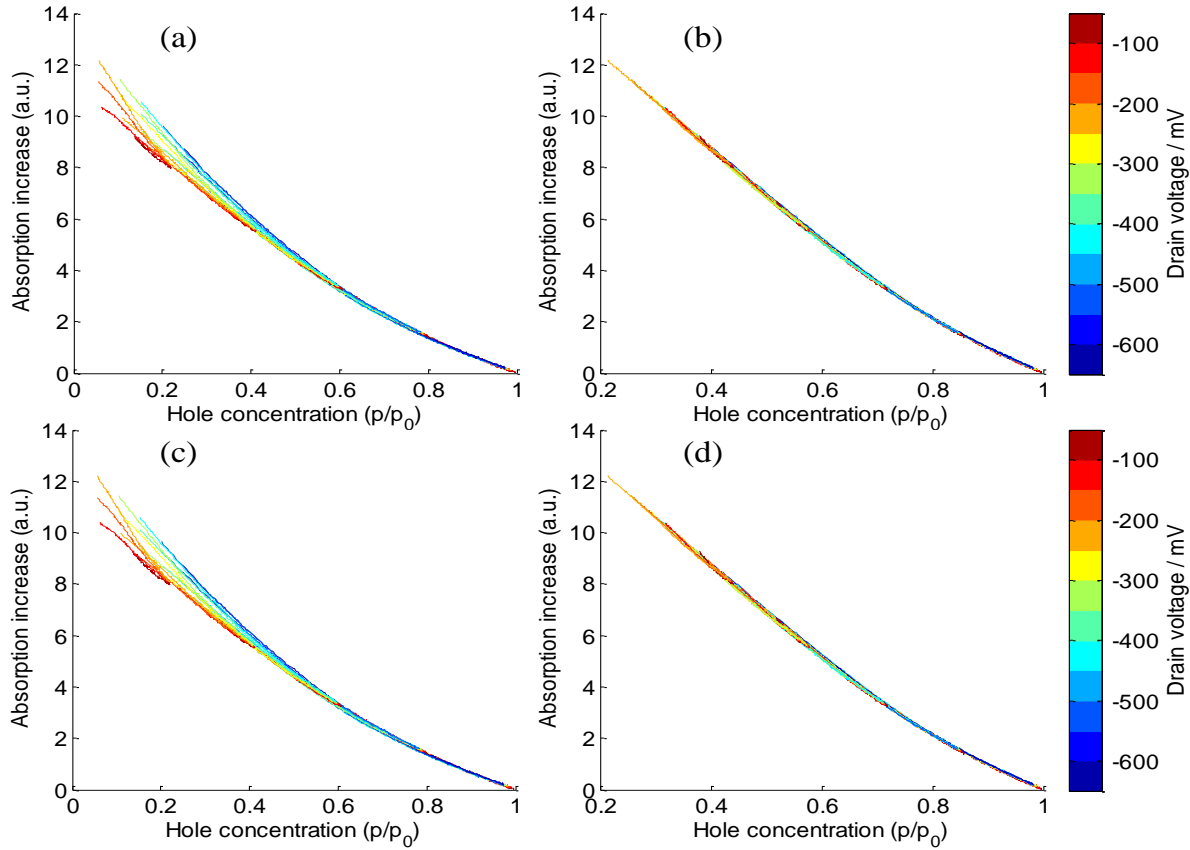


Figure VII-4 Measured absorption increase vs. predicted hole concentration. (a) and (b) are obtained using the cropped images. (c) and (d) are obtained using the uncropped images. In (a) and (c), the hole concentration is predicted by using the Bernards-Malliaras model. In (b) and (d), the hole concentration is predicted using the power law dependence of mobility on hole concentration, $\mu(p) = \mu_0 \times \left[\frac{p}{p_0} \right]^{\frac{E_0}{kT} - 1}$.

Finally, in Figure VII-5, we provide raw images of the OECT channel both in the floating electrode and the low conductivity state. Although no cropping or averaging has been applied to these figures, it is clear that the channel is darker in the low conductivity state. Furthermore, one can discern that the channel is darker near the drain electrode on the left side of the image than it is near the source electrode on the right side of the image. These images (and others) are available in portable graymap format upon request from the author.

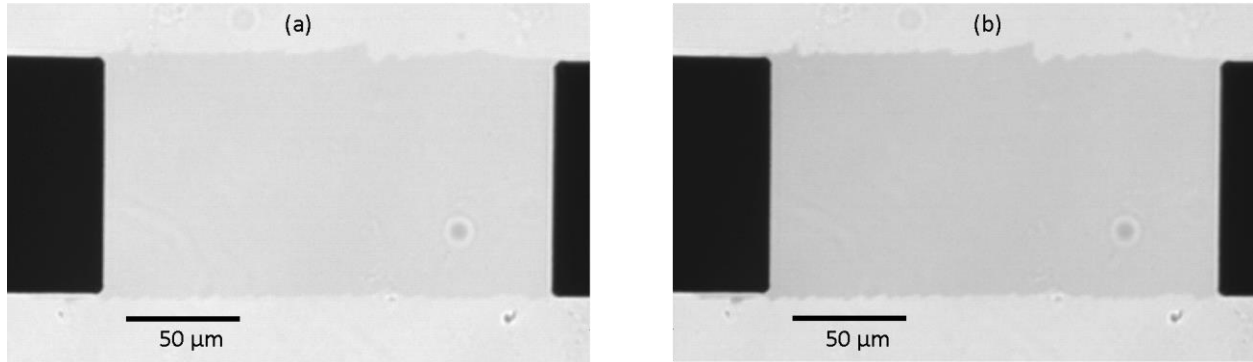


Figure VII-5. Raw images of the OEET channel during the floating electrode state (a) and the low conductivity state with a drain voltage of -200 mV and a gate voltage of 400 mV (b). In (b), the drain voltage is applied at the left electrode while the electrode on the right is grounded.

2. Modifications to the Bernards-Malliaras model

Channel length modulation

To correct for channel length modulation (CLM), we use the same correction typically used for long-channel field-effect transistors.²⁰⁹ We assume that when $V_D < V_G - V_P$, the channel current takes the form below:

$$I_{Dsat} = I_{Dsat0} \times [1 + \lambda[V_{Dsat} - V_D]], \text{ for } |V_D| > |V_{Dsat}| \quad (\text{VII.1})$$

where

$$I_{Dsat0} = \frac{-GV_P}{2} \left(1 - \frac{V_G}{V_P}\right)^2 \quad (\text{VII.2})$$

is the saturation current in the absence of CLM, and $V_{Dsat} = V_G - V_P$ is the drain voltage at the onset of the saturation regime. Once we have extracted G and V_P from the I - V curves for a single assumed value of λ , the CLM parameter, we can use the Bernards-Malliaras model to predict the hole concentration along the channel. To do this, we assume that the most negative voltage along the channel is pinned at V_{Dsat} but moves toward the source electrode, effectively shortening the channel.²⁰⁹ The amount the channel is shortened is given by the ratio I_{Dsat}/I_{Dsat0} as described in equation (VII.3).

$$\frac{I_{Dsat}}{I_{Dsat0}} = 1 + \lambda[V_{Dsat} - V_D] = \frac{L}{L - \Delta L} \quad (\text{VII.3})$$

where L is the physical channel length and $L - \Delta L$ is the effective channel length due to CLM.

The results for four different values of λ are shown in Figure VII-6. It is clear that as λ is increased above $\lambda = 0.45$, the CLM model overcorrects for the lack of a one-to-one fit. This trend is further supported in Figure VII-7, where we plot the spread in predicted hole density ratios as a function of λ at measured absorption increases of 6, 8, and 10 counts.

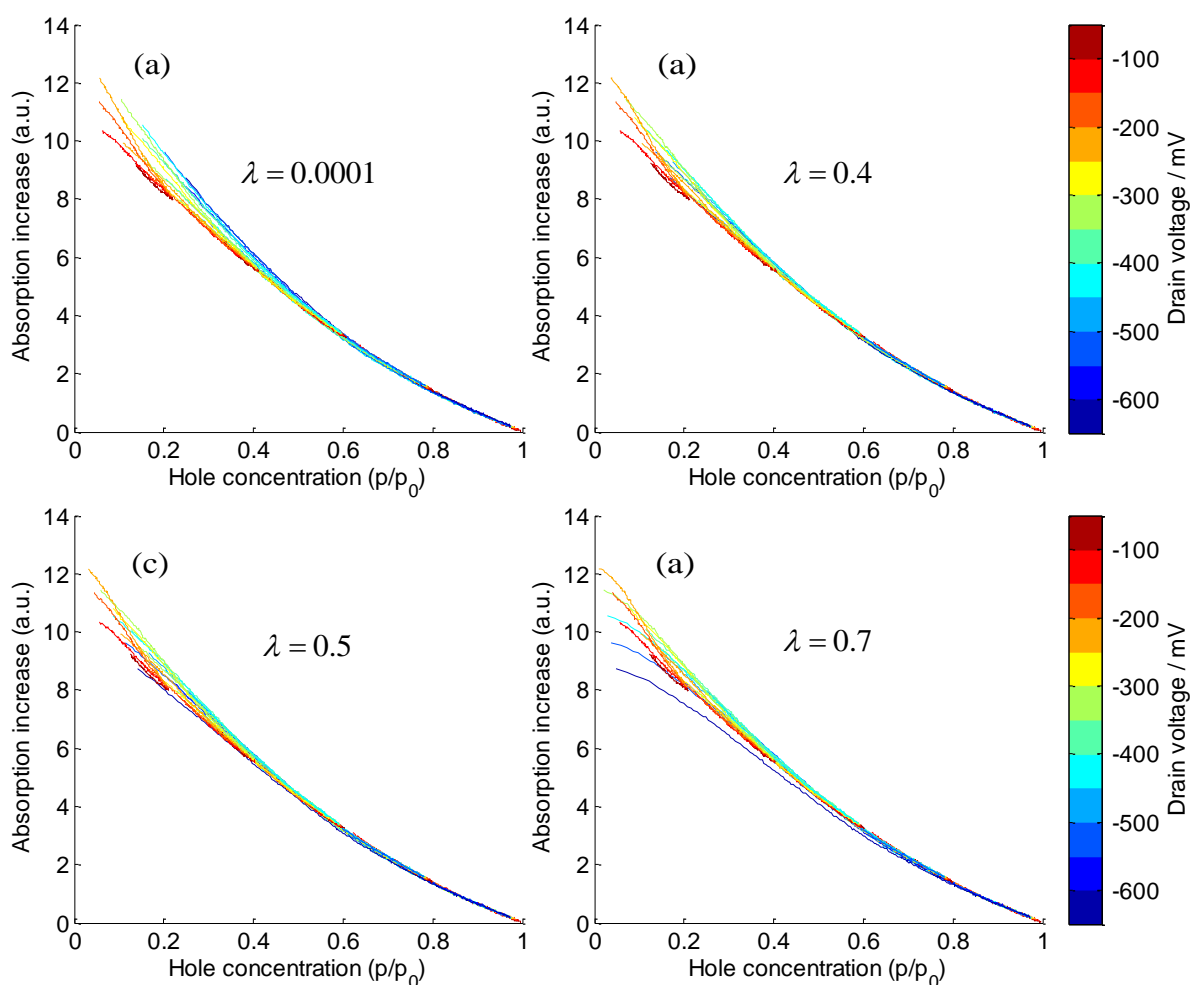


Figure VII-6 Measured absorption increase versus the hole concentration predicted by the CLM model with different values of the CLM parameter λ .

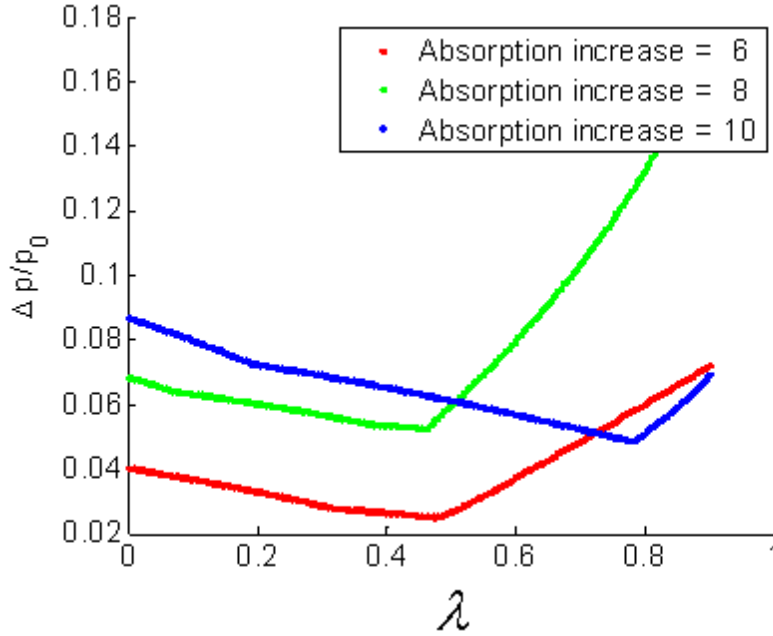


Figure VII-7. This figure shows the range of predicted hole ratio values at a given absorption increase as a function of the CLM parameter, λ . This figure is constructed by drawing a horizontal line across one of the images in Figure VII-6. The horizontal distance between the rightmost curve the horizontal line crosses and the leftmost curve that it crosses is $\Delta p/p_0$. When the model prediction yields a one-to-one relationship between hole concentration and absorption, $\Delta p/p_0 = 0$.

Contact resistance

To correct for a possible contact resistance between the gold source and drain electrodes and the PEDOT:PSS channel, we assumed that the contact resistance at both the source and the drain was equal to R_C . Then, for a negative applied drain voltage and a negative drain current, the voltage at the edge of the source electrode will be $V(x = 0) = IR_C$, and the voltage at the edge of the drain electrode will be $V(x = L) = V_D - IR_C$. Keeping all other assumptions the same as in the Bernards-Malliaras model, the current-voltage relationship for the contact resistance model can be found analytically using the same strategy.

$$J = q\mu p_0 \left[1 - \frac{V_G - V(x)}{V_P} \right] \frac{dV}{dx}$$

(VII.4)

$$JL = \int_{V_G - IR_C}^{V_G - [V_D - IR_C]} q\mu p_0 \left[\frac{u(x)}{V_P} - 1 \right] du$$

where $u(x) \equiv V_G - V(x)$. This integration gives:

$$I = \frac{G[V_D^2 - 2V_GV_D + 2V_PV_D]}{2V_P + 4V_P R_C G + G R_C [2V_D - 4V_G]} \quad (\text{VII.5})$$

for the linear regime. The applied drain voltage at which saturation occurs is given by finding the minimum of this term. Doing so, we find

$$V_{D,sat} = \frac{2R_C G V_G - V_P [1 + 2R_C G] + \sqrt{V_P^2 - 2R_C G V_P [V_G - V_P]}}{R_C G} \quad (\text{VII.6})$$

As we did with the CLM model and the power law mobility model, once we find the current for a given set of gate and drain voltages, we can integrate from $x' = 0$ to $x' = x$ rather than $x' = 0$ to $x' = L$ in order to find the voltage along the channel as a function of position. Doing so, we obtain a quadratic expression for u . After solving for u , we can obtain the hole concentration as a function of position by inserting u into equation (II.3).

The result of varying the contact resistance on the spread of predicted hole concentrations for a fixed absorption increase is shown in Figure VII-8. This shows that even if we allow the contact resistance to reach the same order of magnitude as the channel resistance, the best results are obtained for the zero contact resistance case.

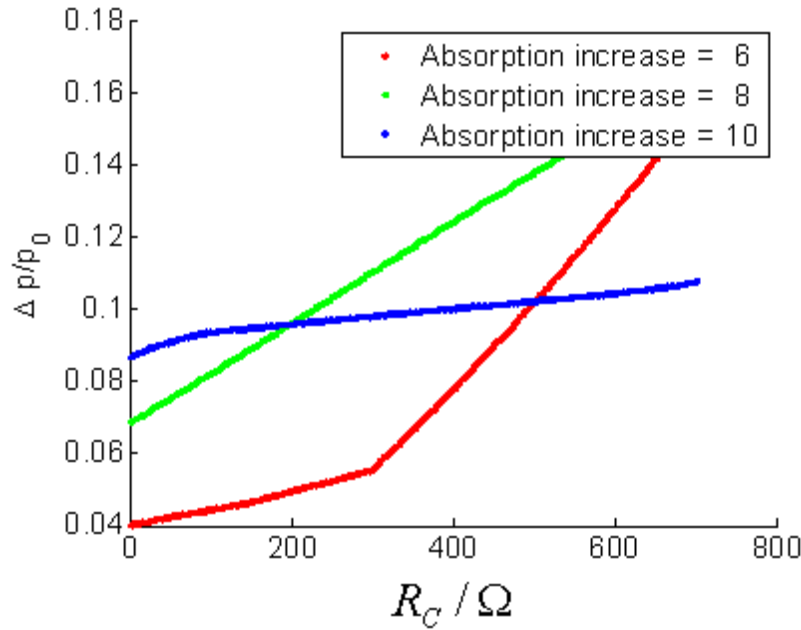


Figure VII-8. This figure shows the range of predicted hole ratio values at a given absorption increase as a function of the contact resistance.

Voltage-dependent capacitance

It has been shown that electric double layer capacitors can have capacitances that increase with voltage.^{210,211} One possible form for such a dependence is $c = c_0 + kV$.²¹¹ The ionic capacitance may take a similar form in an OECT, where V is the voltage between the gate and the channel. Making this assumption, one obtains

$$p(x) = p_0 \left[1 - \frac{u(x)}{V_P} - \kappa [u(x)]^2 \right] \quad (\text{VII.7})$$

where $V_P \equiv \frac{p_0 q T}{c_0}$ and $\kappa \equiv \frac{k}{p_0 q T}$.

Using the same strategy to find the current-voltage relationship predicted by this model and the hole concentration as a function of distance, we obtain

$$I = G \left[\left[\frac{(V_G - V_D)^2}{2V_P} + \frac{\kappa(V_G - V_D)^3}{3} - [V_G - V_D] \right] - \left[\frac{V_G^2}{2V_P} + \frac{\kappa V_G^2}{3} - V_G \right] \right] \quad (\text{VII.8})$$

and

$$\frac{\kappa u^3}{3} + \frac{u^2}{2V_P} - u + V_G - \frac{\kappa V_G^2}{3} - \frac{V_G^2}{2V_P} - \frac{Ix}{GL} = 0 \quad (\text{VII.9})$$

Equation (VII.9) is a cubic equation that can be solved analytically for u . The result can be substituted into Equation (VII.7) to obtain the hole concentration as a function of position along the channel. From the results shown in Figure VII-9, we can see that a voltage-dependent capacitance cannot improve the spread of predicted hole concentration ratios even as k is allowed to increase above c_0 .

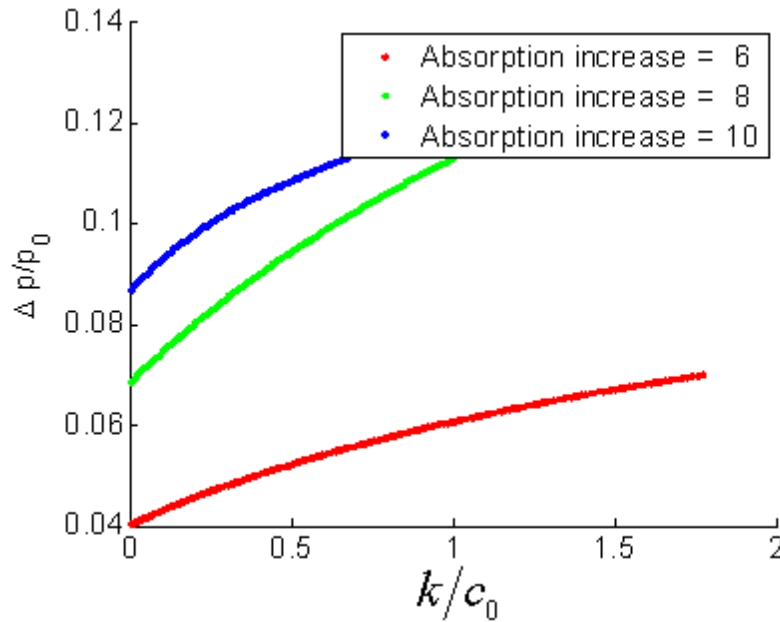


Figure VII-9. This figure shows the range of predicted hole ratio values at a given absorption increase as a function of the ratio of the voltage dependent capacitance coefficient, k , to the constant capacitance coefficient, c_0 .

Power law dependence of mobility on hole concentration

The details of this model are provided in the body of the paper. In Figure VII-10 we show the effects of varying the disorder parameter so that this model can be compared to the ones described above.

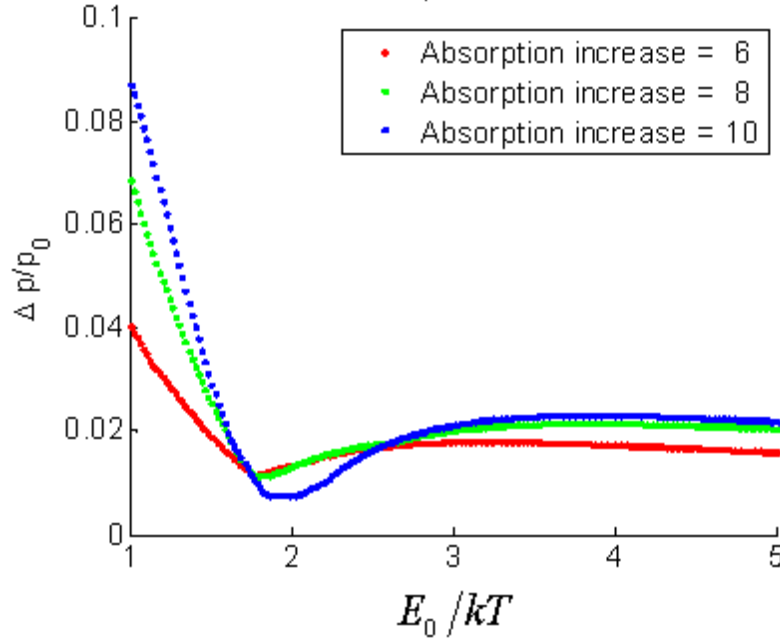


Figure VII-10. This figure shows the range of predicted hole ratio values at a given absorption increase as a function of disorder parameter E_0/kT .

Exponential dependence of mobility on hole concentration

The final model we tested had no physical basis, but we wanted to test whether the power-law dependence of mobility on hole concentration was better than other possible relationships. For this model, we assumed that the mobility is given by

$$\mu = \mu_0 \exp\left(\frac{bp}{p_0}\right). \quad (\text{VII.10})$$

The current-voltage relationship for this model is

$$I = \frac{\exp\left(b\left[1 - \frac{V_G}{V_P}\right]\right) G \left[bV_G + V_P[1-b] + \exp\left(\frac{bV_D}{V_P}\right) [b[V_D - V_G + V_P] - V_P] \right]}{b^2}, \quad (\text{VII.11})$$

and the hole concentration must be solved for numerically.

As shown in Figure VII-11, this model is an improvement over the Bernards-Malliaras model, and is comparable to the model using a power law dependence of mobility on hole concentration, as indicated by the similar shapes and magnitudes of the curves in Figure VII-10 and Figure VII-11. In fact at an absorption difference of 10, the exponential model is slightly

better. Therefore, we cannot say which of these two models fits the data better. However, we prefer the power law dependence because of its physical basis (and ability to be solved analytically).

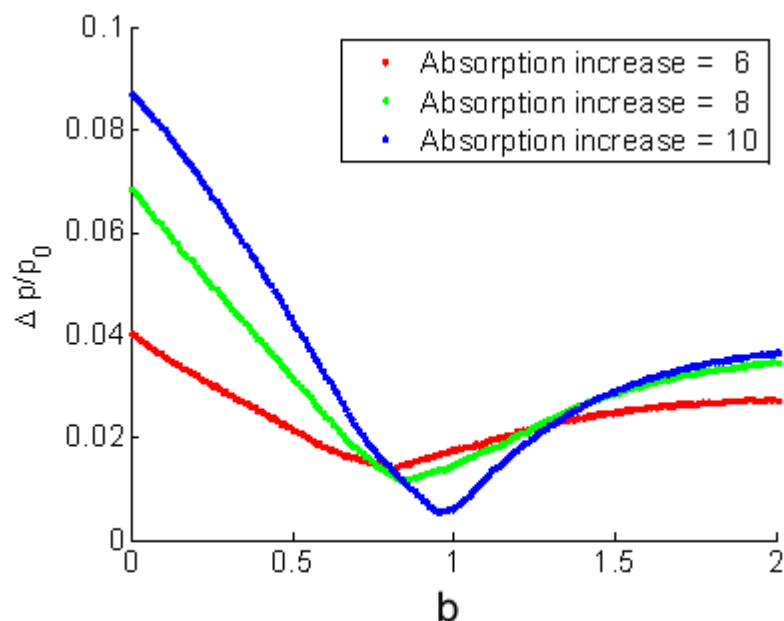


Figure VII-11. This figure shows the range of predicted hole ratio values at a given absorption increase as a function of the unitless parameter, b , appearing in the exponential dependence of mobility on hole concentration.

3. Transient electrical response

The transient electrical response of a typical gel-electrolyte OECT is shown in Figure VII-12. A single exponential is fit to the “elbow” region of this curve between 0 s and 0.5 s, yielding a time constant of 28.5 ms. We note however, that the curve displays a slowly decaying tail that extends for the full 7.5 s of measurement. We are not sure what causes this slow decay, but many other devices in the literature show a similar response.^{26,65–67,108,166} Some authors speculate that the slow decay following a fast turn-on is due to “rearrangement of conjugated polymer chains” or “bias stress/trap filling”.¹⁰⁸ The gate current is shown in Figure VII-13,

where it is clear that, except for a brief spike at the initial voltage step, the gate current is 3 orders of magnitude smaller than the drain current.

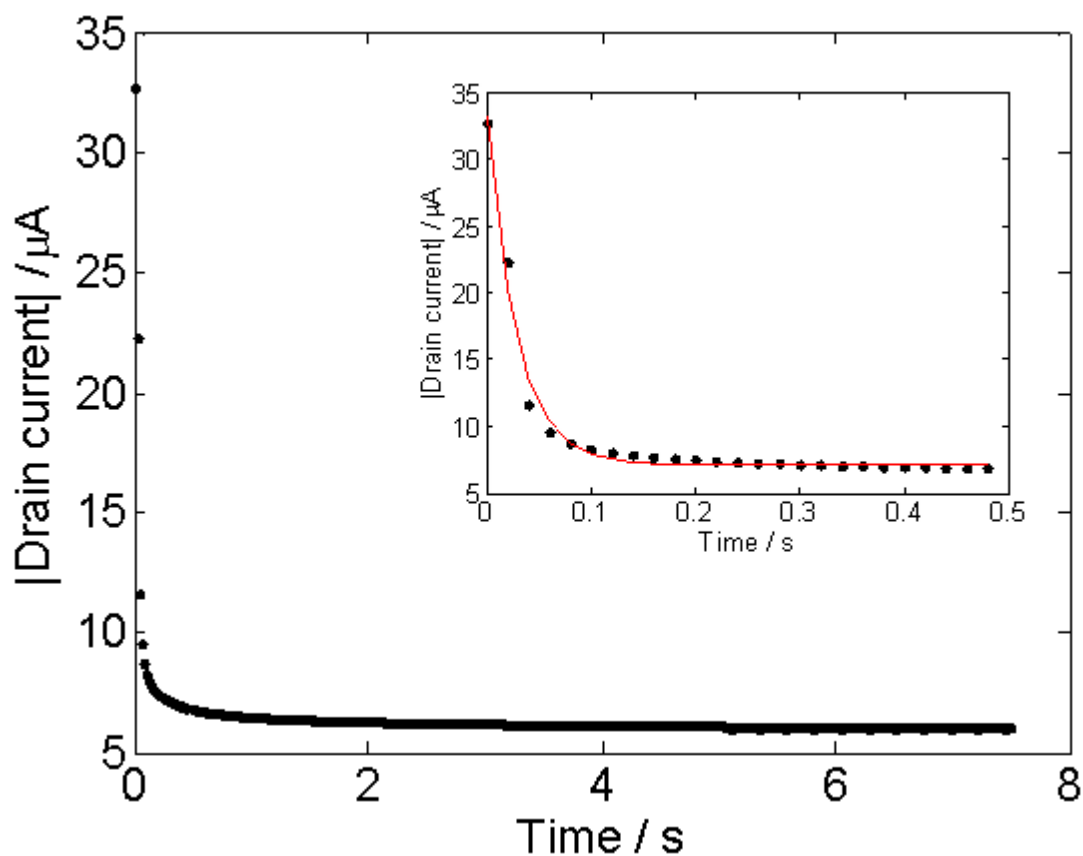


Figure VII-12. Typical transient electrical response of an OECT after the application of a positive gate voltage. This response is obtained with a drain voltage of -50 mV and a gate voltage stepped from 0 V to 400 mV. The inset shows the “elbow” region of the curve where the data (black points) were fit to a single exponential (red line).

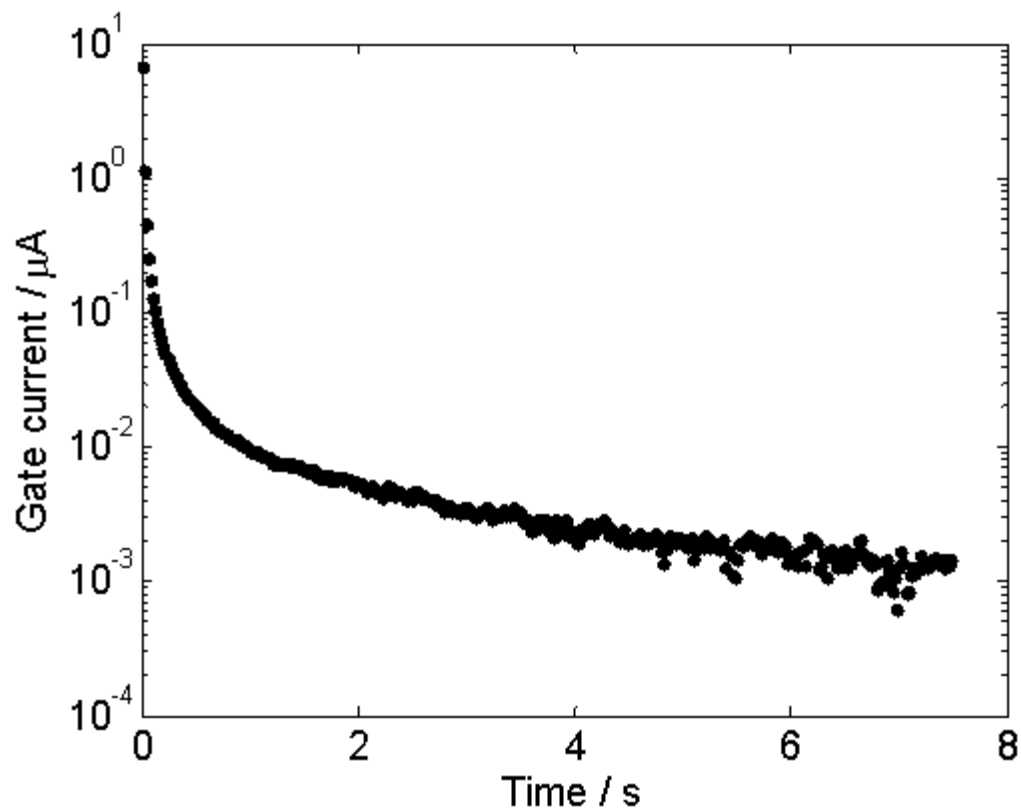


Figure VII-13. Typical transient electrical response of a gel-electrolyte OECT after the application of a positive gate voltage. This response is obtained with a drain voltage of -50 mV and a gate voltage stepped from 0 V to 400 mV.

The transient electrical response of a typical liquid-electrolyte OECT is shown in Figure VII-14. After fitting to a single exponential, we find the time constant of this device is approximately 79 μs . Notice that the liquid electrolyte OECTs are much faster than the gel-electrolyte devices.

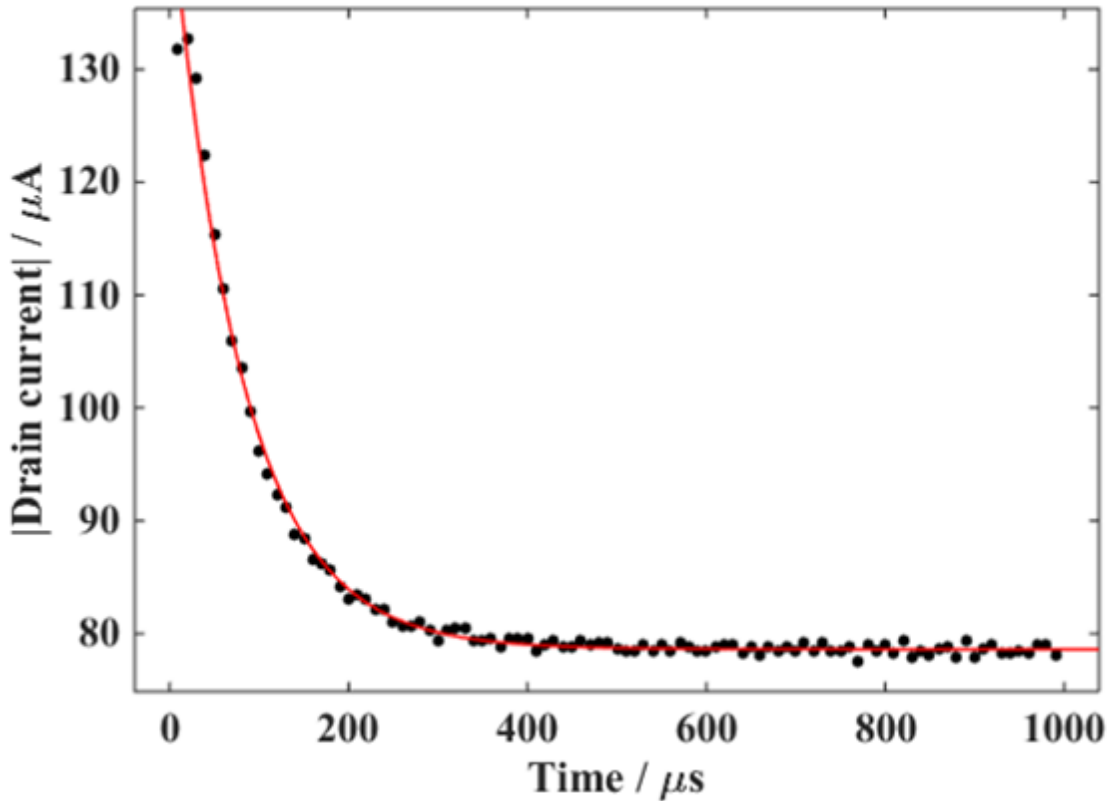


Figure VII-14. Typical transient electrical response of a liquid-electrolyte OECT after the application of a positive gate voltage. This response is obtained with a drain voltage of -100 mV and a gate voltage of 100 mV. The data (black points) are fitted to a single exponential (red line).

4. Calculation of expected transconductance

Differentiating equation (II.6) and (II.7) with respect to V_G at constant V_D yields

$$g \equiv \left(\frac{\partial I_D}{\partial V_G} \right)_{V_D} = \left\{ \begin{array}{ll} G \times \left[\left(\frac{V_P - V_G}{V_P} \right)^{\frac{E_0}{kT}} - \left(\frac{V_D - V_{D,sat}}{V_P} \right)^{\frac{E_0}{kT}} \right], & \text{for } V_D > V_{D,sat} \\ G \times \left(\frac{V_P - V_G}{V_P} \right)^{\frac{E_0}{kT}}, & \text{for } V_D < V_{D,sat} \end{array} \right\}. \quad (\text{VII.12})$$

In the saturation regime, g is independent of V_D . However, in the linear regime, we can see that g depends monotonically on V_D . To see this, take the derivative of Equation (VII.12).

$$\left(\frac{\partial g}{\partial V_D}\right)_{V_G} = -\frac{GE_0}{V_P kT} \left[\frac{V_D - V_{D,sat}}{V_P}\right]^{\frac{E_0}{kT} - 1} \quad (\text{VII.13})$$

As long as $V_D > V_{D,sat}$ and $V_P > 0$, this derivative is negative, meaning that as V_D is made less negative, g decreases.

Figure VII-15 shows a linear fit to the measured absorption increase as a function of the calculated hole concentration.

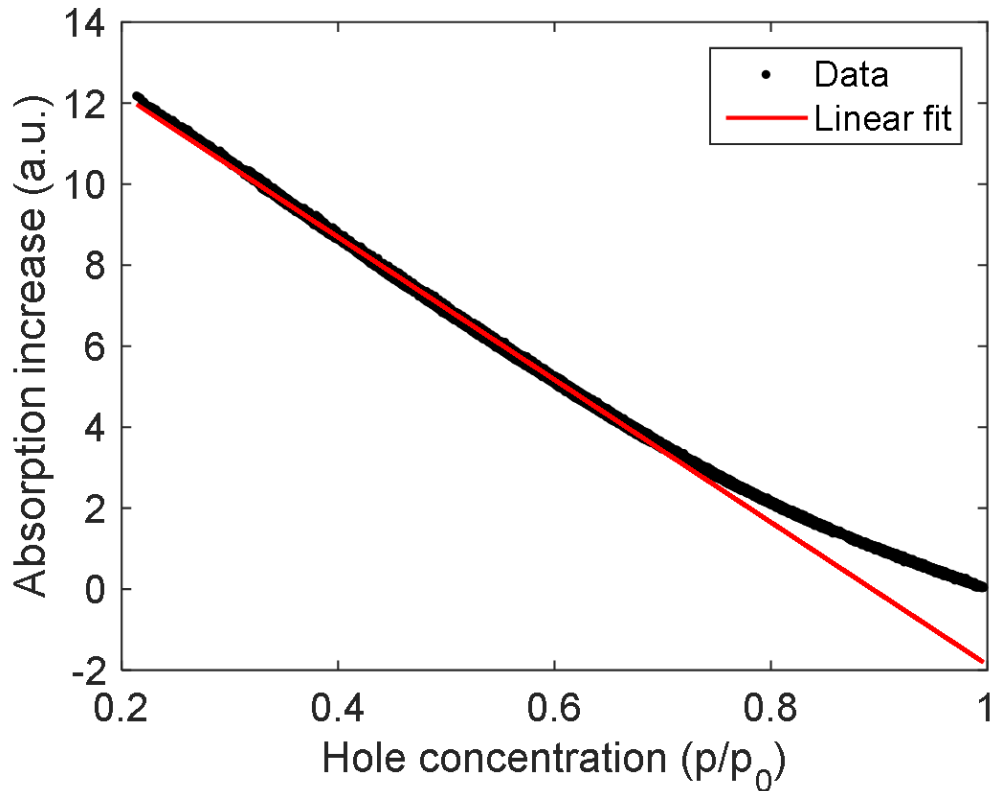


Figure VII-15. This figure shows a linear fit to the data displayed in Figure II-9. The linear fit yields $\gamma = a \times \left[1 - \frac{p}{p_0}\right] + b$, where γ is the optical absorption, and p/p_0 is the ratio of the hole concentration to the zero-field hole concentration. The extracted parameters are $a = 17.6$ and $b = -1.87$, both in arbitrary units.

APPENDIX II: SUPPORTING MATERIAL FOR CHAPTER III

A. Derivation of the disorder model

The disorder model proposed in chapter III is based on the percolation theory of Ambegaokar, Halperin, and Langer (AHL).¹⁴⁴ The primary theorist behind the model described below was David Dunlap, but I also helped develop the theory and test the model. Below we give an explanation of our implementation of this theory.

The AHL theory considers the connections between hopping sites to be conductances. The conductance between two sites with energy ε_i and ε_j is given by

$$g_{i,j} = n_i[1 - n_j]\gamma_{i,j}.$$

where $g_{i,j}$ is the conductance between sites i and j , n_i is the occupation number for site i , and $\gamma_{i,j}$ is the transition rate for hopping from site i to site j . As discussed in AHL, detailed balance ensures that $g_{i,j} = g_{j,i}$. By combining equations 3.2, 3.3, and 3.6 from AHL, one obtains the following expression for conductance between sites i and j

$$g(\varepsilon_i', \varepsilon_j') = \frac{2g_{\max}\exp\left(-\frac{1}{2}\beta|\varepsilon_j' - \varepsilon_i'\right)}{\cosh\left(\frac{1}{2}\beta[\varepsilon_j' - \varepsilon_i']\right) + \cosh\left(\frac{1}{2}\beta[\varepsilon_j' + \varepsilon_i']\right)}. \quad (\text{VIII.1})$$

For simplicity we have assumed the Miller-Abrahams form of detailed balance;¹⁴⁵ uphill hops are thermally activated, while downhill hops are independent of the site energies. We have assumed that all carriers are sufficiently localized and/or temperature is sufficiently high that variable range hopping beyond nearest neighbor sites is negligible compared to nearest-neighbor hopping. We have defined $\beta \equiv 1/(kT)$ with $k \equiv$ the Boltzmann constant and $T \equiv$ the temperature. We have introduced the primed notation so that $\varepsilon' \equiv \varepsilon - \mu$ is the difference between the site energy and the Fermi level, μ . The factor g_{\max} is the maximum possible conductance between two sites. Two sites will be connected with conductance g_{\max} if both site

energies are at the Fermi level. Notice that in the limit of small kT , equation (VIII.1) in the present work reduces to equation 3.7 from AHL except for the dimensions of the prefactor, which is g_{\max} for conductance here and γ_0 for hopping rate in AHL 3.7. The spatial dependence in AHL equation 3.7 does not occur in our equation (VIII.1) because we only consider nearest-neighbor hopping in a uniform lattice. Finally, we note that the expression for non-equilibrium conductance between sites in AHL (equation AHL 4.4) is proportional to the hopping rate in AHL 3.7; therefore, our equation (VIII.1) agrees with the conductance expression in AHL.

Continuing toward the calculation of sample conductivity, let us introduce dimensionless energies x and y :

$$x = \frac{1}{2}\beta[\varepsilon_1' + \varepsilon_2']$$

$$y = \frac{1}{2}\beta[\varepsilon_1' - \varepsilon_2']$$

so that we can rewrite equation (VIII.1) as follows:

$$g(x, y) = \frac{2g_{\max}\exp(-|y|)}{\cosh(y) + \cosh(x)} \quad (\text{VIII.2})$$

Now, the argument from AHL is that the lowest conductances do not participate in forming a percolating network. One just needs to consider all of the conductances between the maximum, g_{\max} , and some minimum, g_{\min} . Setting $g(x, y) = g_{\min}$, and using equation (VIII.2) yields

$$\frac{g_{\min}}{g_{\max}} = \frac{2\exp(-|y|)}{\cosh(y) + \cosh(x)} \equiv r \quad (\text{VIII.3})$$

for some values of x and y , where we have defined r to be the ratio of the minimum conductance in the percolation cluster to the maximum possible conductance.

Using (VIII.3), we can define a value y_{\max} such that if $y > y_{\max}$, then $g(x, y)$ will be less than g_{\min} . This definition is given below:

$$r = \frac{2\exp(-|y_{\max})}{\cosh(y_{\max})+1} \quad (\text{VIII.4})$$

Next, we define a relationship $x_{\max}(y)$ such that if $-x_{\max}(y) < x < x_{\max}(y)$ and $y < y_{\max}$, then $g(x, y)$ will be greater than g_{\min} . This relationship is defined below.

$$r = \frac{2\exp(-|y|)}{\cosh(y)+\cosh(x_{\max})} \quad (\text{VIII.5})$$

Then we integrate over all possible connections between hopping sites (the density of states at energy ε_i multiplied by the density of states at ε_j for all i and j) to get the fraction η of possible connections that must have $g > g_{\min}$ in order form a connected percolation cluster spanning the system. We have

$$\eta = 2(kT)^2 \int_{-y_{\max}}^{y_{\max}} dy \int_{-x_{\max}(y)}^{x_{\max}(y)} dx \rho(kT[x+y]+\mu) \rho(kT[x-y]+\mu) \quad (\text{VIII.6})$$

where y_{\max} is given by (VIII.4), and $x_{\max}(y)$ is given by (VIII.5). These values for the limits of integration are chosen so that we integrate over all bonds with conductance greater than g_{\min} but do not integrate over any bonds with conductance less than g_{\min} . The prefactor $2(kT)^2$ comes from the Jacobian for converting the integral over energy to an integral over x and y . The density of states (DOS), ρ , is normalized with respect to the volume such that when integrating over all energies, the result is 1. In our implementation, we chose to model the DOS as a single Gaussian. Although this choice of DOS function is simpler than that expected in doped semiconductors,¹⁵² we chose to use a Gaussian because it only introduces two free parameters to the model, and it is justified in materials with electronic coupling between charge carriers and randomly aligned – or partially correlated – dipoles.²¹² Therefore, the volume-normalized DOS for our model is

$$\rho(E) = \frac{1}{\sqrt{2\sigma^2\pi}} \exp\left(-\frac{[E-E_0]^2}{2\sigma^2}\right)$$

where σ is the width of the DOS, E is the energy of an electron in the DOS, and E_0 is the energy of the center of the DOS peak with respect to Ag/AgCl.

To solve for sample conductivity, we input material parameters σ , E_0 , and η , then numerically solve equation (VIII.6) for y_{\max} . Once we have y_{\max} , we can find the minimum conductance in our percolation network according to the following equation, which comes from equation (VIII.4).

$$g_{\min} = g_{\max} \frac{2\exp(-|y_{\max}|)}{\cosh(y_{\max})+1}$$

We can understand the conductance g_{\min} as representing the maximum resistance hop along the minimum resistance path through our network. Therefore, according to the arguments from AHL about percolation transport, g_{\min} will characterize the macroscopic conductivity of the sample. The sample conductivity will be proportional to g_{\min} where the proportionality constant is determined by sample geometry.¹⁴⁴ In agreement with previous work, we implement this conductivity model for OECTs by assuming that the Fermi-level of electrons in the semiconductor is given by $\mu = qV_G$, where μ is the Fermi-level in the film with respect to Ag/AgCl, q is the elementary charge, and V_G is the gate voltage.^{121,122} Therefore, changing the gate voltage shifts the Fermi-level of the semiconductor in the OECT channel. In OECTs, Fermi-level shifts are manifested by the introduction or removal of ionic dopants. In p-type depletion-mode OECTs, positive gate voltages force cations into the semiconductor channel where they compensate native dopants and cause a decrease in conductivity. In p-type accumulation-mode OECTs, negative gate voltages force anions into the semiconductor channel where they provide a counter charge for holes on the polymer backbone, thus causing an increase in conductivity. The model presented here takes into account the effect these dopants have on the Fermi-level (and thus carrier concentration) in the semiconductor channel. However, this model neglects secondary effects of the dopants, such as coulombic and steric interactions between charge

carriers and dopants. These secondary effects can often be accounted for by assuming an appropriately modified DOS.^{151,152}

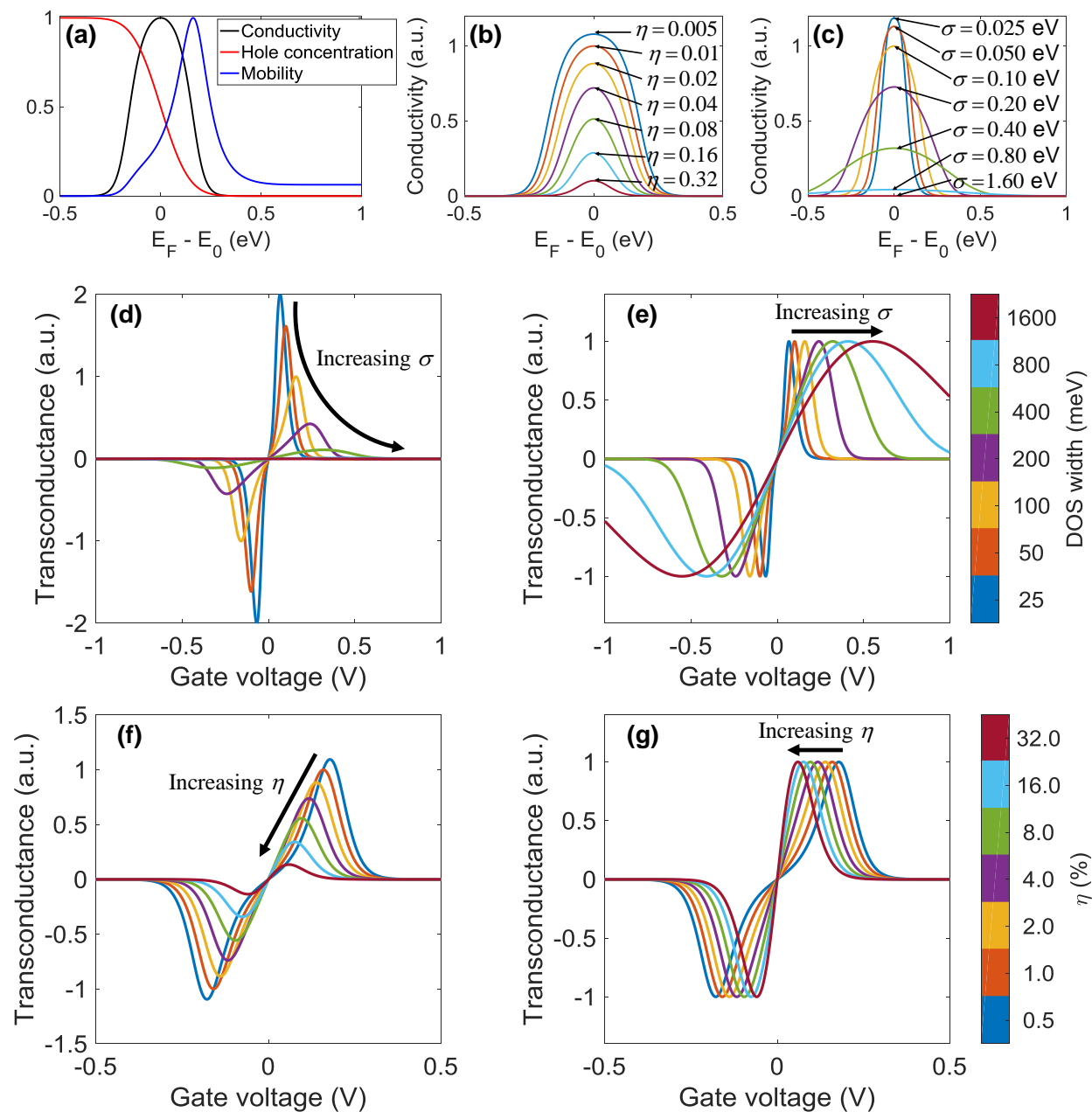


Figure VIII-1. Disorder model for OECTs. (a) Conductivity, total hole concentration, and effective mobility (defined as conductivity divided by total hole concentration) for a disordered semiconductor according to the disorder model. The horizontal axis is the Fermi level of electrons minus the energy at the peak of the DOS. All curves in (a) are normalized so that their global maximum is 1. In (a), the DOS standard deviation is 100 meV and the percolation fraction is 0.01. (b) Effect of changing percolation fraction on the conductivity vs. Fermi-level relationship. The standard deviation of the DOS is 100 meV for all curves in (b). (c) Effect of

changing DOS variance on the conductivity vs. Fermi-level relationship. The percolation fraction is 0.01 for all curves in (c). In (b) and (c), all curves are normalized to the global maximum of the conductivity when the DOS standard deviation is 100 meV and the percolation fraction is 0.01. (d-g) Dependence of transconductance curves on DOS standard deviation and percolation fraction. In (d) and (f), all curves are normalized to the maximum transconductance of the curve for which the DOS standard deviation is 100 meV and the percolation fraction is 0.01. In (e) and (g), all curves are normalized to their global maximum value. The colorbar shown next to (e) applies to figures (d) and (e). The colorbar next to (g) applies to both (f) and (g). The percolation fraction is 0.01 in figures (d) and (e), and the DOS standard deviation is 100 meV in (f) and (g).

B. Contact resistance measurements.

To calculate the contact resistance in our transistors, we start by finding how much voltage is dropped at the source contact. The source voltage is calculated by extrapolating the voltage profile between the two probes closest to the source, according to equation (VIII.7) below.

$$V_{Source} = \frac{V_2 - V_1}{x_{2L} - x_{1R}} [x_S - x_{1L}] + V_1 \quad (\text{VIII.7})$$

where V_{Source} is the extrapolated source voltage; V_1 is the voltage measured at the probe nearest the source electrode; V_2 is the voltage measured at the probe adjacent to the first probe; $x_S = 0$ is the position of the source electrode; x_{1L} is the position of the left edge of the first voltage probe (assuming the source electrode is to the left); x_{1R} is the position of the right edge of the first voltage probe; and x_{2L} is the position of the left edge of the second voltage probe. See Figure VIII-2 and Figure VIII-3.

The contact resistance at the source electrode is the difference between the applied and actual source voltages divided by the channel current.

$$R_{Source} = \left| \frac{V_{Source,applied} - V_{Source}}{I_{Channel}} \right| \quad (\text{VIII.8})$$

where R_{Source} is the contact resistance at the source electrode; $V_{Source,applied}$ is the voltage applied to the source electrode; and $I_{Channel}$ is the channel current in the transistor.

Because we use a common source configuration for our measurements, $V_{Source,applied} = 0$ and we have

$$R_{Source} = \left| \frac{V_{Source}}{I_{Channel}} \right| \quad (\text{VIII.9})$$

The uncertainty in the extrapolated source voltage is given by

$$\delta V_{Source} = \sqrt{\left[\frac{V_2 - V_1}{x_{2L} - x_{1L}} x_{1L} \right]^2 \left[\left[\frac{\delta V}{V_2 - V_1} \right]^2 + \left[\frac{\delta x}{x_{2L} - x_{1R}} \right]^2 + \left[\frac{\delta x}{x_{1L}} \right]^2 \right] + [\delta V]^2} \quad (\text{VIII.10})$$

where δV_{Source} is the uncertainty in the extrapolated source voltage; δV is the experimental uncertainty in measured voltage; and δx is the experimental uncertainty in the position of the edge of the voltage probes. Once we have the uncertainty in the source voltage, we find the uncertainty in the extracted contact resistance according to equation (VIII.11).

$$\delta R = \sqrt{\left(\frac{\delta V_{Source}}{I_{Channel}} \right)^2 + \left(\frac{V_{Source}}{I_{Channel}^2} \delta I_{Channel} \right)^2} \quad (\text{VIII.11})$$

where $\delta I_{Channel}$ is the uncertainty in the measured channel current and is defined as $\delta I_{Channel} \equiv$

$\frac{1}{2} (\max(I_{Channel}) - \min(I_{Channel}))$ where the channel current was measured five times. The

measurements near the source electrode are shown in Figure VIII-2 and Figure VIII-3.

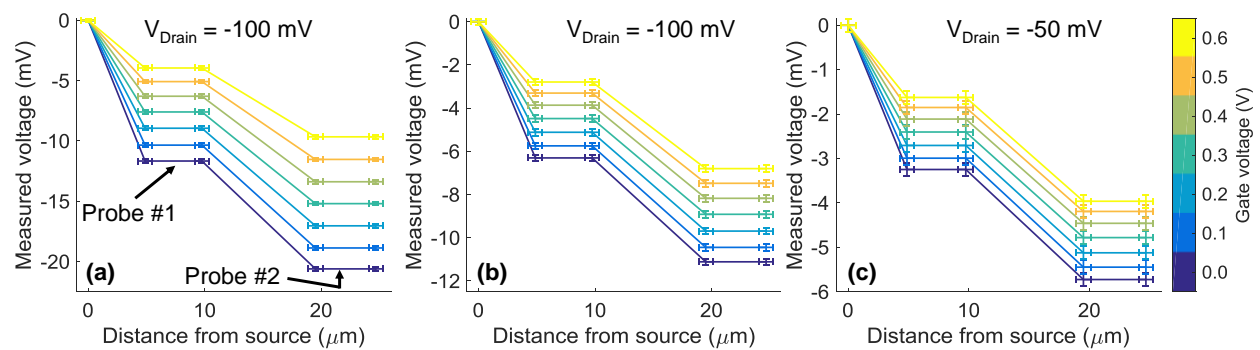


Figure VIII-2. Measured voltage in the channel of a PEDOT:PSS-based OECT. The probes have a width of $\sim 5 \mu\text{m}$. Because we assumed that the voltage is constant across each probe, there are horizontal sections in each graph corresponding to the width of each probe.

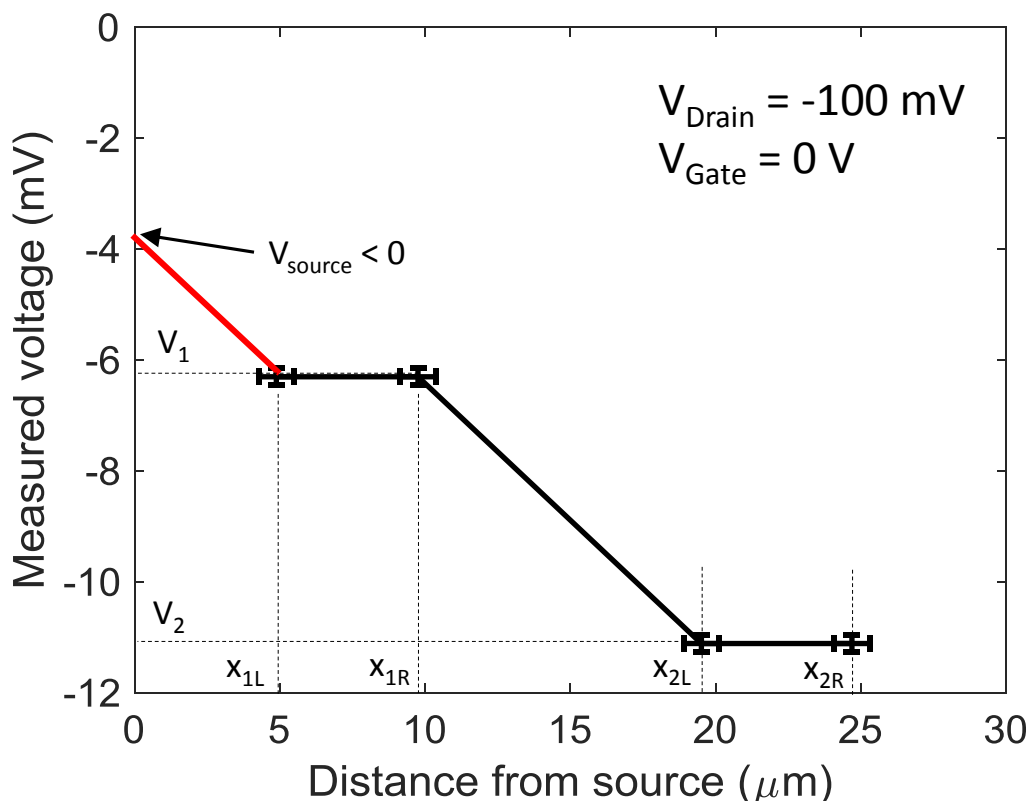


Figure VIII-3. Measured voltage near the source of a PEDOT:PSS-based OEET. The red line shows the extrapolation of the measured data to the source electrode. The offset between the extrapolated source voltage and 0 V is voltage drop due to contact resistance. As in Figure VIII-2, we assume that each voltage probe enforces an equipotential region across its width. Therefore, the voltage profile is horizontal on top of each voltage probe.

The contact resistance can be calculated at the drain contact in the same manner; however, it is not possible to separate the effects of channel depletion and actual contact resistance. Therefore, our method of calculating contact resistance will overestimate the contact resistance because of the curvature of the voltage profile with respect to position in the channel. This effect will be more pronounced at the drain electrode than at the source electrode (because the curvature is stronger at the drain) and will be more pronounced at higher drain voltages. Figure VIII-4 shows the estimated contact resistance at the drain electrode. According to the explanation above, the contact resistances shown in Figure VIII-4 are conservative upper bounds on the actual contact resistances.

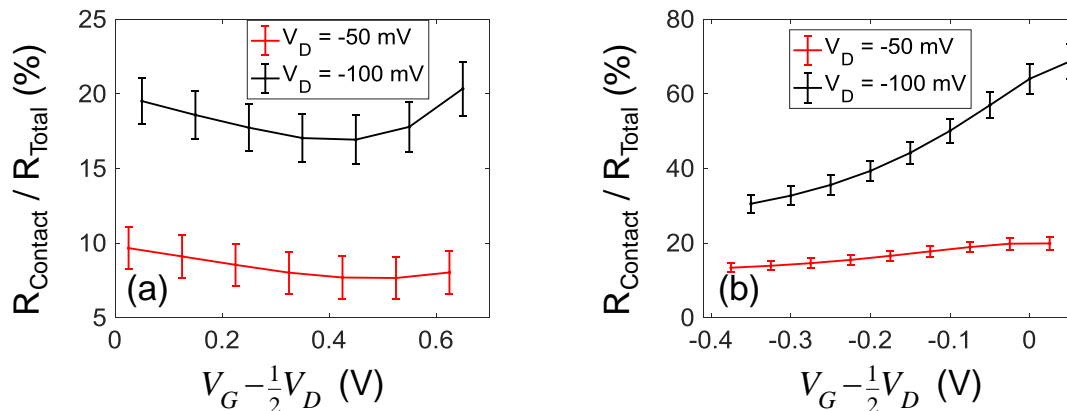


Figure VIII-4. Normalized contact resistance at the drain electrode for (a) a PEDOT:PSS-based OECT and (b) a p(g2T-TT)-based OECT. Note that these curves are known to be overestimates of the contact resistance at the drain electrode.

C. Experimental details:

1. Fabrication

OECTs were fabricated on glass substrates as previously reported.²¹³ Briefly, Cr/Au was photolithographically defined via a liftoff process, followed by deposition of 2 layers of parylene C (PaC) separated by micro-90 antiadhesive (2% in water). The openings of the OECT channels were defined photolithographically using a thick photoresist (AZ9260), and etched before spinning on the active OECT polymer channel material. A subset of devices, including those prepared with voltage probes for 4-wire measurements, were prepared in a similar method but employed a 2 μm layer of silicon oxynitride as the insulation layer, and used a MoCr hard etch mask rather than a thick photoresist. In this case, after metal deposition and patterning, silicon oxynitride was deposited, and photolithographically patterned to open the channel region. Micro-90 was spun on as above, and the sacrificial layer of PaC was deposited. MoCr was deposited and patterned photolithographically before oxygen plasma to etch the sacrificial PaC opening. After etching, the semiconductor was spun-cast onto the sample. For PEDOT:PSS, the

semiconductor solution was 94 wt% Clevios PH-1000, 5 wt% ethylene glycol, 1 wt% 3-glycidoxypropyltrimethoxysilane, and 0.1 wt% dodecylbenzenesulfonic acid. The PEDOT:PSS solution was spun at 3000 rpm, 1500 rpm/s, and 60 s. It was then baked for 70 s at 110 °C. After this initial bake step, the second layer of PaC was peeled off of the sample, patterning the PEDOT:PSS channels according to the process in DeFranco et al.²¹⁴ After peel-off, the sample was baked for 70 minutes at 140 °C and then soaked in deionized water for 13 hours. The p(g2T-TT) solution was 0.12 wt% of p(g2T-TT) dissolved in chloroform. It was spun at 1500 rpm, 1000 rpm/s, and 40 s. The peel-off process for the p(g2T-TT)-based transistor was the same as that for the PEDOT:PSS-based transistor except no baking steps were included. This resulted in an ~ 100 nm thick semiconductor layer for PEDOT:PSS and an ~ 85 nm layer for p(g2T-TT).

2. Characterization

The PEDOT:PSS-based OECT output and transfer curves (Figure III-1c, Figure III-2c, Figure III-3, and Figure III-4a) were made using a Keithley 2612A source meter unit. 4-wire measurements were performed in 4-wire sense mode for channel B and 2-wire sense mode for channel A. The force-hi terminal of channel B was connected to the drain electrode, and the sense-hi terminal was connected to the voltage probe nearest to the drain electrode. The force-lo terminal of channel B was connected to the source electrode, and the sense-lo terminal was connected to the voltage probe nearest to the source electrode. The force-hi terminal on channel A was connected to the Ag/AgCl pellet, and the force-lo terminal was shorted to the sense-lo terminal of channel B. For 2-wire measurements, the force-hi terminal of channel B was connected to the drain electrode, and the force-lo terminal was connected to the source electrode. The force-hi terminal of channel A was connected to the Ag/AgCl pellet, and the force-lo

terminal was shorted to the force-lo terminal of channel B. The output and transfer curves for the p(g2T-TT)-based OECT (Figure III-1d, Figure III-2d, and Figure III-4b) were made using a Keysight B2962 source meter unit. The 4-wire and 2-wire connections for these measurements were the same as those used for the PEDOT:PSS-based OECT.

The contact resistance measurements for the PEDOT:PSS-based OECT were made using a National Instruments PXIe-4145 source meter unit synchronized with a National Instruments PXI 6289 DAQ system. The force-hi terminal of channel 1 of the 4145 was connected to the drain electrode, and the force-lo terminal was connected to the source electrode. The positive voltage output of the 6289 was connected to the Ag/AgCl pellet, and common voltage output was shorted to the force-lo of channel 1 on the 4145. The force-hi terminal of channel 2 of the 4145 was connected to a voltage probe, and the force-lo terminal was shorted to channel 1 force-lo. Channel 1 of the 4145 was configured to source voltage and measure current. Channel 2 of the 4145 was configured to source 0 current and measure voltage. The DAQ was configured to source voltage, but did not measure current. Five measurements were made in total, and channel 2 of the 4145 was placed on a different voltage probe in each measurement. For the p(g2T-TT)-based OECT, the contact resistance measurements were made by using the Keithley tsp-link system to synchronize a Keithley 2450 and a Keithley 2636A. Force-hi of channel A on the 2636 was connected to the Ag/AgCl pellet, and force-lo was connected to the source electrode. Force-hi of channel B was connected to the drain electrode, and force-lo was shorted to force-lo of channel A. Force-hi of the 2450 was connected to a voltage probe, and force-lo was shorted to force-lo of channel A on the 2636. Both channels of the 2636 sourced voltage and measured current. The 2450 sourced 0 current and measured voltage. Five total measurements were made,

and for each, the 2450 was connected to a different voltage probe. In this way, the voltage at each position in the channel was measured.

Before making any measurements the OECTs were cycled on and off for more than five minutes with square voltage pulses at the gate electrode.

3. Data fitting

The disorder model was implemented in MATLAB and used as an objective function for the MATLAB nonlinear curve fitting function `lsqcurvefit`. Parameters were extracted based on the fit between the model's predicted transconductance curve and the experimental transconductance curve. The free parameters in the fitting procedure are E_0 , σ_{DOS} , and η . The conductivity scaling factor, σ_0 , is a fixed value in the fitting procedure and is simply the conductivity when the OECT is biased at $V_G = 0$ V (for PEDOT:PSS) or $V_G = -0.4$ V (for p(g2T-TT)). The uncertainty in the parameters E_0 , σ_{DOS} , and η are based on the estimated covariance matrix for those variables. The reported uncertainties in these variables are 95% confidence intervals obtained using the MATLAB function `nlparci`. For the PEDOT:PSS-based OECT, the reported uncertainty in the σ_0 parameter is two times the standard deviation of measured conductivity at $V_G = 0$ V over 4 trials. For the p(g2T-TT)-based OECT, the reported uncertainty in the σ_0 parameter is two times the standard deviation of the measured conductivity at $V_G = -0.4$ V over 10 trials. Code for implementing the model and fitting to data are available from the author upon request.

APPENDIX III: SUPPORTING MATERIAL FOR CHAPTER IV

A. Discrete Model Derivations

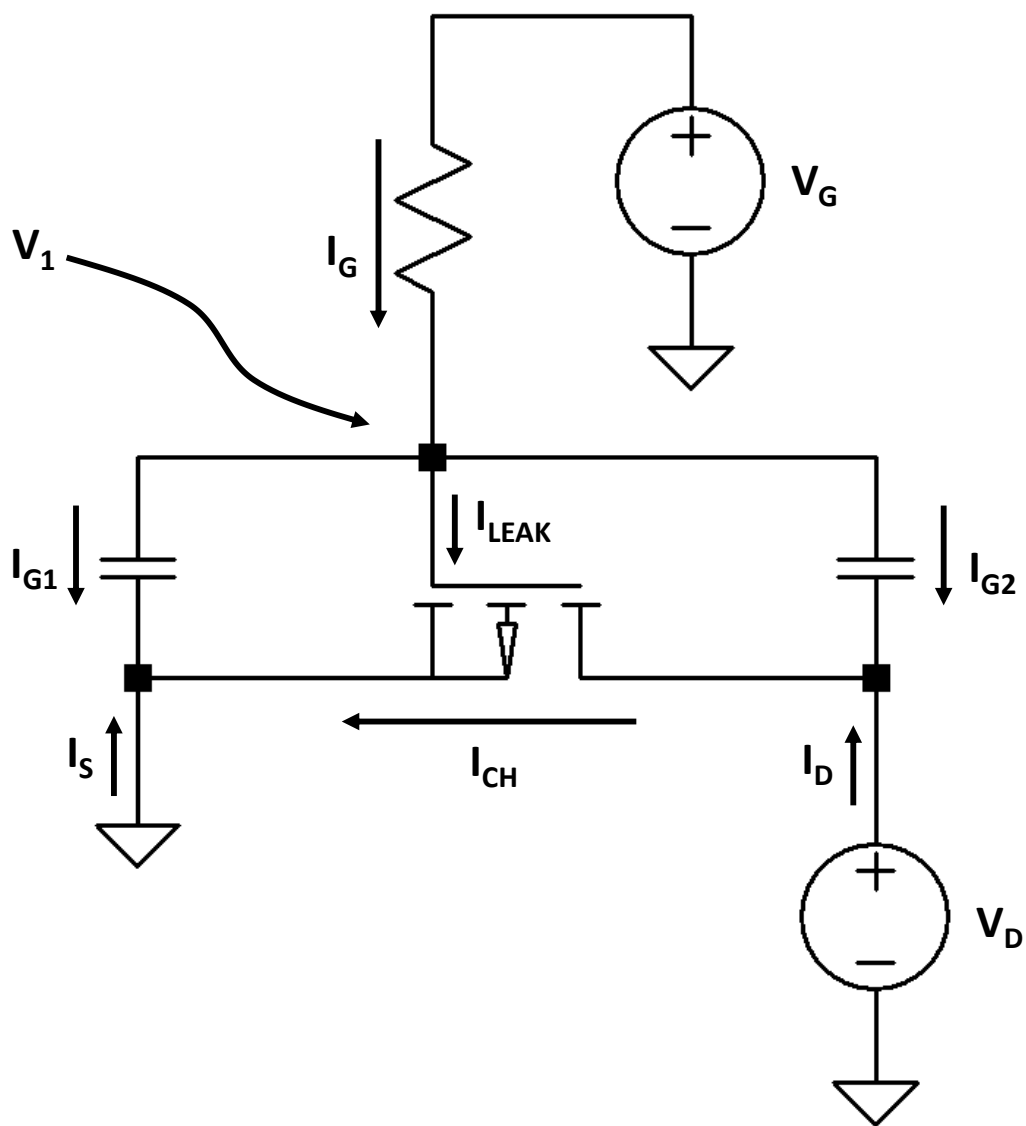


Figure IX-1. Circuit diagram for the Discrete Model description of an OECT (see chapter IV).

Figure IX-1 shows the circuit diagram that defines the simple model. In this section, we will derive the expressions for the source and drain currents resulting from an arbitrary gate input. First we consider the ionic current, which flows through the gate resistor and capacitors,

but not through the transistor.* In the following derivation, lower-case variables are used for time-domain terms and the corresponding upper-case variables refer to the Fourier transform of those terms. Assuming the leakage current, I_{Leak} , is negligible, and using the Meyer partition¹⁷² we have

$$i_{G1}(t) = \frac{1}{2} C_{CH} \frac{dv_1(t)}{dt}$$

$$i_{G2}(t) = \frac{1}{2} C_{CH} \frac{d}{dt} [v_1(t) - v_D(t)] \quad (\text{IX.1})$$

$$i_G(t) = \frac{v_G(t) - v_1(t)}{R_G} = i_{G1}(t) + i_{G2}(t)$$

Taking the Fourier transform of this system, we obtain

$$I_{G1}(\omega) = \frac{1}{2} j\omega C_{CH} V_1(\omega)$$

$$I_{G2}(\omega) = \frac{1}{2} j\omega C_{CH} [V_1(\omega) - V_D(\omega)] \quad (\text{IX.2})$$

$$I_G(\omega) = \frac{V_G(\omega) - V_1(\omega)}{R_G} = I_{G1}(\omega) + I_{G2}(\omega)$$

where ω is the angular frequency and $j \equiv \sqrt{-1}$. If the drain voltage is constant with respect to time, then $dv_D/dt = 0$, and we can write

$$I_{G2}(\omega) = \frac{1}{2} j\omega C_{CH} V_1(\omega) = I_{G1}(\omega)$$

$$I_G = j\omega C_{CH} V_1(\omega)$$

$$\frac{V_G(\omega) - V_1(\omega)}{R_G} = j\omega C_{CH} V_1(\omega) \quad , \quad (\text{IX.3})$$

$$V_1(\omega) = \frac{V_G(\omega)}{1 + j\omega\tau}$$

where $\tau = R_G \times C_{CH}$. Because $v_1(t)$ does not change too rapidly for typical values of τ , we can use the quasi-static approximation¹⁷¹ and transform V_1 , given by Equation (IX.3), back into the time domain and then insert the result into the steady-state equation for a long-channel PMOS transistor.²¹⁵

* Ionic current can flow laterally through the transistor channel, but the high channel length/thickness ratio ($\sim 10^3$) allows us to neglect this contribution.

$$i_{CH}(t) = \frac{\mu C_{CH}}{L^2} [V_P - v_1(t) + \frac{V_D}{2}] V_D, \quad (\text{IX.4})$$

where μ is the hole mobility, L is the channel length, and V_P is the pinch-off voltage. Both V_P and V_D are constants with respect to time. We can find the source and drain currents by adding the gate current to the channel current, as indicated in Figure IX-1.

$$\begin{aligned} i_S &= - \left[i_{CH} + \frac{1}{2} i_G \right] \\ i_D &= i_{CH} - \frac{1}{2} i_G \end{aligned} \quad (\text{IX.5})$$

1. Step response

The results of equations (IX.3), (IX.4), and (IX.5) describe how to find the source and drain currents for an arbitrary gate input. If, at time $t = 0$, the gate voltage is stepped from the constant value V_0 to the constant value $V_0 + \Delta V_G$, then

$$V_G(\omega) = \Delta V_G \sqrt{\frac{\pi}{2}} \left[-\frac{j}{\pi\omega} + \delta(\omega) \right] + V_0 \sqrt{2\pi} \delta(\omega). \quad (\text{IX.6})$$

Inserting this into Equation (IX.3) and taking the inverse Laplace transform, we obtain

$$v_1(t) = \Delta V_G [1 - \exp(-t/\tau)] + V_0, \quad (\text{IX.7})$$

for $t > 0$. Combining the results of (IX.1), (IX.4), (IX.5), and (IX.7) we obtain

$$i_G(t) = \frac{\Delta V_G}{R_G} \exp(-t/\tau), \quad (\text{IX.8})$$

And

$$i_{CH}(t) = \frac{\mu C_{CH}}{L^2} \left[V_P - V_0 + \frac{V_D}{2} \right] V_D - \frac{\mu C_{CH}}{L^2} V_D \Delta V_G \left[1 - \exp\left(\frac{-t}{\tau}\right) \right]$$

$$i_S(t) = - \left[\frac{\mu C_{CH}}{L^2} \left[V_P - V_0 + \frac{V_D}{2} \right] V_D - \frac{\mu C_{CH}}{L^2} V_D \Delta V_G \left[1 - \exp\left(\frac{-t}{\tau}\right) \right] + \frac{\Delta V_G}{2R_G} \exp\left(\frac{-t}{\tau}\right) \right] \quad (\text{IX.9})$$

$$i_S(t) = - \left[\frac{\mu C_{CH}}{L^2} \left[V_P - V_0 - \Delta V_G + \frac{V_D}{2} \right] V_D + \Delta V_G \exp\left(\frac{-t}{\tau}\right) \left[\frac{\mu C_{CH}}{L^2} V_D + \frac{1}{2R_G} \right] \right]$$

Notice that the source current will step instantaneously to the new steady-state value if

$-2\mu V_D/L^2 = 1/\tau$, in agreement with the Bernards model.²⁶

2. Frequency domain response

Having analyzed the response to a square gate voltage step, let us now derive the response to a sinusoidal input with frequency ω_0 . From Equations (IX.2)-(IX.5) we obtain

$$I_D(\omega) = \frac{\mu C_{CH}}{L^2} \left[\sqrt{2\pi} \delta(\omega) V_P - \frac{V_G(\omega)}{1+j\omega\tau} + \sqrt{2\pi} \delta(\omega) \frac{V_D}{2} \right] V_D - \frac{V_G(\omega)}{2R_G} \left[\frac{j\omega\tau}{1+j\omega\tau} \right] \quad (\text{IX.10})$$

$$I_D(\omega) = - \left[\frac{1}{1+j\omega\tau} \right] \left[\frac{\mu C_{CH} V_D}{L^2} + \frac{j\omega\tau}{2R_G} \right] V_G(\omega) + A_1 \delta(\omega)$$

where A_1 is a constant that describes the DC contribution to the drain current. We can separate the input signal into its component at frequency ω_0 and its DC offset. Then we can write $V_G(\omega) = V_G(\omega_0) + A_2 \times \delta(\omega)$, where A_2 is a constant describing the DC offset of the gate sinusoid. This yields

$$I_D(\omega) = - \left[\frac{1}{1+j\omega\tau} \right] \left[\frac{\mu C_{CH} V_D}{L^2} + \frac{j\omega\tau}{2R_G} \right] [V_G(\omega_0) + A_2 \delta(\omega)] + A_1 \delta(\omega) \quad (\text{IX.11})$$

and the component of the drain current at frequency ω_0 (for $\omega_0 \neq 0$) is

$$I_D(\omega_0) = - \left[\frac{1}{1+j\omega_0\tau} \right] \left[\frac{\mu C_{CH} V_D}{L^2} + \frac{j\omega_0\tau}{2R_G} \right] V_G(\omega_0) \quad (\text{IX.12})$$

We can divide this result by to obtain the transadmittance (that is the transfer function of the transistor) at the input frequency, ω_0 .

$$\frac{I_D(\omega_0)}{V_G(\omega_0)} = - \left[\frac{1}{1+j\omega_0\tau} \right] \left[\frac{\mu C_{CH} V_D}{L^2} + \frac{j\omega_0\tau}{2R_G} \right] \quad (\text{IX.13})$$

One can see from the above derivation that the transadmittance at the drain terminal (Equation (IX.13)) is composed of a channel admittance term (the leftmost term in the second set of brackets in (IX.13)) and a gate admittance term (the rightmost term in the second set of brackets in (IX.13)). This leads to the following expression for the full gate admittance (twice as large as the term in (IX.13) because only half of the gate current flows to the drain terminal):

$$\frac{I_G(\omega_0)}{V_G(\omega_0)} = \left[\frac{1}{1+j\omega_0\tau} \right] \left[\frac{j\omega_0\tau}{R_G} \right]. \quad (\text{IX.14})$$

Therefore, the ratio of drain current to gate current at frequency ω_0 is given by

$$\frac{I_D(\omega_0)}{I_G(\omega_0)} = - \left[\frac{\mu C_{GH} V_D}{L^2} + \frac{j\omega_0 \tau}{2R_G} \right] / \frac{j\omega_0 \tau}{R_G}$$

$$\frac{I_D(\omega_0)}{I_G(\omega_0)} = \frac{j\mu V_D}{\omega_0 L^2} - \frac{1}{2} \quad (IX.15)$$

$$\left| \frac{I_D(\omega_0)}{I_G(\omega_0)} \right|^2 = \left(\frac{\mu V_D}{\omega_0 L^2} \right)^2 + \frac{1}{4}$$

Therefore, $I_D(\omega_0) = I_G(\omega_0)$ when ω_0 is given by

$$\left(\frac{\mu V_D}{\omega_0 L^2} \right)^2 = \frac{3}{4}, \quad \text{for } I_D(\omega_0) = I_G(\omega_0)$$

(IX.16)

$$\Rightarrow \omega_0 = \frac{2\mu V_D}{\sqrt{3} L^2}, \quad \text{for } I_D(\omega_0) = I_G(\omega_0)$$

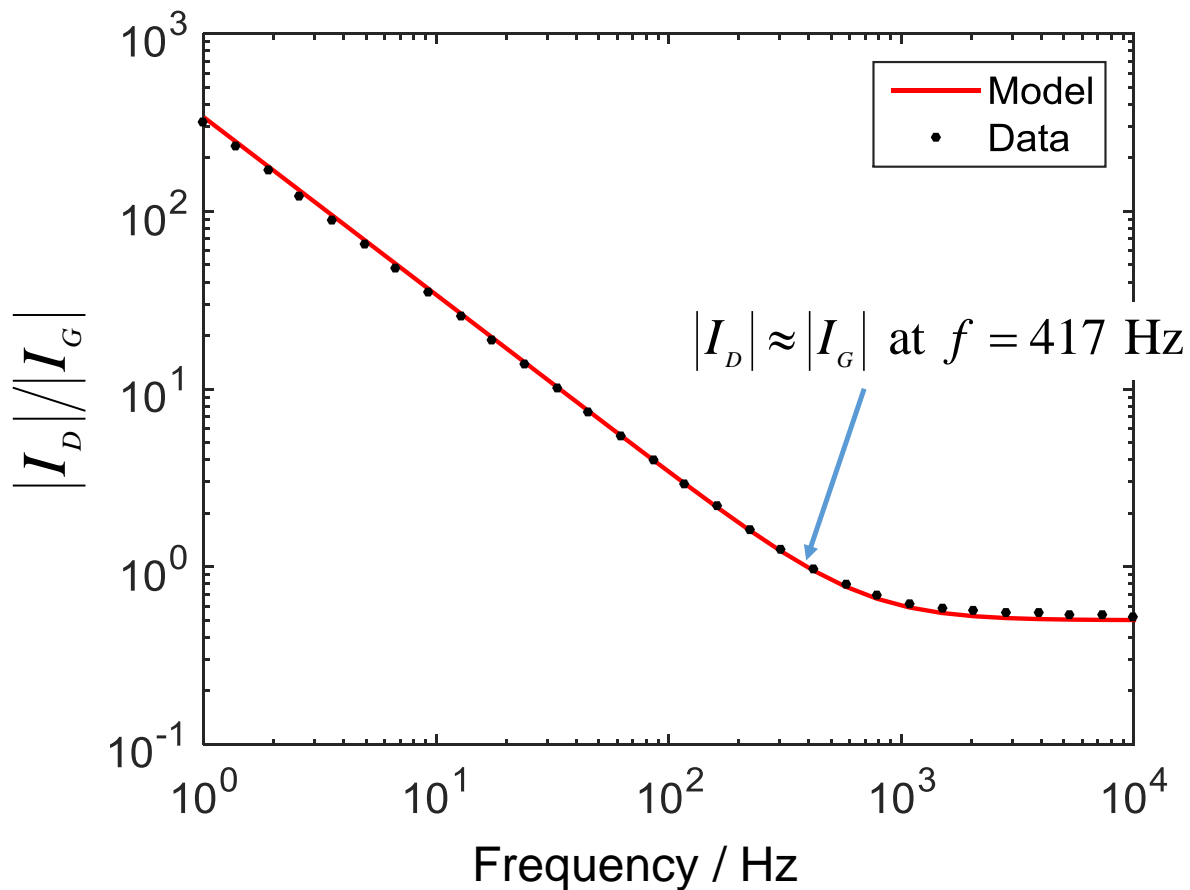


Figure IX-2. Ratio of gate to drain current as a function of the input frequency. Note that the values plotted here are the component of each current at the input frequency, not the DC values.

The data shown here were measured using the same device that was used for Figure IV-2 in chapter IV.

B. Experimental non-idealities:

1. Long-term current drift

Figure IX-3 shows the discrete model fit to the data shown in Figure IV-2c. In Figure IX-3, the data are plotted out to 20 ms, making it clear that the measured source current continues to drift long after the RC time constant of the ionic circuit.

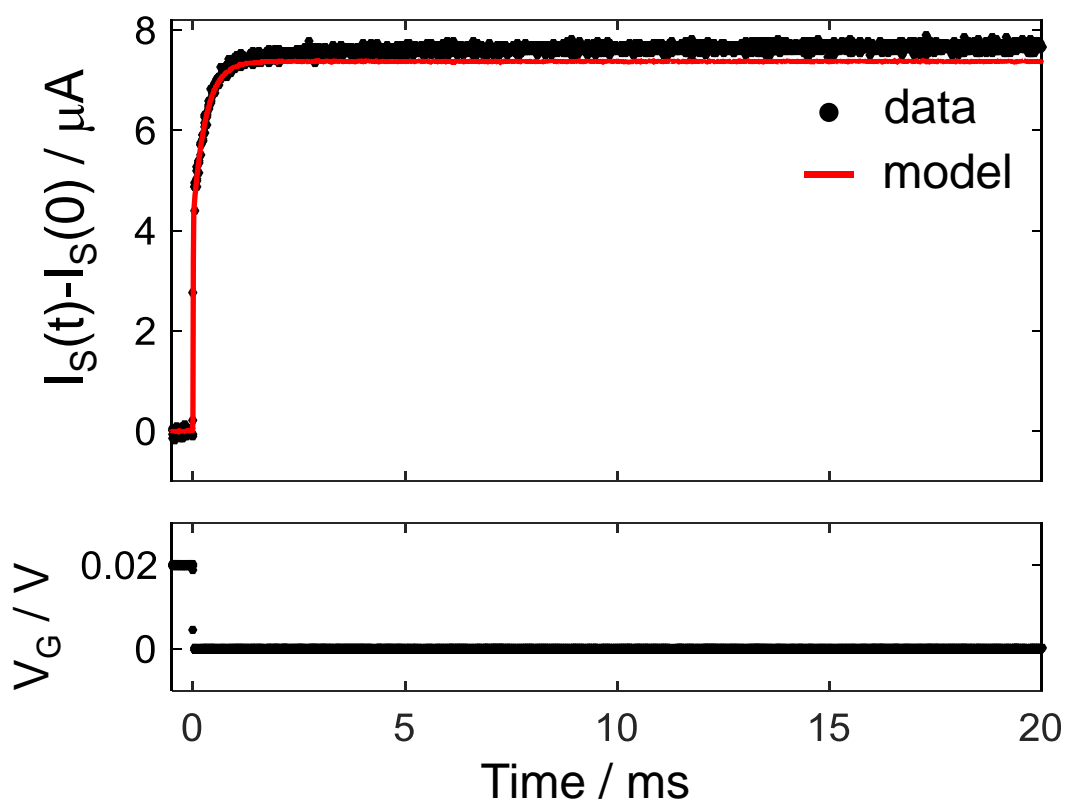


Figure IX-3. Long-term current drift is evident 20 ms after the gate voltage is stepped. The data shown here are the same as in Figure IV-2c.

2. Error between predicted and measured current at $t = 0$.

The error between the predicted and measured currents at $t = 0$ is due both to shortcomings in the discrete model and systematic measurement error. For instance, the model does not take into account the non-uniform hole mobility in PEDOT:PSS, so steady-state values

at different voltages may not simultaneously fit the model with the same mobility parameter. However, in some cases, there is a discrepancy between the source and drain currents measured at exactly the same gate and drain voltages, as shown in Figure IX-4. This discrepancy is particularly noticeable in Figure IX-4b, where the y-axis only spans 800 nA. The ~ 200 nA difference between the $t = 0$ values for the source and drain currents is in agreement with the performance specifications of the Agilent B2962a, which state that a fixed offset of 200 nA is possible in any measurement when using the 1 mA measurement range. In our experience, this offset is most noticeable when comparing measurements with voltages of opposite +/- sign. However, as shown in Figure IX-5, the error in measured current at $t = 0$ is negligible for small gate voltage steps and when not comparing source versus drain currents.

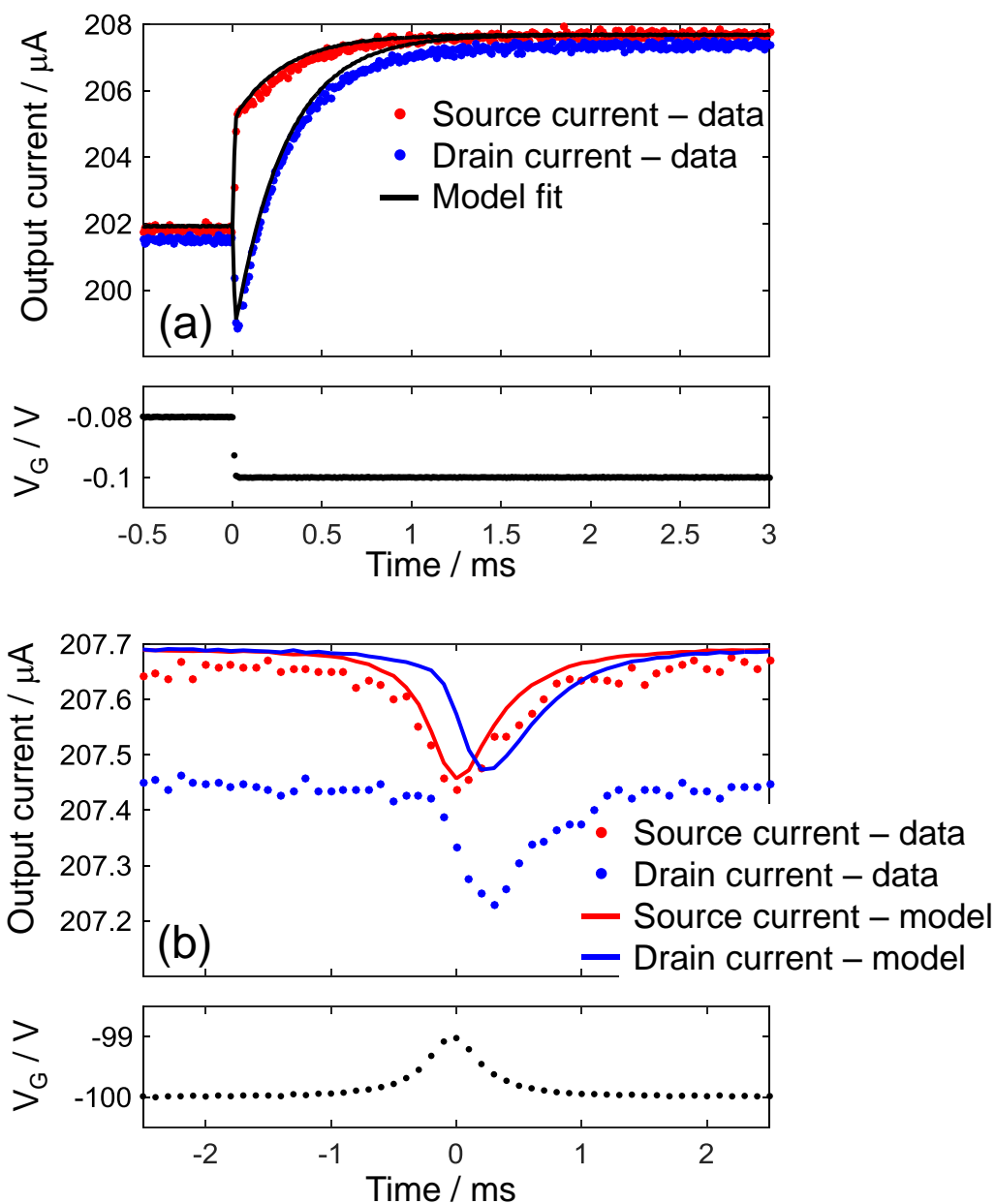


Figure IX-4. The raw data and model fits for the results shown in Figure IV-3a and Figure IV-3b. In (a), the discrepancy between the predicted and measured $t=0$ currents is 90 nA for the source current and 400 nA for the drain current (averaged over 101 data points). In (b), the discrepancy is 30 nA for the source current and 240 nA for the drain current (averaged over 200 data points). The fit parameters used here are the same as those used in Figure 3 of the main text; however, we included $V_p = 0.671$ V.

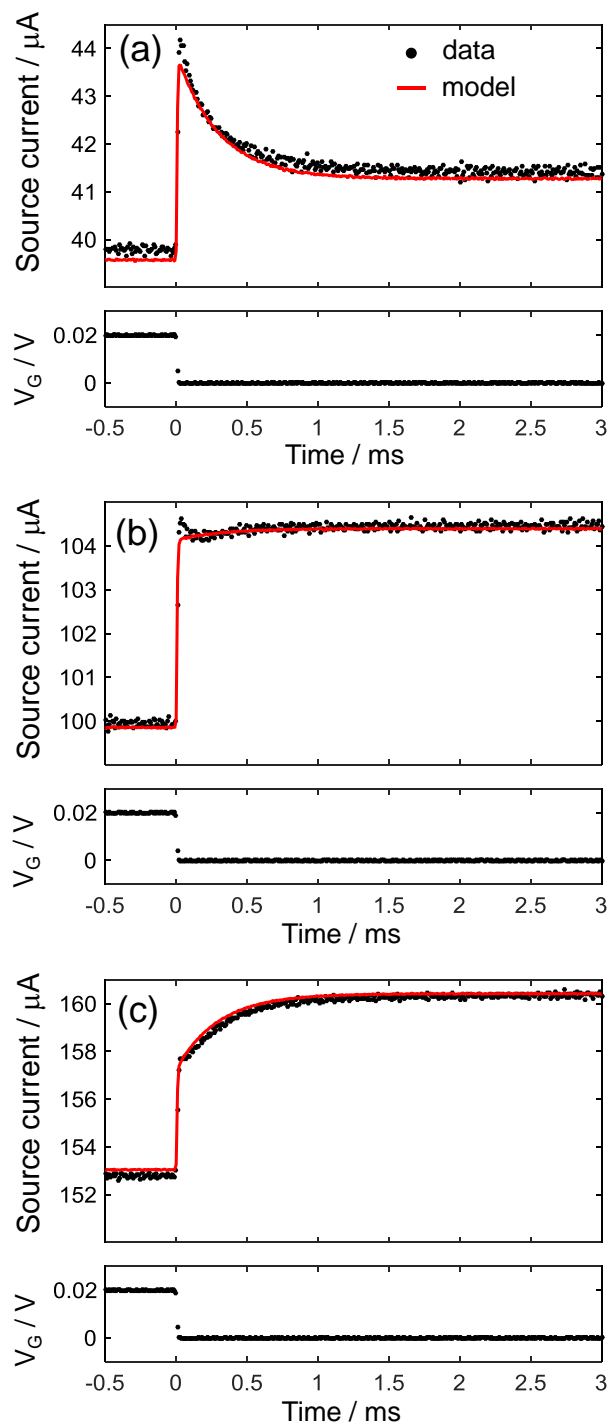


Figure IX-5. The raw data and model fits for the results shown in Figure IV-2a-c in chapter IV. In (a), the discrepancy between the predicted and measured $t = 0$ currents is 230 nA (averaged over 1001 data points). In (b), the discrepancy is 110 nA (averaged over 1001 data points). In (c), the discrepancy is 230 nA (averaged over 1001 data points). The fit parameters for this figure are the same as those used for Figure 2 in the main text; however, we've included $V_P = 0.5$ V.

3. Device stability

Figure IX-6 shows the device response to 2250 ON/OFF cycles and demonstrates the robustness of our devices to bias stress.

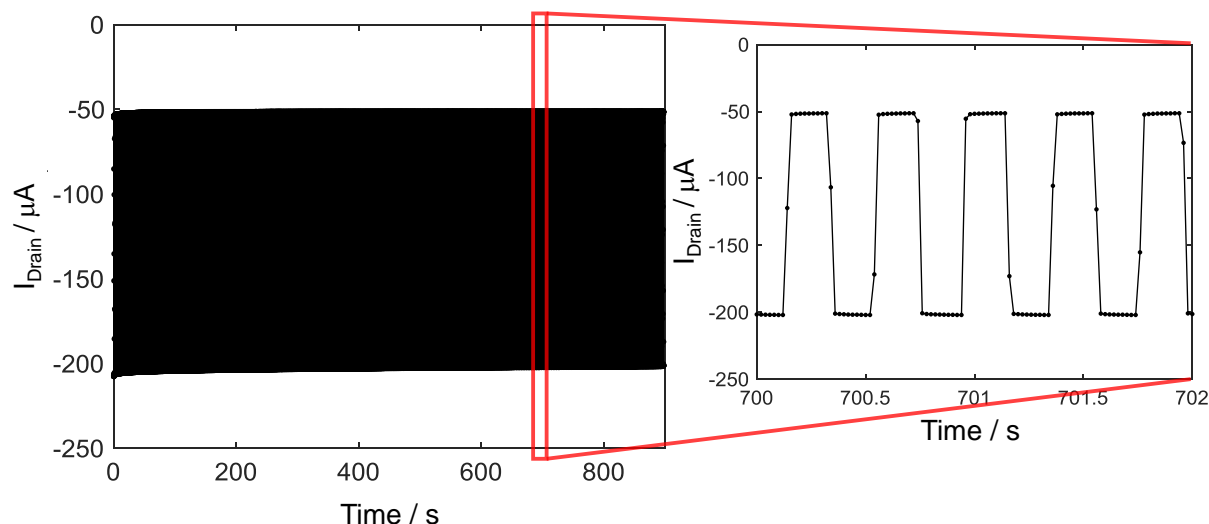


Figure IX-6. Response of a PEDOT:PSS-based OECT to a square pulse train at the gate electrode. The pulse train has a period of 0.4 s, a 50% duty cycle, a peak-to-peak amplitude of 0.4 V, and a DC-offset of 0.1 V. The drain voltage is fixed at a constant -0.1 V. In order to capture 15 minutes of continuous data, the sampling rate was set to 50 Hz. This figure shows that the device is stable for over 15 minutes of operation and 2250 cycles with minimum decrease in the on and off currents. The transistor used for this figure is the same device as the one used for Figure IV-3 in chapter IV.

C. Experimental details

1. OECT fabrication

OECTs were fabricated using a previously reported technique.²¹⁴ Gold electrodes were evaporated onto glass substrates and patterned via photolithographic liftoff. After this, an $\sim 2 \mu\text{m}$ layer of parylene-C was evaporated onto the substrate. Then an anti-adhesion layer (1% Micro-90 in water) was spun on before evaporating on a second layer of parylene-C. The parylene layers were patterned via reactive ion etching with a photolithographically patterned mask of AZ-9260. After etching, a PEDOT:PSS solution (95 wt% Clevios PH-1000, 4 wt% ethylene glycol, 0.9 wt% 3-glycidoxypropyltrimethoxysilane, 0.1 wt% dodecylbenzenesulfonic acid) was

spun onto the parylene layer at 3000 rpm for 30 s and baked at 95 °C for 75 s. Next, the sacrificial layer of parylene-C was peeled off of the substrate, leaving PEDOT:PSS films in the transistor channels and a barrier layer of parylene-C covering the gold electrodes. Finally, the sample was baked on a hotplate at 140 °C for 70 minutes and subsequently immersed in water for 4 hours.

2. Characterization

OECTs were characterized using a dual-channel source-meter unit (Agilent B2962a) with custom-written control code in Python. All measurements were made using a Ag/AgCl pellet (2 mm diameter \times 2 mm height) as the gate electrode. The electrolyte was a solution of 100 mM NaCl in water and was contained in a PDMS well on top of the OECTs. The time step between measurements was 10 μ s for Figure IV-2 and Figure IV-3a and 100 μ s for Figure IV-3b.

Because the source and drain currents could not be measured simultaneously, they were measured in consecutive experiments approximately 1 minute apart. The drain current was measured with a negative drain voltage applied to the drain terminal and the source terminal at 0 V. The source current was measured by floating the source-meter channels up to the drain voltage. For example, the source current shown in Figure IV-2c was measured with +130 mV applied at the source terminal and 0 V applied at the drain terminal. The gate voltage for this measurement was stepped from +130 mV to +150 mV at time $t = 0$.

Characterization of the accumulation-mode OECT was the same as that of the PEDOT:PSS devices except that we used 2 digital multimeters (NI-PXI-4071) to measure the gate and drain currents while biasing the gate and drain with a multi-channel data acquisition card (NI-PXI 6289). We used custom-written Labview control software for these measurements.

3. Estimation of parameter uncertainty

The fit parameters were estimated using custom code incorporating the nonlinear fit function `lsqcurvefit` from MATLAB R2015a. The fits were made between the discrete model and the frequency-domain data with upper and lower bounds on the mobility provided by the time-domain data. The measured gate voltage was used as the input for the discrete model calculations because the actual gate voltages are not perfect step functions or smooth Lorentzians. The +/- uncertainties for the fit parameters are 95% confidence intervals extracted using the `lsqcurvefit` Jacobian and MATLAB's `nlparci` function. The uncertainties for the mobility measurements using equation (IV.1) were calculated by propagating the uncertainty in frequency (+/- half the step size between frequency samples).